Université catholique de Louvain
Ecole Polytechnique de Louvain (EPL)
Département de science des matériaux et des procédés (MAPR)
Unité de chimie et de physique des hauts polymères (POLY)

Radioactive ion implantation of thermoplastic elastomers

Veronica I. Borcea

Thèse présentée en vue de l'obtention du grade de docteur en sciences appliquées

Composition du Jury:

Prof. Alain JONAS (UCL/POLY) – Promoteur
Prof. Christian BAILLY (UCL/POLY) – Président du Jury
Prof. Patrick BERTRAND (UCL/PCPM)
Prof. Roger LEGRAS (UCL/POLY)
Prof. Auguste LALOUX (UCL/TELE) – Président de la cérémonie
Dr. Marc LOISELET (UCL/CRC)
Prof. Stéphane LUCAS (LARN-NAMUR)
Dr. Said RACHIDI (CERTECH-SENEFFE)
Ing. Thierry DELVIGNE (DSI-TOURNAI) – Membre invité

Louvain-la-Neuve
Septembre 2008

Acknowledgements

First of all, I would like to thank Prof. Alain Jonas for having accepted to be the supervisor of the thesis. His suggestions, encouragements were always a precious support. In particular, I really appreciated the freedom of action he allowed me.

I also would like to thank Prof. Patrick Bertrand, Prof. Roger Legras, Dr. Marc Loiselet, Prof. Stephan Lucas, Dr. Said Rachidi and Mr. Thierry Delvigne for having accepted to be members of my jury: their remarks were an invaluable help. I am also grateful to Prof. Christian Bailly for presiding the jury and to Prof. Auguste Laloux for presiding the ceremony of the public defence.

This thesis was possible due to a small, but ambitious company, Delta Services Industriels (DSI) - Tournai, which has already grown much bigger than it was when we met for the first time. Their project, in collaboration with the Centre de Ressources Technologiques en Chimie de Seneffe (CERTECH) and the Université catholique de Louvain earned a Marie Curie fellowship offered by the European Commission, opening in this way the possibility of funding the first three years of my thesis. A special thanks goes to Thierry Delvigne, Benoît Deconninck and Olivier Courtois not only for the possibility offered, but also for the help during all the stages of the project.

With this occasion I would also like to express my gratitude to the European Commission, for the funding of the first three years of my thesis, and to the Université catholique de Louvain, for founding the fourth year.

Thanks are also due to the Centre de Recherche du Cyclotron of UCL, Marc Loiselet, Guy Ryckewaert and all the technical team, for the ^{7}Be implantation experiments of course, but not only. Thank you also for making me feeling welcome. In particular, I would like to express my gratitude to Mr. Loiselet for his special interest in the project, the encouragements, the support and the time dedicated to my thesis.

I really appreciated working within the Unité de Chimie et de Physique des Hauts Polymères (POLY) at UCL and I would like to express collectively my gratitude to all members of the laboratory. A special thanks to Aurore Becquevort, Sabine Bebelman, Colette Douchamps, Pascale Lipnik and Bernard Nysten for their availability and help. I would also like to say a special thanks to Gabriel Baralia and Jérôme Plain, for helping me in critical moments of the work.

The plasma etching experiments were performed in the Cleanroom facilities of Unité des Dispositifs Intégrés et Circuits Electroniques (DICE) at UCL with the help

of André Crahay, David Spôte, Christian Renaux and Nicolas Reckinger. Thank you for making it possible!

The Laboratoires d'Analyses par Reactions Nucléaires (LARN) of the Facultés Universitaires Notre Dame de la Paix - Namur offered the facilities and the possibility to carry out the Kr ion implantation experiments. I would like to express my gratitude for the opportunity offered.

I would also like to express my gratitude to Prof. Károly Bondor and Prof. Jean-Paul Issi, the thesis becoming possible also thanks to them.

A special thanks to Prof. Francis Labrique for his encouragements, for the great stories about Belgium, and not only.

My heart goes to my family, especially to Sorin, Mami, Tati, Gabi, Luli and Hadi, you were always there for me and I know that I will never be able to express all my gratitude for all that you have done for me. This thesis is OUR achievement. Thank you.

Abstract

The radioactive ion implantation wear measuring method (RII) has been used for many years as a tool to make highly sensitive real-time in-situ measurements of wear and corrosion in metallic or ceramic materials. The method consists of the controlled implantation of radioactive ions of limited decay time in a thin layer at the surface of the material. The progressive abrasion of the material results in a decline in radioactivity which is followed to monitor material losses.

The application of RII to control the wear of polymers is potentially of interest, but it has been lagging behind because of uncertainties related to possible changes in material properties during and after the implantation, and to the exact shape of implantation profiles. In this thesis, we investigate these issues on two thermoplastic elastomers typically used for making the soles of sport shoes, among which one contains radiation-sensitive unsaturated bonds, using as ions ^{7}Be, ^{7}Li and Kr. The results of the sample characterisation indicate that the ^{7}Be and ^{7}Li implantations, under properly-selected conditions, do not induce significant modifications in the materials. The implantation of a stack of polymer thin films and the activity measurements performed to determine the implantation profile are also presented. The experimental results on the ion implantation profiles and the determination of calibration curves are presented and discussed in comparison with simulated results. The results indicate that it is possible to predict the implantation profile by means of simulations. This bodes well for the application of the RII method to polymer materials.

In the last part, an experimental study is presented regarding the possible redistribution of the implanted ^{7}Be after implantation. Since very few existing experimental techniques are able to detect light elements implanted in polymer targets at fluences less or equal to 10^{12} cm^{-2}, with implantation depths of a few μm, a new method is presented, which implies the use of plasma etching techniques in order to remove layers of polymers and measuring the remaining activity after each step. Our results indicate that a redistribution of the implanted ions takes place during the implantation process, resulting in a scrambling of the initial implantation profile. Nevertheless, provided a suitable methodology be used, wear measurements in polymers by using the RII method are still possible, as we propose in the thesis.

Table of content

Chapter I
General Introduction

1. Context

In the modern world, polymer materials are present in almost all fields, even in the ones with high complexity and sensitivity, as for example, automotive industry, medical prosthesis, aerospace and so on. These materials are exposed, without exception, to different types of wear, which affect their functioning and their lifetime.

Therefore, one important field in material science is related to the study of the wear phenomena, in order to allow new materials, more resistant to the working condition, to be obtained. One of the most effective solutions is to determine an optimal material composition based on the results of investigation on the extent of wear for different material compositions and working parameters. Such investigation has a phenomenological nature and a final decision is made based on minimization of wear measured in experimental test systems.

When speaking about wear measurement, is necessary to study the problem from all aspects: the nature of the sample materials, experimental wear tests and wear measuring techniques. Therefore, we started by delimitating from the huge family of wear phenomena, two interesting cases of wear of polymer materials: weathering of organic coatings and the abrasive wear of polymers. A wear measuring method is without use without a good wear test, and therefore, our second step was to identify the possible experimental simulation methods suitable for the study of the two types of wear selected before. These two steps are presented interconnected in section 2 of this first chapter.

A new and promising wear measuring method was recently proposed, which is already proved to function well for metallic and ceramic parts. The question which was then posed is whether this method is suitable or not for wear measurements in polymer. It is well known that polymer materials are sensitive materials, therefore, the first issue was whether the method will affect or not the material to be tested. Therefore, we tried to apprehend the method and its alternatives, and a deep bibliographical study was performed on all the alternatives in order to establish which one could be used with polymeric materials. The results of this study are presented in section 3.

We had to select a material and to use it, if possible, during our entire project. The selection was not easy, and at the end, we decided for a thermoplastic elastomer, which has the advantage of a special morphology: a minority cylinder phase in a

majority matrix. This was important, because it would allow following the possible physico-chemical modifications by also surveying the modifications in the morphology of the material. Furthermore, we selected a copolymer with no oxygen present in the structure, which gives the opportunity to observe more easily the oxidation during different stages of the study: wear test, after implantation, etc. In addition, the thermoplastic character of this material ensures solubility, hence easy processing and characterization. The last step was to decide in a polymer with applications in fields were one of the wear types mentioned before is important. Therefore, we decided for a copolymer used as impact improver or for fabrication of shoe soles, Hybrar 7125. The material is presented in section 4.

This first chapter ends with an overview of the thesis and key aspects are underlined.

2. Wear of polymer materials

2.1. Classification

When we discuss about wear processes we have to consider the following phenomena: abrasion, corrosion, erosion, fatigue, cavitation, adhesion [1].

Abrasive wear occurs when hard asperities are ploughing into softer surfaces. We can distinguish three type of abrasion: two of them are taking place when two solids are in contact (two- and three body abrasion) and the other one (erosive abrasion) is occurring when abrasive particles are impacting a solid surface.

In the case of **corrosion**, we deal with chemical (or photochemical) degradation induced by light (especially ultra violet light), heat, atmospheric elements (oxygen, nitrogen, or atmospheric pollutants), humidity, and different liquids.

Erosion is a progressive loss of material due to a mechanical interaction with a fluid, a multi-component fluid or impinging particles (liquid or solid).

Fatigue is a wear of a solid surface caused by fracture arising from material fatigue, so it is a damage accumulation process. For example, when one surface slides over another there is a zone of compression in the material ahead of the motion. Plastic deformation of the material causes a zone of tension behind the motion. Cracks nucleate in the subsurface and propagate as a result of repeated cycles at a depth governed by the material properties. Eventually the cracks propagate to the surface and the material that was surrounded by the cracks is lost.

Cavitation damage is a progressive loss of material due to the continuous exposure to cavitation. Cavitation is defined as the repeated nucleation, growth and violent collapse of cavities, or bubbles in a liquid. Cavities in contact or close to a solid surface will collapse asymmetrically forming a micro-jet of liquid directed toward the solid. In addition, the cavities do not act independently, but collapse in concert. This effect leads to an enhanced effect such that the pressures produced by these

collapses may cause localised deformation and/or removal of material from a surface near the cavities.

Adhesion wear is due to localised bonding between contacting solid surfaces leading to material transfer between the two surfaces or loss from either surface.

When we discuss about different types of wear we have to consider the fact that in real situations it is impossible to affirm that we have only one type. Most of the time two or more of them occur simultaneously so the result is a synergistic process in which each of these is affected by the simultaneous action of the other, and in many cases is thereby accelerated.

In the following section, we present two cases where different types of wear are acting simultaneously: the weathering of polymer coatings devised for windmill blades and the contact motion of two solids.

2.2. Two case studies:

2.2.1. The weathering of polymer coatings

The first step made was a bibliographical research on the weathering of polymer coatings. A review of many scientific papers gave us the possibility to delimit the environmental factors that generate wear of polymer coatings. Very large collections of variables exist in the environment that can affect coatings durability. Light, temperature, moisture, pollution, abrasion, solvents, biological agents, etc., represent only a very small number of environmental variables affecting coating performance. There is an added complexity in that many of the environmental variables interact to cause coating degradation characteristics not observed with only a single variable. Often, because of this complexity, weathering technologists focus studies on what may be referred to as the big three environmental variables in weathering research: light, temperature and moisture. For the special case of windmill blades, we considered important to consider also the effects of atmospheric pollutants, rain and sand.

Factors affecting the wear resistance of the material

Sunlight in a materials exposure environment may play a key role in coatings durability and degradation. Solar radiation reaching the surface of Earth is characterised by wavelengths from approximately 295 up to about 2500 nm. The terrestrial radiation is classified as UV-B (295-315 nm), with energy of 426-380 kJ/mol, UV-A (315-400 nm), having energy between 380 and 300 kJ/mol and being less dangerous for organic materials than UV-B, visible (400-760 nm) and infrared (760-2500 nm).

The energetic UV radiation constitutes only about 1-5% of the total radiation. It represents, however, the most dangerous radiation component responsible for initiation of most outdoor effects in polymer materials by direct photolysis of covalent bonds. Visible light (39-53% of solar radiation) photosensitise chromophores and accelerates degradation in this way. Infrared light (42-60% of the total radiation) triggers thermodegradation of polymers. During photodegradation, generally chain scission, cross-linking and production of monomer or other small molecular-weight fractions, can occur.

Engineers consider several different **temperatures** important to weathering test methods: ambient or air temperatures, material surface temperature and bulk temperature. Materials surface characteristics: reflectance, transmittance, absorptance, (along with convection, conduction and emittance of the material) interact with ambient temperatures and solar irradiance to determine the temperature of a materials surface.

Environmental temperature changes affect coatings in two major ways: by inducing thermal stresses in the system and by changing the mechanical properties of the material. Thermal stresses result from difference of the coefficients of thermal expansion of the coating and substrate. In the initial period of exposure, due to its properties, the coating material has the ability to respond stress by molecular motions. However, physical ageing and chemical degradation result in a progressive decrease of the ability of the coating to relax stress. As a result, mechanical damage occurs to the coating (microcracks) as well as delamination from the substrate. Subsequently, during cyclic temperature changes, defects propagate [2].

Temperature differences can also drastically affect reaction rates, reaction mechanisms, pathways, and co-variables (such as moisture) in coatings degradation.

Pollutants play an increasing role in the environmental degradation of polymers. Oxidising and acid pollutants arising from both the human activities and natural sources such as carbon dioxide, sulphur and nitrogen oxides can be mentioned. Most of them, together with various volatile aliphatic organic compounds and their oxidation products are involved in reactions characteristic of chemical smog [3].

Important factors to be considered are the availability of the pollutant, his transportation to a surface, the interaction pollutant-surface, synergy with other environmental factors and the sensibility of the surface material to the pollutant. When gaseous and particulate species accumulate directly on a surface this is called dry deposition. Wet deposition occurs when the pollutants are incorporated into a fog droplet and then deposited as falling precipitation. At the pollutant-surface interface, the physico-chemical processes involve the diffusion of the pollutants through the material surface, the formation of products and additional diffusion through the products layer [4,5].

Just as light and temperature have multiple levels of influence on coatings degradation, **moisture** is also a multi-dimensional variable. Moisture in gas form, liquid form and solid form has different influences on materials degradation. This

manifestation of the temperature-moisture interaction effect causes different coating degradations. Similarly, frequency and duration dependencies also affect coatings durability. Exposure laboratories typically employ two main types of moisture measurement; relative humidity and wet time. Relative humidity indicates the mass of water vapour in the air relative to the air's maximum capacity given the air temperature. Wet time is the amount of time liquid water is present on a material's surface due to condensation and precipitation.

Water acts both as a chemical reagent in many hydrolytic weathering reactions and as a physical stressor in materials degradation. Moisture cycling by humidity or liquid water creates mechanical stress cyclic loading in many materials. Absorbed water induces compressive stresses on the outside and tensile stresses in the bulk. Drying creates bulk compressive and surface tensile stress gradients [6].

Whereas condensation often occurs at regular daily intervals, **rain** can play a more infrequent, seasonal role. The frequency and duration of rain is also closely linked with irradiance and temperature variations. The effects of rain may be similar to condensation, from the perspective of the water present on the coating's surface.

Moreover, when the effects of rain are considered, the impact of the water drops has to be considered. Rain is composed of a distribution of drop diameters that vary as a function of the rate at which the rain is falling [7]. Since the raindrops in a rain field undergo distortions as they pass through the disturbed airflow in the vicinity of a rotating windmill blade, the shapes of these drops at the time of impact can be quite different from what they are in the unperturbed atmosphere. Simulation programs and theoretical calculations were developed to evaluate the shapes of the raindrops at the time of impact as a function of the drop diameter [8,9].

When a liquid impacts a surface, the high-pressure zone produced in the earliest stage of impact can generate pressures of the order of gigapascals for a period of time depending on the impact velocity and geometry in the contact region. These high pressures are responsible for most of the damage resulting from liquid impact and are maintained while the edge of the contact area between the impacting liquid and solid moves supersonically with respect to the shock speed in the liquid [10]. Deformations of the surface such as plastic flow, buckling, and depressed annulus are only a few possible effects of liquid impact.

Sand particles entrained into airflow can impact on coated surfaces resulting in extensive erosion damage and degradation. The flow conditions along with the properties of the target material as well as the particle properties influence the impact dynamics and thus the erosion rate. Among the flow parameters, we can mention particle velocity, angle of incidence and flux (particle concentration) [11,12]. For example, if we consider the angle of incidence, we can distinguish two type of material behaviour: ductile (with maximum erosion rate at angles between 15° and 30°) and brittle (with maximum erosion rate at angles close to 90°) [13]. Note that when we consider the flux, we have to take into account the fact that

increasing the flux will not induce increase in the rate of erosion because the surface becomes shielded at higher fluxes by the rebounding particles.

Due to the heat generated by the impact, chemical degradation of the material can occur. Plastic deformation and material removal are also typical damages encountered on material surfaces caused by sand particle impact.

Testers and standard methods used to simulate the wear

The delimitation of the environmental factors affecting the durability of polymer coatings should be followed by an analysis of test methods used for artificial weathering of organic coatings. Table I-1 presents results of the analysis of test methods used for artificial weathering of organic coatings.

Different types of light sources were considered. Carbon arc, xenon arc and fluorescent tube lamps testers were evaluated from multiple points of view. Spectral output compared to the natural sunlight, the production of unwanted heating, automatic control of light intensity, temperature, light/dark periods and humidity were the factors taken into account. Different types of devices used for rain and sand erosion were also considered. In order to find out the requirements for the specific weathering tests, the corresponding standards were also considered [14-18].

This analysis allows formulating a conclusion concerning the environmental factors, which should be simulated to progress significantly into the understanding of the weathering of polymer coatings. Sand and rain impact in the presence of UV radiation are especially interesting as very little work has been carried out on the combined effects of sand and rain erosion [38], and the fact that polymer coatings used on windmill or helicopter blades are often exposed to both, sometimes simultaneously.

In order to predict the wear of materials subjected to impact by solid particles different setups can be used, such as: whirling arm (where the target is spun through a chamber of falling particles) [19], sand blast (where particles are carried in air flow and impacted onto a stationary target) [20-24], centrifugal acceleration erosion tester (where particles are fed into the central hole of a rotating disc, accelerated through several radial ceramic channels by the centrifugal force, ejected from the end of the acceleration tubes and impacted onto multiple targets) [25,26].

For the study of the erosion induced by rain, there are whirling arm type (where the target is spun through a rainfall) [27,28], single and multiple impact jet apparatus (where the target is fixed and impacted with a high velocity jet) or special test facilities [29].

The test should satisfy several conditions, so it has to simulate acceptably real conditions and be an accelerated test, which could determine polymer durability in significantly shorter times than natural weathering. In the same time, the test must have high accuracy.

Environmental factor	Simulation device	Damage type	Measuring methods
Light (UV radiation)	Carbon arc, Xenon arc, or Fluorescent tube sources QUV cabinets Prohesion chamber [4,30 ,31]	Gloss loss Chalking, Cracking Colour retention Increase of the surface tension [32,33]	SEM Optical microscopy FTIR Iodometric titration Contact angle XPS Weighing Oxygen absorption DMA Thickness measurements Specular reflectance intensity measurements DSC [30,34, 35,36]
Temperature		Mass loss Mechanical properties loss Cracks [2]	
Pollutants		Swelling Bubbling Blistering Micropeeling Cracking Material loss Transparency problems Thickness reduction [3]	
Moisture	Steam chamber Salt fog test chamber Salt spray test [6,32]	Mass modification Colour change Blistering, Chalking Dimensions increasing [32]	
Rain	Single and multiple impact jet apparatus Whirling arm rig [9, 37]	Circumferential cracking Depressed annulus Buckling Spall, Chipping [10]	Optical microscopy Weighing SEM [38]
Sand	Sand-blast method Whirling arm rig Centrifugal accelerator [9,39]	Mass loss Craters Cracking Roughening [11,12]	Weighing Optical microscopy FTIR Profilometry SEM [10,38]

Table I-1. Results of the bibliographical analysis of test methods used for artificial weathering of organic coatings.

The selection of a simulation method is a considerably complex issue. The bibliographic sources indicate that the whirling arm type device is a good method because it allows the simultaneous use of sand and water and satisfies the first two conditions mentioned before. However, it is not a perfect method for various reasons: a high centrifugal force is placed on the specimen and there is no provision for temperature or other control of the specimen, the rig consumes large amounts of power, the results are sensitive to specimen mounting, etc.

Similarly, the centrifugal acceleration erosion tester presents a series of problems such as: difficulty in assessing the mass of abrasive that strikes each target, divergence of the particle jet, impossibility to use it in combination with water, etc. [40,41].

As for the sand blast method and the impact jet apparatus, thus can be used only with sand or with water, respectively, therefore only for limited erosion tests.

2.2.2. The abrasive wear of polymers

Among many industrial applications, thermoplastic elastomers are dedicated to situations where the abrasion resistance is important. As a consequence, we decided to make a bibliographical research on the abrasive wear of polymers, including standard method and devices used to appreciate the abrasive wear resistance of polymeric materials. The results are presented in the following section.

Abrasive wear occurs when hard asperities are ploughing into softer surfaces. We can distinguish three types of abrasion: two of them are taking place when two solids are in contact (two- and three-body abrasion) and the other one (erosive abrasion) is occurring when abrasive particles are impacting a solid surface. For two-body abrasion, two surfaces are interacting: the first one, whose wear is of the most concern and a second one, a rough counterface, which is in motion relative to the first surface. In the three-body abrasion, abrasive material is present in the contact zone.

We already presented the principles of the erosive abrasion in the preceding section, when the effects of sand impact on the polymer coatings were discussed. In the following, we will try to focus on the abrasive wear occurring in the contact motion of two solids. We have to keep in mind that in many situations of a relative contact motion of two solids, the abrasive wear mechanism is accompanied by adhesion, corrosion (thermo-oxidative wear) and fatigue. In the case of soft materials, as polymers, the most encountered secondary phenomenon is adhesion.

A fundamental parameter of interest in all wear investigations is the **volumetric wear rate** (or specific wear rate, wear coefficient), expressed as:

$$W_v = \frac{V}{d \cdot L} \qquad \text{(I.1}$$

where V is the wear volume, d is the distance of sliding and L is the load applied [42]. The units of W_v are m^2/N, sometimes $mm^3/(N \cdot m)$. The terms 'wear resistance' and 'abrasion resistance' are also employed and correspond to the reciprocal of the wear rate, in whatever units are being used.

Factors affecting the wear resistance of the material

There are varieties of **material properties** that have been shown to have an effect on abrasive wear: hardness, elastic modulus, melting temperature, structure, fracture toughness, composition etc. [43]. A number of models that attempt to relate the abrasive wear resistance of polymers to the mechanical properties have been proposed [44]. One of these is known as the Ratner-Lancaster correlation. It predicts that the wear rate of a polymer, W is given by:

$$W = \frac{k\mu}{H\sigma_b\varepsilon_b} \qquad \text{(I.2}$$

where k is the proportionality constant, μ is the coefficient of friction, H the hardness and σ_b and ε_b are the tensile stress and strain at break.

A study that points to the effective number of physical crosslinks per macromolecular chain as the principal factor that dictates the intrinsic abrasive wear resistance for a commercially relevant polyethylene was also presented [45].

The properties of **abrasive material** that have an effect in the three-body wear are the shape of particles, hardness, toughness and size. For example, changing the shape of the particles (round abrasive) will induce less wear. Another example is that for a given volume of abrasive, a larger abrasive should impose less wear, since there are fewer points of contact and the contact stresses at these points are lower.

In two-body abrasion, the counter surface roughness, spacing and orientation strongly influence the wear processes, but the magnitude of the effect is different for various polymers [46].

The **type of motion** (sliding, rolling or fretting) influences strongly the basic mechanisms involved in wear processes. Sliding is the relative motion in the tangential plane of contact between two solid bodies. Rolling, the relative motion between two non-conforming solid bodies whose surface velocities in the nominal contact location are identical in magnitude, direction and sense, is generally less damaging compared to sliding. Fretting is a small amplitude oscillatory motion, usually tangential, between two solid surfaces in contact and is generally accompanied by fatigue wear [47].

Wear is proportional to **applied load**, as long as the load levels do not lead to fracture the abrasive. In this case, the wear rate will decrease if the abrasive is round or may increase if the fractured abrasive has sharp corners.

The wear rate will change with the **relative speed of motion**. This is connected to the heat generated in frictional process that accompanies the movement [48]. The effect of temperature on the abrasive wear behaviour depends on the material properties.

Due to the abrasion process, structural and topographical modification of the material can occur. For each of them, representative characterisation methods can be used.

Structural and topographical changes and characterisation methods

During the abrasion process, some of the molecular bonds may break so in this case the effects will be a reduction in the molar mass of polymer and oxidation. Dry sliding of rubbers on a hard abrasive leads to thermal decomposition of rubber by elevated frictional temperatures [49]. Another phenomenon observed in the case of sliding and rolling is the inducement of a preferred orientation of the molecular chains (generally parallel to the direction of motion) [50]. The incorporation of material transferred from the counter surface (wear debris) or of abrasive particles was also observed [51].

Therefore, the characterisation methods are solubility measurements and chromatography for the reduction in molar mass, spectrometry for bond breaking and oxidation products and AFM, optical microscopy and SEM for the changing in the orientation of molecular chains and foreign material incorporation [52].

Regarding the effects on the material topography, we can distinguish between grooving and rolling abrasive wear. In grooving abrasion wear, the same region of the abrasive particle or asperity is in contact with the wearing surface throughout the process. Therefore, wear surfaces are characterised by grooves parallel to the direction of sliding. In rolling abrasion wear, the region of the abrasive particles in contact with the wearing surface is continually changing, resulting in heavily deformed surfaces, with multiply indented appearance and little or no directionality [53].

Generally, in the case of abrasive wear it is impossible not to observe a roughness modification. Behind this, there are many plastic deformations: galling (macroscopic, usually localised, creation of protrusions above the original surface), ploughing (formation of groves by plastic deformation), and scratching (a mechanical removal or displacement, or both, of material from a surface). Surface cracks are less likely to be observed in systems with ductile materials. The techniques used to characterise this type of effects are profilometry, AFM, SEM and optical microscopy.

In the case of rubbery materials, a periodic surface pattern is formed. This abrasion pattern, a series of parallel ridges perpendicular to the sliding direction, is formed at the initial stage of abrasive wear and grows in ridge spacing and height. After a period, the abrasion pattern reaches a steady geometrical feature in spacing and high, which is almost held constant thereafter. The rate of abrasion loss increases with growing abrasion pattern and becomes constant after the pattern reaches the steady

state. Thus, the abrasion pattern can be recognised as an intrinsic and fundamental measure of rubber abrasion in rubber-like materials [54].

Testers and standard methods used to simulate the wear (3)

Name	Principle	Problems	ASTM Standard
Polishing or grinding test [58]	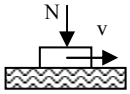 A plane specimen is loaded against the flat surface of a much larger counterface in the presence of abrasives.	Wear is generally not uniform over the specimen surface.	G174-04
Pin abrasion testing [49,51]	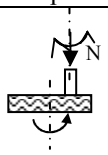 The upper pin specimen is perpendicular and sliding against the abrasive surface of a lower counterface that is mounted on either a flat circular disk, or a cylindrical drum, or a flat lateral positioning table.	Deformation of the pin and non-uniform wear over the pin transversal surface may appear.	G132-96 (2001)
Block on ring [55]	 A stationary block specimen is pressed with a constant force against a rotating ring counterface at 90° to the ring's axis of rotation.	Difficulties linked to the special geometry of the wear scar.	G176-03
Taber abrader [56]	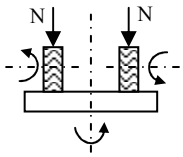 A plane specimen is rotated about a vertical axis under a pair of abrasive wheels that rotate independently and freely about a horizontal axis, which does not intersect the axis about which the specimen is driven.	Poor reproducibility, so restricted to testing in only one laboratory when numerical abrasion resistance values are to be used.	D4060-01 (2003)
Ball cratering (Ball on flat) [57]	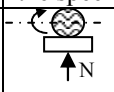 A hard sphere is pressed and rotated against the specimen surface in the presence of abrasive particles flow.	Difficulties linked to the special geometry of the wear scar.	

Table I-2. Standard methods for abrasion testing

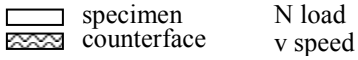

In general, the devices for assessing abrasive wear fall into three levels of complexity. At the lowest level are simple laboratory apparatus designed specifically to study the basic mechanisms by which surface damage is initiated and propagated; typical examples are rigid cones, spheres, needles or tips traversing polymer surfaces. At the other extreme are complex custom-built equipments, which are intended to simulate the conditions of operation existing in a particular application as closely as possible. Information obtained from such equipment, although of considerable value to the user, is rarely of more general relevance to other applications or problems. Between these two extremes are a range of laboratory apparatus designed to examine not only the relative ranking of materials in different regimes of wear, but also the ways in which wear varies with the sliding conditions (load, temperature, speed, environment, etc.) [42,58]. A selection of some more widely used standard methods of the latter type is shown in Table I-2.

2.3. Common wear measuring methods

The wear rate is expressed as a function of the volume loss during the wear test (equation I.1). Therefore, examination of the mass (volume) loss of materials is one of the most important indicators of wearing. A selection of common wear measuring methods is shown in Table I-3.

We can remark that in almost all cases, the test has to be stopped and the sample removed from the testing device. This will strongly influence the wear process and the results. The only two in situ methods, the radiographic and the displacement measurement, suffer from very low precision and reproducibility.

In some situations, the correct assessment of wear is vital. The total joint replacement prostheses usually consist of a metal or ceramic component against an ultra high molecular weight polyethylene (UHMWPE) part. One of the most important factors affecting performance and endurance of such implants is the wear rate of the UHMWPE component when metal or ceramic-polymer contacts take place. The generation of wear debris is detrimental to tissue and has been linked to complications including tissue inflammation, bone loss and implant loosening. There is a general interest, thus, in improving the wear performance of UHMWPE. The standard methods for wear assessment of prosthetic material generally indicate gravimetric techniques for the quantification of wear [59,60]. As exception, there is an ISO technical report, which indicates an alternative method, based on radionuclide techniques [61]. The principle of measurement and advantages of such a method will be presented in the coming section.

3. Wear measurement using Radionuclide Techniques

Wear measurement using Radionuclide Techniques (RNT) is a unique way to determine the tribological performance of a system continuously and in real time.

Method	Measuring technique	Advantages	Inconvenients
Gravimetric (mass loss)	Specimen is removed, cleaned, weighed, and remounted in the test apparatus.	Simplicity, direct measurement of the mass loss	Difficult to measure very small mass loss; Possible errors due to moisture or lubricant absorption
Profilometry	The worn surface is compared with a region not exposed to wear.	Indication about local wear	Disturbing effects due to creep and temperature variation
Optical measuring	In test methods with imposed wear scar, the wear scar volume is calculated using optically measured dimensions	Very small amount of wear can be quantified	It is very difficult to establish the exact shape of the wear scar and the mathematical relation for the volume calculation.
Duplication	Replica of the surface is made and studied with profilometry, optical methods	Can be combined with other methods	Replica material leftovers may influence the test afterwards; Temperature sensitive
Radiographic	X-ray images are taken during the test and processed by means of special software.	In situ method	Poor precision and reproducibility
Displacement measurement	Displacement transducers measure the movements of the sample during the test	In situ method	Disturbing effects due to creep, wear debris generation and the linear expansion of the specimen with generated heat

Table I-3. Common wear measuring methods

Due to its extremely high resolution and accuracy, this method is especially suited to mechanical systems showing low ware rates. If friction is also measured, dynamic processes like running-in can be assessed precisely, leading to a deeper understanding of the fundamental mechanisms of the wear process. The method, therefore, can be used for applied as well as for detailed basic research.

The principle of wear determination by nuclear methods consists of a radioisotope introduction upon the component to be studied, namely the activation of the material. Wear processes are characterised by a loss of material assessed by radioactivity measurements.

3.1. Activation of materials

The most used radioisotope methods may be classified depending on the activation method.

A. Activation based on nuclear reactions induced in the wear parts
    1. Activation by neutrons (bulk activation)
    2. Activation by charged particles (Thin Layer Activation – TLA)
B. Radioactive Ion Implantation (RII)
    1. Recoil implantation (Ultra Thin Layer Activation – UTLA)
    2. Direct implantation
C. Radioactive marker melting method [62]
D. Chemical substitution of a radioactive isotope for a normal constituent of a molecule of interest [63]

In this section, we will describe the activation techniques based on nuclear reactions induced in the wear parts and the radioactive ion implantation methods. The last two methods have not been generally used so far and therefore will not be detailed in this work.

Not all the radioactive isotopes than can be produced are useful, because some are produced with low efficiency or have half-lifes too long or too short. Since a radioisotope is essentially unusable after 5-6 half-lifes, isotopes with at least 1 or 2 months half-lifes are typically chosen for wear tests. Corrosion tests (if not accelerated) may require a long period in which to perform the measurement, and thus utilise longer-lived isotopes.

3.1.1. Activation based on nuclear reactions induced in the wear parts

Atomic nuclei of wear parts may be marked radioactively by employing nuclear reactions:

$$A(a,b)B \qquad \text{(I.3}$$

In such a nuclear reaction the atomic nuclei *A* of the target material are bombarded by various particles *a* such as neutron, protons, α-particles or deuterons with high kinetic energy (in the range of 5 to 100 MeV). Upon impact, the target nuclei are transformed into the intermediate state of highly activated compound cores. As consequence of this high excitation, an immediate emission of various other particles *b* (e.g. neutrons, protons, deuterons, α-particles or γ radiation) from the compound core takes place. As a result of the nuclear reaction the nuclei *B* can remain in unstable, radioactive states. Consequently, their excitation decays by the emission of α, β, γ or X radiation. The emitted radiation then is detected and evaluated by the RNT measuring system.

Activation by neutrons

The first type of activation based on nuclear reaction, the activation by thermal neutrons**,** is carried out in a nuclear reactor. Neutrons are uncharged particles and can penetrate large distances before being captured. Since the resulting activity is present throughout the entire volume, this technique is also named "bulk activation". The isotopes can be predicted beforehand to satisfy a particular experimental requirement by selecting the suitable reaction [62,63].

The activation by neutrons is a comparatively inexpensive method but it presents also problems [64]. In nearly all cases, the targets become radioactive throughout the entire sample and not only in the wear zone close to the surface. This means that the activity is higher than needed. Therefore, protective measures and special safety facilities are needed during the wear measurements and these reduce considerably the applicability in the industry. Moreover, in some cases it is not possible to get suitable radioisotopes by bombarding a material with neutrons.

Activation by heavy charged particles

In addition to activation by thermal neutrons, the target may be activated by the bombardment with heavy charged particles. The particles may be protons, deuterons or α-particles originating from an accelerator, such as a cyclotron. This increases the number of possible nuclear reactions, increasing also the number of materials that can be tested [62,65,66]. When using this technique the target becomes radioactive only in a thin zone near its surface since the charged particles quickly lose their kinetic energy as a consequence of intense interactions with the target atoms. Therefore, this activation method is called Thin Layer Activation (TLA). The maximum penetration depth of charged particles depends on the energy of the particle, the angle of incidence and various properties of the material.

Compared to the activation by neutrons, another advantage of TLA is the small total activity of the tested component. Thus, wear measurement using this technique can be carried out even in industry without special protective measures, therefore eliminating handling problems. TLA offers the possibility of activation of small, well-defined regions on a component. By choosing bombarding particles of different

types and energy levels, different patterns of radioisotopes may be obtained in targets of identical material [67].

3.1.2. Radioactive Ion Implantation

When the sample does not contain any element that can be activated, the necessary radioactive nuclides can be implanted. In order to reduce the risks of material modification, light radioactive species are selected for implantation. One way of introducing radioactive tracers in the part to be studied is to implant recoiled radioactive products from nuclear reactions. Another way is the direct implantation using radioactive ion beams.

Recoil implantation (Ultra Thin Layer Activation – UTLA)

This method relies on a light ion beam *a*, which bombards a sacrificial target *A* and produces radioactive recoils *b* by the nuclear reaction [68]:

$$A(a,b)B \qquad \text{(I.4}$$

Some radioactive isotopes acquire sufficient kinetic energy to recoil out of the target and stop in the material. The incident beam is stopped upstream the material by a beam stop. In this way, a range of radioisotopes (^{7}Be, ^{56}Co, ^{57}Co, ^{58}Co) can be implanted into all kind of materials [69,70].

The energy spectrum of radioactive nuclei transmitted from the target is continuous, with a maximum energy ranging from a few hundred keV to a few MeV. Using the recoil technique the activated depth is much smaller than using TLA technique, where the energy of the incident particle has to be sufficiently large to enable nuclear reactions. Therefore, this method is also called Ultra Thin Layer Activation (UTLA). The implantation depth depends principally on the radioactive ion mass, the incident particle mass and energy.

Compared to the activation with neutrons or charged particles, where the heat generated during the exothermal nuclear reactions can modify or even destroy the activated material, the recoil implantation can be used for the radioactive labelling of sensitive materials. However, the presence in the implanted area of particles from the primary beam, indicates that the damages are greatly but not completely decreased [71].

Direct implantation of radioactive ions

Various radioactive beams of light species from ^{6}He to ^{35}Ar are accelerated and used for experiments in nuclear astrophysics and nuclear physics [72,73]. The production of an intense and stable ^{7}Be radioactive ion beam has generated considerable efforts in several laboratories [74-76]. One application is in the field of nuclear astrophysics for the understanding the high-energy flux of solar neutrinos. Being the lightest gamma-emitter with suitable half-life (53.3 days), ^{7}Be is also the favourite tracer nuclide for high sensitive wear analysis. Its gamma energy is high enough (477.56

keV) to penetrate even a couple of mm of thick iron, allowing gamma measurement without disassembling the investigated system. Another element also used was ^{22}Na [77], but his long half-life (2.6 years) increases the problems linked to the radioprotection.

The direct implantation permits the implantation of ion beams with a wide range of energies, enabling the possibility to obtain various activated profiles. Another advantage over UTLA is the absence of the high-energy primary beam; the risks of target material modification are therefore diminished.

3.1.3. Calibration curves

In order to make a wear measurement using RNT, theoretical calibration is very important, first to select the right activation conditions (particles, energy, geometry, duration, etc.) and second to estimate the activity needed and the depth of sample to be considered for the study [78]. The distribution of the activity in the depth of the material, or so-called calibration curve, can be obtained by using Monte Carlo simulation programs such as IRIS (Implantation of Recoil Ions Simulation) for recoil implantations or SRIM (Stopping and Range of Ions in Matter) for direct ion implantations [79,80]. There are also mathematical methods and simulation programs for the activation methods based on nuclear reactions [78].

The calibration curve for wear determination is given by the following formula [66]:

$$R = \frac{N \cdot \exp(-\lambda t)}{N_0} = f(x) \qquad \text{(I.5}$$

with R the relative remaining activity, N_0 the counting rate of the total thickness of the irradiated area (counts/s), N the counting rate of the same area after the removal of the upper elementary layers (counts/s), λ the decay constant (s^{-1}), t the time after measurement of N_0 (s), and x the thickness of removed layers.

During the activation of the material, by neutron or heavy charged particles bombardment or by ion implantation, the experimental calibration is also performed. In the case of bulk implantation, the experimental calibration is very simple, since the total radioactivity can be assumed to be evenly distributed throughout the mass and volume of the activated part. Therefore, a reference coupon can be included in the activation step for the components of interest with good assurance of simultaneously achieving identical mass-specific activity [81].

When TLA or nuclear implantation is used, generally three methods may be used in order to obtain the experimental calibration curve. The selection of the method depends on the thickness of the activated layer and on the nature of the sample material.

One possibility is the polishing of the activated sample, where the residual activity is measured after removing thin layers of material by mechanical or chemical polishing. At each step, the sample is washed and then activity and thickness of the sample are measured.

Another method used is the stacked foils method. The method consists in implanting a stack of foils made of the same material as the studied one. The thickness of the whole stack is equal or greater than the implanted depth in the given implantation conditions. After implantation, high-resolution γ ray spectrometry measurements are performed to determine the activities of the stacked foils step by step when foils are removed one after the other from the stack [78].

When very low activated depths are planned, thin films of same composition as the investigated sample with various thicknesses are deposited on a substrate. After irradiation, radioactivity A_0 in the pair film-substrate is measured. The thin film is removed from the substrate by dissolution and the activity A of the substrate is measured. The ratio A/A_0 expresses the relative remaining radioactivity after a material loss equal to the film thickness.

Finally, another important aspect that has to be considered when TLA or RII are performed is the precision in the position of the activated zone. Autoradiography is a simple and fast control method that can be used for all energy emissions and a wide range of surface geometries [82]. The good selection of the parameters (film type, deconvolution filters, exposure time) may improve considerably the precision of this method [83].

3.2. Wear measurement methods

Using the RNT techniques, two different continuous wear measurement methods are applied: the concentration method and the difference method. Both techniques offer the advantage of continuous observation and measurement of the progress of wear on parts in service without having to stop or even disassemble the system. The time dependence of wear is determined from the radiation emitted by the activated material.

3.2.1. Concentration method

The concentration method involves measuring wear by detecting the radiation emitted by wear particles carried away from an activated surface area by a transporting medium (lubricant, fuel, etc.). The medium and the wear particles are carried to a highly sensitive detector, which measures the radiation emitted by the wear particles. There are two possible configurations: the concentration flow method and the filter concentration method [64].

In the **concentration flow method**, the transporting medium is pumped through the flow-through measuring head, consisting mainly of the measuring vessel and a

detector, placed in a near 4π detection geometry. The measuring vessel is shielded by lead to reduce background signals originating from natural radioactivity as well as from the activated parts of the system tested.

If filters are located in the flow circuit of the transport medium, the concentration-flow method must be supplemented by a **filter probe**. The radiation emitted by the wear particles retained in the filter is measured by a detector within the filter measuring head.

In order to obtain the correlation between counting rate of signals during operation of the system and the absolute amount of linear or volumetric wear a calibration procedure is performed. In the case of concentration methods, the calibration of the mechanical-spectrometric arrangement is made using different sets of standardised single radioisotope samples, dissolved in the flow chamber, or in the filter head volume, respectively [66]. The proportionality between the radioactivity level and the concentration of activated material particles removed by wear processes and suspended in the fluid is given by:

$$M = K \cdot V \cdot C \cdot N \qquad \text{(I.6}$$

with M the total mass of wear, K the specific calibration factor (constant of each mechanical-spectrometric arrangement), V the total volume of fluid, C the ratio between the mass of standard and his counting rate and N the counting rate of wear particles in the transporting medium.

In the case of concentration methods the background or starting reference is initially a non-radioactive environment (if the source object is isolated from the location of wear debris), in which accumulates the radioactive wear. Therefore, the relative change in activity is very large and this gives the high sensitivity of the technique.

Using filters and RNT an analysis of the size distribution of wear particles can be performed [65]. A sample of the transport medium is taken together with wear particles, diluted and passed through a series of filters. A set of track etched membrane filters can be chosen, as it offers the smallest scatter of pore diameters and finest gradation of pore sizes. The diluted sample is filtered using the filter with the largest nominal pore size. The filter retain the residue, which is separated, whilst the drop-out is collected in a test tube and is filtered again using a pore filter with the next smaller pore size, and so on. In between two filter stages, the test tube is placed into a measuring head, containing mainly the detector, to determine the mass of the wear particles. This mass can then be standardised against the total mass of the activated wear particles and plotted as a function of the filter pore size [84].

3.2.2. Difference method

In the second continuous wear measurement method using RNT, the difference method, wear is studied by measuring the decrease in the residual activity of the

irradiated system part versus the thickness of removed material. The activity is measured by a γ-detector with a lead shielding to reduce signals originating from normal radioactivity. Special attention must be paid to the detector position near the labelled piece.

Although the principle of the difference method is quite simple, many influencing factors such as geometric limitations, optimisation of the distance between detector and moving machine part and absorption of the emitted radiation before it reaches the detector, complicate the measuring situation. For resolution purposes, it is essential for this technique to activate only a very thin surface zone or surface layer. If the activated surface is too thick, then wear may only result in an irresolvable small change in total surface activity [64]. As consequence, this measuring method can not be used with neutron activation techniques, where the entire part is activated.

Figure I-1 present a schematic view for the application of RNT measuring methods: the difference and the two concentration configurations.

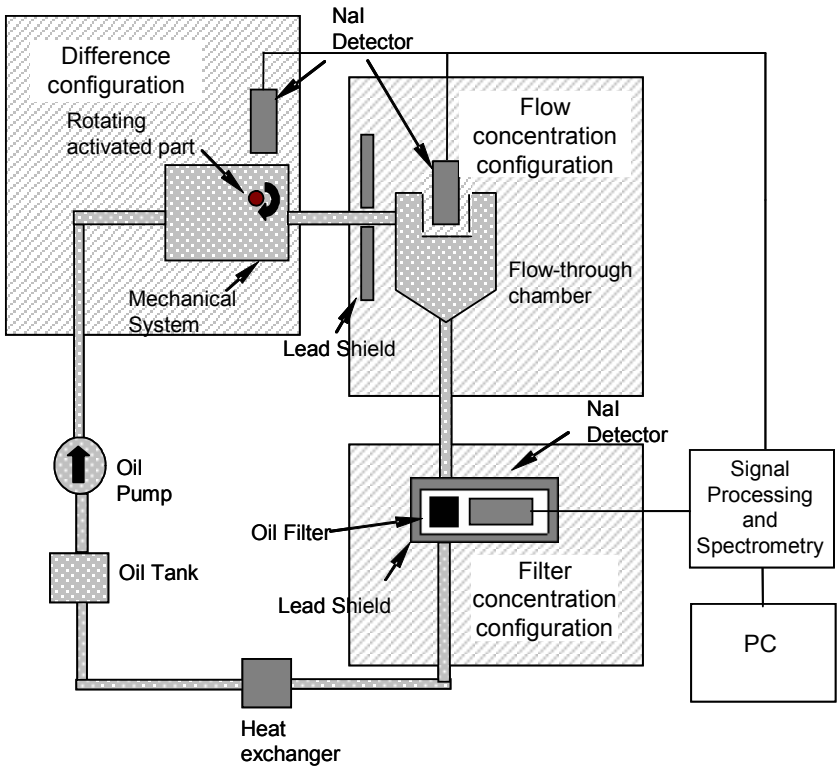

Figure I-1. Schematic view for the application of RNT measurement methods

3.3. Advantages over other wear measuring methods and applications

Unlike other methods (weighing for example), where the test is stopped time by time to make the measurement, RNT allows continuous measurement of wear as a function of time. They are high-speed techniques, enabling their use as online measurement methods. The material loss can be monitored and quantified in real time.

The material penetrating properties of γ-radiation allows measurement without disassembling the investigated system, offering the possibility of in-situ applications.

Selected areas for wear measurements may even be narrowly demarcated. Only the material loss from this particular region is monitored. Using appropriate activation procedures, different radionuclides can be introduced into different areas of a component, or in different components of a system, and the wear from these areas can be followed simultaneously and independently.

Various radionuclides emit radiations of specific energies; therefore, the activation by nuclear reactions opens the possibility of monitoring individual elements and this may be very useful in selective corrosion studies.

The sensitivity of the material loss measurement is high. With activated layers of a few micrometers in depth, precision in the nanometer range is possible with a minimal amount of radiation.

For a good detection, a small amount of radiation is enough (~10 kBq). This corresponds to a dose equivalent of approximately 0,35 mSv (Sievert) which is almost 10 time smaller than the natural dose (2,4 mSv/year).

Being on-line, continuous measuring methods, the influence of operating conditions and parameters (speed, temperature, pressure) on the wear behaviour of the system can be determined. Knowing them, the wear behaviour can be correlated to different operating conditions and parameters. For example, in the analysis of running-in performance it is possible to evaluate the period until a constant value of wear rate is reached, the wear rate upon reaching stationary wear behaviour and the wear rate immediately after variation of the operating conditions.

The major field of application is the study of wear behaviour of different engine components. Real-time experiments were performed on piston rings and cylinder bores wear in spark-ignition engines [81] and camshafts [85]. Analysis of the influence of surface texture of the shaft and bearing on the minimum admissible lubricant film thickness at the transition from fully hydrodynamic lubrication (almost no wear) to boundary lubrication in sliding bearing/shaft systems was carried out [64]. A study of wear characteristics of various oils using TLA

techniques was made in order to obtain solutions for oil consumption reduction [62, 65].

Erosion of generator components of a hydroelectric power station was studied using TLA. The results were used to select materials that are more resistant and TLA was also used as the basis of an automated, on-line alarm system to warn station operators on further damages [86].

High temperature cyclic oxidation (at 900 and 1000 °C, with cooling to ambient temperature) of pure and yttrium implanted chromium was studied using TLA [87]. Recoil implantation of ^{56}Co radioactive nuclei was used to measure the nanometric corrosion rate of stem generator tubes of nuclear power plants [79]. Activation of a Ni-Cu alloy and a Cu-Sn alloy (artistic bronzes) for corrosion monitoring and metal release monitoring was also reported [78].

Finally, we have to mention that RNT wear measurements are limited to cases where wear products are totally removed. Another sensible aspect is that the radioactive material must behave like the non-radioactive version with respect to mechanical properties.

3.4. Radionuclide techniques and polymers

When RNT are to be used for wear measurement of polymers, the problem of possible physico-chemical modifications of the material during the activation process has to be considered. During the presentation of the different activation techniques, we highlighted the fact that the direct implantation of ^{7}Be is the less damaging method. Due to difficulties in the preparation of a stable ^{7}Be ion beam, there are no wear experiments based on direct implantation reported in the literature. The only report about direct implantation of ^{7}Be in polymer (polyethylene) presents the calibration curve obtained using an energy wobbling technique [77].

The few investigations performed up to now are based on the recoil implantation technique. Calibration curves have been measured by using the stacked foils method, with a continuous energy spectrum of recoils, ranging from 0 to 10 MeV with a mean energy of 3 MeV [68]. By comparison with ^{12}C and ^{4}He implantation in polymers at similar dose, the authors concluded that no modifications of mechanical and chemical properties are produced in polypropylene and polyethylene foils.

The effect of the ^{7}Be recoil implantation on wear of a medical grade UHMWPE was studied using a block-on-cylinder screening wear tester [71]. The implantation of 300 Bq of ^{7}Be (energies spectrum between 0 and 10 MeV) to a depth of 20 μm (with a homogeneous implantation to 5 μm) did not alter the wear behaviour of medical grade UHMWPE when compared to non-implanted samples measured by 3D laser profilometry.

Wear evaluation of a cross-linked medical grade polyethylene by UTLA compared to gravimetry demonstrated a good correlation between the two methods [88].

Furthermore, in comparison with gravimetric results, the UTLA data shows a significant lower uncertainty about the mean values.

We can thus conclude that, no thoroughgoing study on possible physical or chemical modifications resulting from recoil implantation has been reported so far.

4. Thermoplastic elastomers

As mentioned previously (end of section 2.2.1), our work will focus on the implantation of thermoplastic elastomers for wear monitoring. Therefore, in the coming section, we briefly present the main characteristics of these materials.

4.1. General considerations

Thermoplastic elastomers (TPEs) are a class of polymer or polymer blends that have rubber-like behaviour but can be melt processed like thermoplastic polymers [89]. The combination of these properties is obtained by the two-phase structure of the materials: the soft phase, an elastomer, gives the material the rubber-like properties in the solid state whereas the hard phase, a thermoplastic polymer with a high glass-rubber transition temperature or a semi-crystalline polymer, gives strength to the blend. At the temperature of use, the stiffer phase acts as physical cross-linker for the elastomer phase. At elevated temperature (above the glass transition temperature or above the melting point), the hard phase softens and the TPE becomes processable.

TPEs may be classified into the following classes according to their chemistry and morphology [90]:

A. Block copolymers:
    1. Styrenic block copolymers (SBCs)
    2. Thermoplastic copolyesters (COPEs)
    3. Thermoplastic polyurethanes (TPUs)
    4. Thermoplastic polyamides (TPAs)
B. Blends:
    1. Thermoplastic polyolefin (TPOs)s
        a) Ethylene propylene diene rubber/polyolefins
        b) Natural rubber/polyolefines
    2. Nitrile rubber/polyvinyl chloride (NBR/PVC)
C. Elastomeric alloys (EAs):
    1. Thermoplastic vulcanisates (TPVs)
        a) EPDM rubber/polyolefins
        b) Natural rubber/polyolefins
        c) Nitrile rubber/ polyolefins
        d) Butyl rubber/ polyolefins

2. Melt-processable rubber(MPR)

D. Ionomers
   1. Sulfonated EPDM rubber(S-EPDM)
   2. Zn or Na salt of ethylene acrylic acids

TPEs consist of at least two polymeric phases, with the exception of melt-processable rubbers (MPRs), which are single-phase materials. The useful temperature range for a TPE is between the glass-transition temperature T_{g1} of the elastomeric phase and the melting point T_m or glass transition T_{g2} of the thermoplastic phase. Within this range, the TPE displays its elastomeric properties. At temperatures above T_m (T_{g2}) the hard phase melts (softens) and the TPE becomes fluid and can be processed by usual thermoplastic techniques. Below T_{g1} the material becomes brittle and loses all of its useful elastomeric characteristics.

The passage through T_{g1} and through T_m (T_{g2}) is reversible and can take place many times, since both are physical transformations. In the case of thermoset rubber, T_m (T_{g2}) does not exist, due to the thermoset nature of the material. Thus, the heating to progressively higher temperatures will not produce the melting of the material, but the onset of the irreversible chemical attack either from the environment or from internal decomposition.

The two phases may be present as alternating hard and soft segments along a common polymer backbone. This is the case for block copolymers, the basis for many commercially important TPEs. At temperatures below the effective T_m (T_{g2}) of the hard phase, the hard segments will aggregate into rigid domains, making the TPE a solid. At these temperatures, the soft segments are present as amorphous rubbery domains, which impart elastomeric nature to the TPE. The hard phase will restrict the motion of the soft phase segments, playing the role of physical cross-links.

The two phases may also result from simply mixing two different polymers, as in blends of a hard thermoplastic such as polypropylene with a soft elastomer such as ethylene-propylene terpolymer. Each of the polymeric components has its own phase, but the interaction between the phases is quite weak, if it exists at all. The hard phase must be continuous, or at least, co-continuous, in order for the blend to be thermoplastic and melt at T_m.

An EA consist of a finely divided (about 1 μm diameter) dispersion of highly cross-linked rubber particles in a continuous matrix of thermoplastic. The interfacial surface area between the two phases is sufficiently large to generate significant thermoplastic-elastomer interaction. The cross-linking of the elastomer phase prevents aggregation of the fine particles when the continuous phase becomes molten.

The newest class of TPEs are the ionomers. The physical cross-links in these materials are realised by complex formation. Anionic side groups are grafted on the elastomeric backbone and they form complexes with metallic cations.

Among the practical advantages offered by TPEs over thermoset rubbers, the following can be noted [91]:

- Processing is simple and requires fewer steps, with processing time cycles much shorter for TPEs, resulting in low energy consumption.
- TPEs offer the possibility of recovery and recycling.
- TPEs require little or no compounding with other materials. They are available fully compounded and ready for a wide range of uses.
- TPEs permit thermoplastic fabrication methods not feasible for thermoset rubbers. These methods include blow moulding, co-extrusion with rigid thermoplastics, thermoforming, heat welding and film blowing. These techniques improve the efficiency and cost of part fabrication and allow tighter control on part dimensions.

We have to mention that there are, also, disadvantages to the use of TPEs compared to thermoset rubbers [91,92]. Because the cross-links in the TPEs are physical in nature, the temperature range of application is limited. The presence of the hard phase limits the production of compounds with very low modulus (or low hardness). The elastic recovery of TPEs is not so good as of thermoset rubbers. Many TPEs require drying before processing. While this is a familiar step to thermoplastics processors, it is not necessary for thermoset rubbers.

The relative importance of each these advantages and disadvantages are weighted for each intended application. However, the rapid growth of TPEs during the last four decades indicates that in many instances the advantages of TPEs clearly prevail over their disadvantages. The next section presents some industrial applications of this special type of material.

4.2. Industrial applications

There is a growing interest for TPEs since they are not only good substitutes for thermoset rubbers in many existing applications, but also for new applications.

Styrenic TPEs and TPOs are widely used in nontire automotive applications such as exterior trim (bumpers, air dams, rub strips and weather stripping) or interior parts. For example, due to their better appearing and higher impact resistance, Solvay's Indure TPOs may be able to replace not only other engineering resins, but also steel and fibreglass parts. Unlike other TPOs that have a matte finish, these newly introduced materials can yield a high-gloss and scratch resistance to automotive parts. They can be pre-coloured to match any car colour, including metallics [93].

Higher performance TPEs such as EAs, COPs and TPUs find uses in the more fluid-resistant and thermally demanding under-the-hood automotive applications, where styrenics and TPOs are generally inadequate. For instance, Alcryn, from Advanced Polymer Alloys, is a crosslinked chlorinated olefinic interpolymer that mimics natural rubber's hydrocarbon- and wear-resistant properties [94]. Alcryn is used in

applications such as fuel lines, where material failure would be a catastrophe. It is also coextruded with PVC to form a gasket that most automakers use to hold windshields in place.

Transparent and low-tensile set biocompatible TPEs based on polysiloxane-modified polyolefin block copolymers and TPUs are finding applications in many medical contexts such as blood pump tubing, catheters, urethral stints, internal feeding sets, etc [95]. Vestamid nylon-12- based TPE films, from Degussa, are used as angioplasty balloons because of their durability and physical properties [96]. Eastman Chemical targets its copolyester TPEs exclusively at the medical market. The largest use is for intravenous bags that contain medications and nutritional supplements. Such bags have high strength and can resist puncturing, endure an autoclave, and withstand γ-ray sterilisation without discoloration [97].

TPEs are used extensively in wire and cable insulation. Low dielectric constant, high electrical resistance, high dielectric strength and low power factor make hydrogenated SBCs and EPDM/PP EAs especially useful in electrical applications.

The markets for pressure-sensitive adhesives, construction adhesives and sealants, product assembly adhesives, and hot melt-processable adhesives also developed from TPEs because they have the ability to achieve good adhesion while enjoying the inherent cost, safety and environmental advances of hot melt processing.

Major markets for SBCs include footwear, adhesives and sealants, asphalt modification, automotive sound-deadening foams, fibres and surgical gloves in which SBCs displace polyvinyl chloride.

4.3. The SEPS block copolymer (Hybrar 7125)

As mentioned before (section 2.2.1), it was initially decided to centre the research on the wear of polymer coatings devised for windmill blades, based on thermosetting polymer resins. We rapidly identified two problems with this type of material: 1) the difficulty to study the possible modifications induced by the ion implantation, because of the thermosetting nature of polymer resins and 2) the complexity of the test method used for artificial weathering of organic coatings formulated for windmill blades.

Therefore, we decided to focus instead on the wear of another class of materials, namely thermoplastic elastomers. The study of the wear resistance of such materials is of interest since they are used for shoe soles or other similar applications.

The selected polymer is an A-B-A type triblock copolymer, hydrogenated SIS poly(styrene-*block*-isoprene-*block*-styrene), i.e., it is a SEPS poly(styrene-*block*-(ethylene-*co*-propylene)-*block*-styrene), with the composition characteristics given in Table I-4 [98].

Relative fraction of hydrogenated isoprene	97%
Volume fraction of styrene in SEPS	13.1%
Fraction of structure 1,2 in the EP segment	33.6%
Fraction of structure 1,4 in the EP segment	66.4%

Table I-4. Composition characteristics of the polymer used

The microstructure of copolymer films of different thickness on silicon wafers was investigated using Atomic Force Microscopy (AFM). The details about this technique can be found in Chapter IV. The microstructure of the film surface, or at least its orientation, suffers a strong modification around 1.1 µm thickness. Below this value, the phase separation was not detectable with AFM. Above 1.1 µm thickness, polystyrene cylinders in a EP rubbery matrix were detected (Figure I-2). The cylinders are oriented parallel to the polymer-air interface.

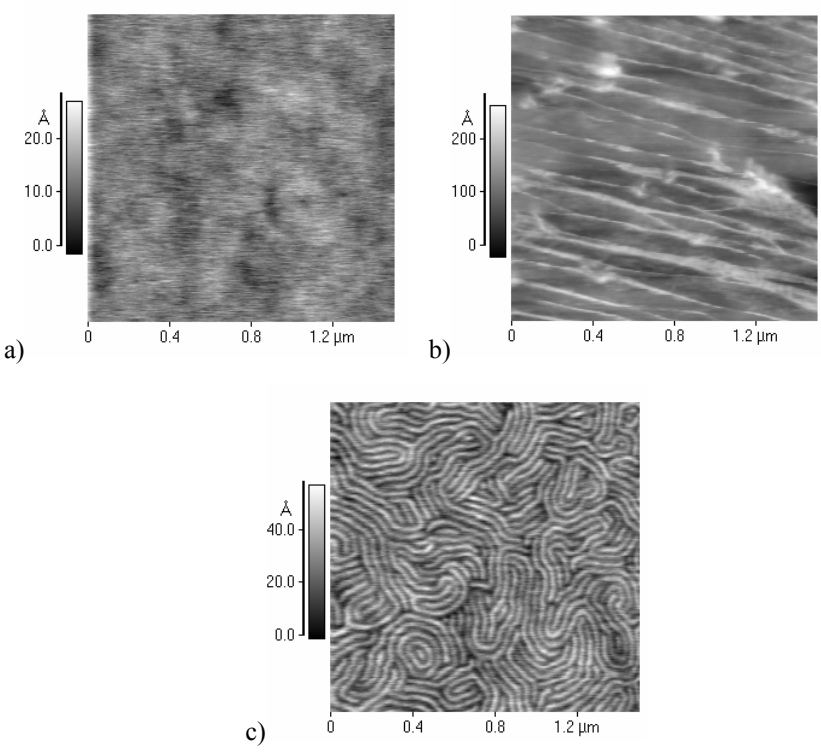

Figure I-2. Topographic (AFM) images of SEPS block-copolymer films on silicon substrate. Thickness: a) <1.1 µm, b)~1.1 µm and c) >1.1 µm.

To follow the microstructure modifications, the thickness selected for the samples used in the experiments directed to the study of physico-chemical modifications of the ion implanted samples was above 1.1 μm.

The glass transition temperature (T_g) was measured in house at 10 °C after rapid cooling, and a T_g of -17°C with a ΔCp of 0.3 J/gK was obtained. This T_g observed for SEPS is due to the glass transition of the ethylene-co-propylene (EP) and the importance of ΔCp indicates that these blocks are the major constituents of the copolymer. The T_g of the polystyrene part was difficult to measure , indicating again the small fraction of the polystyrene in the copolymer.

The information about the molecular weight of the copolymer was obtained by Size Exclusion Chromatography (SEC) in toluene and after two sets of measurements a narrow polydispersity of 1.06 and molecular weight values of Mn=(90292 ; 91243) Mw=(96116 ; 95982) and Mz=(100975 ; 100478) were obtained.

5. Thesis overview

The thesis is structured around main aspects of the radioactive ion implantation (RII) wear measuring technique (Figure I-3), as the only wear measuring method based on radionuclide techniques that is suitable for polymeric materials, as it was indicated in section 3 of the present chapter.

Research objectives

The general objective of the thesis is to test whether radioactive ions can be implanted in a controlled and non-destructive way in a soft polymeric material such as a thermoplastic elastomer. RII is an attractive method to control wear, but its application to polymers requires three conditions to be checked, as listed below:

When a sample is implanted with radioactive ions, the fundamental requirement is that the material properties remain unchanged. Otherwise, during the wear measurement, a different material would be tested, with erroneous results. Thus, one main objective is to establish experimentally if the implantation of the ^{7}Be radioactive ions in polymeric materials induces modifications in the material properties (wear resistance).

As already indicated (see section 3.1.3 of Chapter 1), the theoretical calibration (calibration curve) is a key aspect of the wear measuring method, allowing us to simplify considerably the wear measurement experiments mainly by offering the possibility to prepare properly the implantation for a given application. Therefore, another objective of the thesis is to verify whether it is possible to predict the experimental implantation profile in polymer materials by means of simulations.

Our third main objective is also related with this key aspect of the radioactive ion implantation wear measuring method, namely, to determine what happens with the ions immediately after the implantation and later, because, in order to have the same

calibration curve during the wear measurement, the implanted radioactive ions have to remain at their implantation place during the whole test.

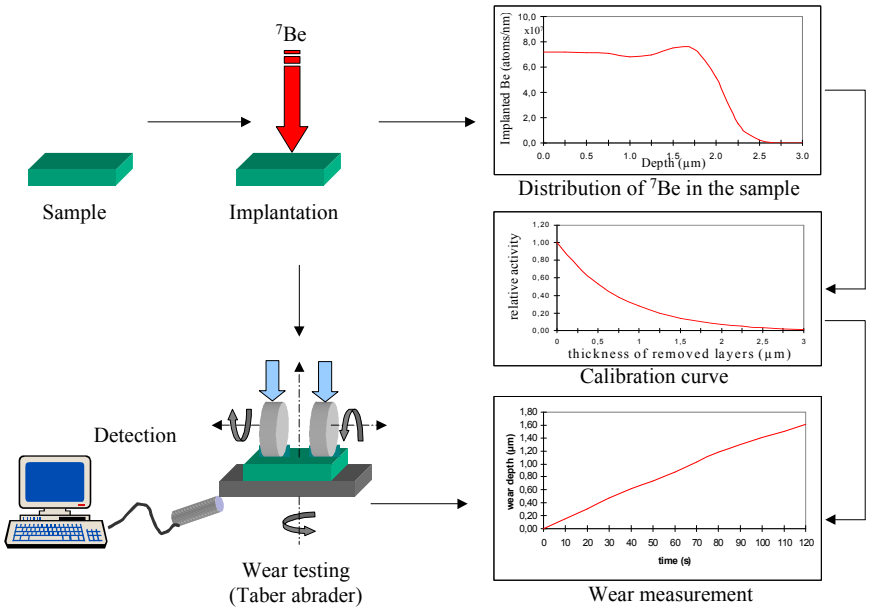

Figure I-3. General plan of a radioactive ion implantation wear measuring technique

As can be realized, these three objectives raise simultaneously scientific and technological issues. The thesis takes as starting point that separating technological from scientific issues would not be fruitful in the present case. Instead, our work will examine in parallel these two types of issues on materials that will be processed in a shape that will allow us to obtain relevant information using sophisticated analytical tools.

Outline of the thesis

In **Chapter II**, some theoretical considerations related to polymer-ion beam interactions, *implantation parameters* (ion type, energy, beam intensity, fluence), *micro-and macroscopic effects on the materials* are discussed.

A separate bibliographical review section is dedicated to the presentation of: experimental *techniques used to determine the implantation profiles*, some experimental results and theoretical aspects related to the *diffusion of ions implanted in polymers*.

In the case of RII wear measuring method, the implanted ions are radioactive, and this means that after implantation the material is exposed to radioactive emissions. *The radioactive decay of ^{7}Be ion* is also presented in **Chapter II**, together with a theoretical point of view on the *potential effects of the emitted radiations on the polymer*.

After the implantation step, the next important aspect is the *determination of the implantation profile, and implicitly, of the calibration curve*. Therefore, **Chapter III** is dedicated to the experimental study of the possibility to *predict the experimental implantation profile* by means of simulations with the Stopping and Range of Ions in Matter software (SRIM-2003) [99].

In Chapter III, the *implantation of a stack of copolymer films* and the *activity measurements performed to determine the implantation profile* is presented. The experimental results of the ion implantation profiles and calibration curves determination are presented and discussed in **Chapter III** in comparison with simulated results.

While Chapter II is dedicated to some theoretical considerations regarding physico-chemical modifications of ion implanted polymer materials, **Chapter IV** can be considered as a continuation of this subject, from an experimental point of view. Samples implanted with ^{7}Be, ^{7}Li and Kr ions were characterised by means of optical microscopy, Atomic Force Microscopy (AFM), Fourier Transform Infrared Spectroscopy (FT-IR) and X-ray Photoelectron Spectroscopy (XPS).

In **Chapter V**, the experimental study of the redistribution of the implanted ^{7}Be is presented. The main problem with all the existing experimental techniques is their detection limit. None of them is able to detect light elements (Li, Be, B) implanted in polymer targets at fluences less or equal to 10^{13} cm^{-2}, with implantation depths of a few μm. To our knowledge, so far, no studies were performed in order to establish if the Be^{7} ions diffuse after or during the implantation process.

In our study, Be^{7} ions were implanted with a known theoretical distribution in the copolymer material used in the previous experiments and plasma etching was used to remove layers of material. Thus, by measuring the thickness of the remaining layer and the corresponding remaining activity, the calibration curve can be reconstructed.

In the **Conclusions and perspectives** part, we review the contributions of the thesis, and list possible directions of future research.

6. References

1. ASTM G40-05 Standard Terminology Relating to Wear and Erosion, ASTM International, Book of Standards, Vol. 03.02.

2. A. Miszczyk, K. Darowicki, Effect of environmental temperature variation on protective properties of organic coatings, Prog. Org. Coat. 46 (2003) 49

3. J. Pospisil, S. Nespurek, Photostabilization of coatings. Mechanism and performance, Prog. Polym. Sci. 25 (2000) 1261.

4. L.F.E. Jacques, Accelerated and outdoor/natural exposure testing of coatings, Prog. Polym. Sci. 25 (2000) 1337.

5. H.F. Mark, N.M. Bikales, C.G. Overberger, G. Menges, Enciclopedia of polymer science and engineering, Vol. 17, Wiley, New York, 1989, p. 796-827.

6. R.D. Adams, M.M. Singh, The dynamic properties of fibre-reinforced polymers exposed to hot, wet conditions, Comp. Sci. Tehnol. 56 (1996) 977.

7. R. Uijlenhoet, J.N.M. Stricker, A consistent rainfall parameterization based on the exponential raindrop size distribution, J. Hydrol. 218 (1999) 101.

8. M. Lesser, Thirty years of liquid impact research: a tutorial review, Wear 186-187 (1995) 28.

9. W. Adler, Particulate impact damage predictions, Wear 186-187 (1995) 35.

10. C.F. Kennedy, A.R. Davies, J.E. Field, Erosion facilities at the Cavendish laboratory, The Cavendish Laboratory, June 2000.

11. R.J.K. Wood, The sand erosion performance of coatings, Mat. Design 20 (1999) 179.

12. J.J. Rajesh, J. Bijwe, U.S. Tewari, B. Venkataraman, Erosive behaviour of various polyamides, Wear 249 (2001) 702.

13. Y.I. Oka, H. Ohnogi, T. Hosokawa, M. Matsumura, The impact angle dependence of erosion damage caused by solid particle impact, Wear 203-204 (1997) 573.

14. ASTM G153-04 Standard Practice for Operating Enclosed Carbon Arc Light Apparatus for Exposure of Nonmetallic Materials, ASTM International, Book of Standards, Vol.14.04.

15. ASTM G154-04 Standard Practice for Operating Fluorescent Light Apparatus for UV Exposure of Nonmetallic Materials, ASTM International, Book of Standards, Vol.14.04.

16. ASTM G155-05a Standard Practice for Operating Xenon Arc Light Apparatus for Exposure of Non-Metallic Materials, ASTM International, Book of Standards, Vol.14.04.

17. ASTM G73-98 Standard Practice for Liquid Impingement Erosion Testing, ASTM International, Book of Standards, Vol. 03.02 .

18. ASTM G76-05 Standard Test Methods for Conducting Erosion Tests by Solid Particle Impingement Using Gas Jets, ASTM International, Book of Standards, Vol.03.02.

19. T.A. Adler, Ö.N. Dogan, Erosive wear and impact damage of high-chromium white cast irons, Wear 225-229 (1999) 174.

20. R.J.K. Wodd, D.W. Wheeler, Design and performance of a high velocity air-sand jet impingement erosion facility, Wear (1998) 95.

21. A.N.J. Stevenson, I.M. Hutchings, Scaling laws for particle velocity in the gas-blast erosion test, Wear 181-183 (1995) 56.

22. A.N.J. Stevenson, I.M. Hutchings, The influence of nozzle length on the divergence of the erodent particle stream in a gas-blast erosion rig, Wear 189 (1995) 66.

23. K.I. Rutherford, I.M. Hutchings, Development of the erosion durability technique for thin coatings, Surf. Coat. Technol. 86-87 (1996) 542.

24. P.H. Shipway, I.M. Hutchings, Measurement of coating durability by solid particle erosion, Surf. Coat. Technol. 71 (1995) 1.

25. T. Deng, M.S.A. Bradley, M.S. Bingley, An investigation of particle dynamics within a centrifugal accelerator type tester, Wear 247 (2001) 55.

26. T. Deng, M.S. Bingley, M.S.A. Bradley, Influence of particle dynamics on erosion test conditions within the centrifugal accelerator type erosion tester, Wear 249 (2001) 1059.

27. C. Westmark, G.W. Lawless, A discussion of rain erosion testing at the United States Air Force rain erosion test facility, Wear 186-187 (1995) 384.

28. A.A. Déom, A. Luc, S. Amara, D.L. Balageas, Towards more realistic erosion simulation tests for high velocity EM and IR windows, Wear 233-235 (1999) 13.

29. W.F. Adler, Rain impact retrospective and vision for the future, Wear 233-235 (1999) 25.

30. B.W. Johnson, R. McIntyre, Analysis of test methods for UV durability predictions of polymer coatings, Prog. Org. Coat. 27 (1996) 95.

31. V. Shah, Handbook of plastics testing tehnology, Wiley, New York, 1984, p. 129-140

32. X.F. Yang, D.E. Tallman, G.P. Bierwagen, S.G. Croll, S. Rohlik, Blistering and degradation of polyurethane coatings under different accelerated weathering tests, Polym. Degrad. and Stability 77 (2002) 103.

33. A.W. Signor, M.R. VanLandingham, J.W. Chin, Effects of ultraviolet radiation exposure on vinyl ester resins: characterisation of chemical, physical and mechanical damage, Polym. Degrad. and Stability 79 (2003) 359.

34. G.P. Bierwagen, D.E. Tallman, Choice and measurement of crucial aircraft coatings system properties, Prog. Org. Coat. 41 (2001) 201.

35. M.E. Nichols, J.L. Gerlock, C.A. Smith, Rates of photooxidation induced cross-linking and chain scission in thermoset polymer coatings-I, Polym. Degrad. and Stability 56 (1997) 81.

36. M. Osterhold, P. Glockner, Influence of weathering on physical properties of clearcoats, Prog. Org. Coat. 41 (2001) 177.

37. J.E. Field, ELSI conference: invited lecture Liquid impact: theory, experiment, applications, Wear 233-235 (1999) 1.

38. G.H. Jilbert, J.E. Field, Synergistic effects of rain and sand erosion, Wear 243 (2000) 6.

39. I.M. Hutchings, M.G. Gee, Critical evaluation of erosive wear testing, NPL Report MATC(D)02, Jan. 2001.

40. A.J. Burnett, S.R. De Silva, A.R. Reed, Comparisions between “sand blast” and “centripetal effect accelerator” type erosion testers, Wear 186-187 (1995) 168.

41. A.J. Burnett, M.S.A. Bradley, D.J. O’Flynn, T. Deng, M.S. Bingley, Anomalies in the results obtained from rotating disc accelerator erosion testers: a discussion of possible causes, Wear 233-235 (1999) 275.

42. H.F. Mark, N.M. Bikales, C.G. Overberger, G. Menges, Enciclopedia of polymer science and engineering, Vol. 1, Wiley, New York, 1985, p. 1-35.

43. L. Zsidai, P. De Baets, P. Samyn, G. Kalacska, A.P. Van Peteghem, F. Van Parys, The tribological behaviour of engineering plastics during sliding friction investigated with small-scale specimens, Wear 253 (2002) 673.

44. H.C. Meng, K.C. Ludema, Wear models and predictive equations; their form and content, Wear 181-183 (1995) 443.

45. T.A. Tervoort, J. Visjager, P. Smith, On abrasive wear of polyethylene, Macromolecules 35 (2002) 8467.

46. S.E. Franklin, Wear experiments with selected engineering polymers and polymer composites under dry reciprocating sliding conditions, Wear 251 (2001) 1591.

47. M.C. Dubourg, A. Chateauminois, B. Villechaise, In situ analysis and modeling of crack initiation and propagation within model fretting contacts using polymer materials, Tribol. Int. 36 (2003) 109.

48. S.W. Zhang, State-of-the-art of polymer tribology, Tribol. Int. 31 (1998) 49.

49. M. Chandrasekaran, A.W. Batchelor, In situ observation of sliding wear tests of butyl rubber in the presence of lubricants in an X-ray microfocus instrument, Wear 211 (1997) 35.

50. F.J. Buchanan, P.H. Shipway, Microabrasion - a simple method to assess surface degradation of UHMWPE following sterilisation and ageing, Biomaterials 23 (2002) 93.

51. S. Ramachandra, T.C. Ovaert, The effect of controlled surface topographical features on the unlubricated transfer and wear of PEEK, Wear (1997) 94.

52. J. Schöfer, E. Santner, Quantitative wear analysis using atomic force microscopy, Wear 222 (1998) 74.

53. R.I. Trezona, D.N. Allsopp, I.M. Hutchings, Transition between two-body and three-body abrasive wear: influence of test conditions in the microscale abrasive wear test, Wear 225-229 (1994) 205.

54. Y. Fukahori, H. Yamazaki, Mechanism of rubber abrasion. Part 3: how is friction linked to fracture in rubber abrasion?, Wear 188 (1995) 19.

55. L.C. Seabra, A.M. Baptista, Tribological behaviour of food grade polymers against stainless steel in dry sliding and with sugar, Wear 253 (2002) 394.

56. A.C.-M. Yang, T.W. Wu, Wear and friction in glassy polymers: microscratch on blends os polystyrene and poly(2,6-dimethyl-1,4-phenylene oxide), J. Pol. Science 35 (1998) 1295.

57. P.H. Shipway, N.K. Ngao, Microscale abrasive wear of polymeric materials, Wear 255 (2003) 742.

58. I.M. Hutchings, Abrasive and erosive wear tests for thin coatings: a unified approach, Tribol. Int. 31 (1998) 5.

59. ASTM F2025-06 Standard practice for gravimetric measurement of polymeric components for wear assessment, ASTM International, Book of Standards, Vol. 13.01.

60. ASTM F1714-96(2002) Standard guide for gravimetric wear assessment of prosthetic hip-designs in simulator devices, ASTM International, Book of Standards, Vol. 13.01.

61. ISO Standard, Implants chirurgicaux – Prothèses partielle et totale de hanche – Recommandations pour l'évaluation en laboratoire du changement de forme des surfaces articulaires, ISO/TR 9326 :1989.

62. P.M. Racolta, Nuclear methods for tribology, J. Appl. Rad. Isot. 46 (1995) 663.

63. D.C. Eberle, C.M. Wall, M.B. Treuhaft, Applications of radioactive tracer technology in the real-time measurement of wear and erosion, Wear 259 (2005) 1462.

64. M. Scherge, K. Pöhlmann, A. Gerve, Wear measurement using Radio-Nuclide-Techniques (RNT), Wear 254 (2003) 801.

65. P.M. Racolta, L. Popa-Simil, B. Alexandreanu, Ion beam-based studies for tribological phenomena, Nucl. Instr. and Meth. in Phys. Res. B 113 (1996) 420.

66. O. Lacroix, T. Sauvage, G. Blondiaux, P.M. Racolta, L. Popa-Simil, B. Alexandrescu, Metrology conditions for thin layer activation in wear and corrosion studies, Nucl. Instr. and Meth. in Phys. Res. A 369 (1996) 427.

67. G. Blondiaux, E. Dragulescu, P.M. Racolta, R. Stroosnijder, Experiments to establish the optimum beam parameters for wear and corrosion measurements, Report WP9 IDRANAP 13-01/2001

68. T. Sauvage, O. Lacroix, G. Blondiaux, P. Boyer, Implantation of ^{7}Be radioactive tracer for wear measurements of polymers, Nucl. Instr. and Meth. in Phys. Res. B 143 (1998) 397.

69. F. Ditroi, I. Mahunka, Thin layer activation of non metallic materials by using nuclear implantation, Nucl. Instr. and Meth. in Phys. Res. B 113 (1996) 415.

70. F. Ditroi, S. Takacs, F. Tarkanyi, I. Mahunka, Study of the ^{nat}C(^{3}He, 2α)^{7}Be and ^{9}Be(^{3}He, αn)^{7}Be nuclear reactions and their application for wear measurements, Nucl. Instr. and Meth. in Phys. Res. B 103 (1995) 412.

71. M. Hoffmann, K. Abbas, T. Sauvage, G. Blondiaux, L. Vincent, M.F. Stroosnijder, ^{7}Be recoil implantation for ultra-thin-layer-activation of medical grade polyethylene: Effect on wear resistance, Nucl. Instr. and Meth. in Phys. Res. B 183 (2001) 419.

72. M. Loiselet, G. Berger, D. Breyne, Th. Daras, H. Goffaux, N. Postiau, G. Ryckewaert, J. Ryckewaert, Production and acceleration of radioactive beams at Louvain-la-Neuve, 14th International Conference on Cyclotrons and their Application, Cape Town, South Africa, 1995, World Scientific,1996 , p629

73. G. Ryckewaert, J.M. Colson, M. Gaelens, M. Loiselet, N. Postiau, Recent results from the Louvain-la-Neuve RIB-facility, Nucl. Phys. A 701 (2002) 323.

74. M. Gaelens, M. Cogneau, M. Loiselet, G. Ryckewaert, Post-acceleration of ^{7}Be at the Louvain-la-Neuve radioactive ion beam facility, Nucl. Instr. and Meth. in Phys. Res. B 204 (2003) 48.

75. U. Köster, M. Argentini, R. Catherall, V.N. Fedoseyev, H.W. Gäggeler, O.C. Jonsson, R. Weinreich, Off-line production of intense ^{7,10}Be^{+} beams, Nucl. Instr. and Meth. in Phys. Res. B 204 (1997) 343.

76. L. Gialanella, U. Greife, N. De Cesare, A. D'Onofrio, M. Romano, L. Campajola, A. Formicola, Z. Fulop, G. Gyurky, G. Imbriani, C. Lubritto, A. Ordine, V. Roca, D. Rogalla, C. Rolfs, M. Russo, C. Sabbarese, E. Somorjai, F. Strieder, F. Terrasi, H.P. Trautvetter, Off-line production of a ^{7}Be radioactive ion beam, Nucl. Instr. and Meth. in Phys. Res. B 197 (2002) 150.

77. P.Fehsenfeld, C. Eifrig, R. Kubat, Application of RNB for high sensitive wear diagnostics in medicine technique and industry, Nuclear Physics A 701 (2002) 235c.

78. K. Abbas, D. Gilliland, M.F. Stroosnijder, Radioactivity measurements for the thin layer activation technique, Applied Radiation and Isotopes 53 (2002) 179.

79. L. Vincent, T. Sauvage, O. Lacroix, M. Saillard, G. Blondiaux, L. Guinard, Simplified methodology of the ultra-thin layer activation technique, Nucl. Instr. and Meth. in Phys. Res. B 190 (2002) 831.

80. L. Vincent, T. Sauvage, O. Lacroix, J. Fradin, M. Saillard, Ultra thin layer activation by implantation of recoil radioactive nuclei : Experiments and simulations, Nucl. Instr. and Meth. in Phys. Res. B 161-163 (2000) 115.

81. E.W. Schneider, D.H. Blossfeld, Radiotracer method for measuring real-time piston-ring and cylinder-bore wear in spark-ignition engines, Nucl. Instr. and Meth. in Phys. Res. A 505 (2003) 559.

82. P.M. Racolta, L. Popa-Simil, B. Alexandreanu, L. Mateescu, Thin layer activation-based evaluation of tribological behaviour of light-ion implanted metallic samples, Nucl. Instr. and Meth. in Phys. Res. B 127/128 (1997) 949.

83. N. Manderlier, T. Delvigne, Quality control by autoradiography for the thin layer activation technique, Nucl. Instr. and Meth. in Phys. Res. B 213 (2004) 523.

84. A. Gervé, W. Lausch, J. Volz, Radionuklidtechnische Verfahren zur Ermittlung des Ölfilterrückhaltegrades für Verschließteilchen und deren Größenverteilung, MTZ 40 (1979) 339.

85. A. Gauthier, T. Delvigne, Soot induced cam wear in diesel engines: an investigation using Thin Layer Activation, SAE Paper, 2000-01-1990, 2000.

86. G. Wallace, K.P. Pohl, E.F. Hutchinson, I.D. Hemmingsen, The application of thin layer activation for on-line erosion monitoring, J. Appl. Rad. Isot. 55 (2001) 281.

87. V.A.C. Haanappel, Y.P. Jacob, M.F. Stroosnijder, The use of thin layer activation in high-temperature cyclic oxidation studies, Corros. Sci. 44 (2002) 1411.

88. M.F. Stroosnijder, M. Hoffmann, T. Sauvage, G. Blondiaux, L. Vincent, Wear evaluation of a cross-linked medical grade polyethylene by ultra thin layer activation compared to gravimetry, Nucl. Instr. and Meth. in Phys. Res. B 227 (2005) 597.

89. G. Holden, N. Legge (eds.), Thermoplastic elastomers, Hanser, New York, 1996.

90. N.K. Dutta, A.K. Bhowmick, N.R. Choudhury, in O. Olabisi (ed.), Handbook of thermoplastics, chap.15, Marcel Dekker, New York, 1997.

91. R.L. Arnold, C.P. Rader, in C.A. Harper (ed.), Handbook of plastics, elastomers and composites, 2nd ed., chap.7, McGraw-Hill, 1992.

92. A.K. Bohwmick, H.L. Stephens (eds.), Handbook of elastomers, Marcel Dekker, New York, 2001.

93. www.solvayengineeredpolymers.com/indure.htm.

94. http://www.apainfo.com/product_family/alcryn_mpr/index.html.

95. P.A. Isaqcs, Elastomer alloys in medical products reduce costs and toxicity concerns, Elastomerics 121 (1989) 26.

96. http://www.degussa-hpp.com/eng/products/hpp/vestamid_e.shtml.

97. http://www.eastman.com/markets/pharmaceutical/packaging.

98. X. Stassart, Caractérisation de mélanges de polyoléfines et de SEPS, Mémoire de fin d'etudes, UCL, 2003.

99. www.srim.org.

Chapter II
Ion implantation – some theoretical considerations

1. Introduction

The study of physical and chemical modifications induced by ion implantation in polymeric materials has caught the attention of researchers for technological as well as for basic scientific reasons. Ion implantation under different conditions can improve mechanical, electrical, optical, chemical and biocompatibility properties of polymers. The modification of the polymer properties is due both to the presence of the implanted impurities that changes the polymer composition, and to the irradiation effects initiated by them, which modify the polymer structure and chemistry.

In the case of radioactive ion implantation (RII) wear measuring method, the opposite situation is desired. When the sample is implanted with radioactive ions, the fundamental requirement is that the material properties remain unchanged. Otherwise, during the wear measurement a different material would be tested, with erroneous results. Therefore, in order to keep the modifications induced in the polymer sample as low as possible, the implantation parameters (ion type, energy, beam intensity, fluence) have to be selected with care.

In the first part of this chapter, we focus on the polymer-ion beam interaction. Micro- and macroscopic effects on polymer materials are discussed. The three main parameters used for the characterisation of the phenomena are introduced: the nuclear and electronic stopping power and the range. A separate bibliographical review section is dedicated to the presentation of: experimental techniques used to determine the implantation profiles, some experimental results and theoretical aspects.

In the case of RII wear measuring method, the implanted ions are radioactive, and this means that after implantation the material is exposed to radioactive emissions. The radioactive decay of ^{7}Be ion is presented, together with a theoretical point of view on the potential effects of the emitted radiations on the polymer.

2. Interactions between ion beams and polymers: ion irradiation and ion implantation

The basic requirements for performing any study in this field are, of course, energetic ions. They can be obtained in many ways, e.g., by making use of radioactive sources such as α particle or fission product emitters, or by exploiting nuclear reactions, e.g., with neutrons from a reactor, that result in the emission of protons, tritons, α particles or fission products, depending on the type of irradiated material. Other nuclei become available by bombardment of swift heavy ions onto appropriate target materials, via various types of nuclear reactions such as fusion reactions, spallation reactions, etc. Finally, for obtaining particles with the highest energies, one even can make use of the sporadically arriving cosmic rays [1]. The easiest way nowadays, however, to obtain particles with sufficient fluence in a "convenient" energy range of some keV to some GeV, is to produce them in an appropriate particle accelerator.

In conventional ion irradiation devices, an ion beam is extracted from a plasma source, accelerated to the desired energy, and then transported to the target. Typical beam currents are very small (in the microampere range) and the beam "footprint" area is less than 1 cm^2. To process large-scale targets, and to avoid shadowing if the target is non-planar, a combination of beam rastering and target manipulation during the process is required.

2.1. Phenomena and specific parameters

2.1.1. Energy loss mechanisms

When an energetic particle penetrates into a polymer medium, it loses energy by two main processes, namely, by interacting with target nuclei (screened) and by interacting with target electrons. The former process is called nuclear energy loss (nuclear stopping) and the latter electronic energy loss (electronic stopping) [2].

Nuclear energy loss arises from collisions between the energetic particle and target nuclei, which cause atomic displacements and phonons. Nuclear energy loss by inelastic collision (nuclear reactions) is not considered here. Displacement occurs when the colliding particle imparts energy greater than a certain displacement threshold energy, E_d, to a target atom. Otherwise, knock-on atoms cannot escape their sites and their energy dissipates as atomic vibrations (i.e., phonons). E_d is the energy that a recoil requires to overcome the binding forces and to move more than one atomic spacing away from its original site.

Since the nuclear collision occurs between two atoms with electrons around protons and neutrons, the interaction of an ion with a target nucleus is treated as the

scattering of two screened particles. Nuclear stopping is derived with consideration of the momentum transfer from ion to target atom and the inter-atomic potential between two atoms. Thus, nuclear stopping varies with ion velocity as well as the charges of two colliding atoms.

Nuclear stopping becomes important when an ion slows down to approximately the Bohr velocity (orbital electron velocity). For this reason, the maximum nuclear energy loss occurs near the end of the ion track for high-energy ions. The Bohr velocity can be derived from the uncertainty principle as:

$$V_B \approx \frac{1}{4\pi\varepsilon_0}\frac{e^2}{\hbar} \approx 2.2\times 10^6 \quad m/s, \tag{II.1}$$

where ε_0 is the permitivity constant, e is the unit charge and $\hbar$ is Planck constant divided by 2π.

Nuclear collisions create recoil atoms, these recoil atoms also lose their energy through nuclear and electronic processes until all excited electrons and atoms are thermalised by dissipating energy through phonons and plasmons. For most ion energy ranges of interest, nuclear stopping by small atoms such as H or He is negligible because the Rutherford cross-section and momentum transfer by the low mass atoms is small. Nuclear stopping, however, becomes important for ion species with a large number of nucleons [3].

Electronic energy loss arises from electromagnetic interaction between the positively charged ion and the target electrons. One mechanism is called glancing collision (inelastic scattering, distant resonant collisions with small momentum transfer) and the other is called knock-on collision (elastic scattering, close collisions with large momentum transfer). Both glancing and knock-on collisions transfer energy in two ways: electronic excitation and ionisation. All excited electrons (plasmons) eventually lose energy as they thermalise. Glancing collisions are quite frequent but each collision involves a small energy loss (<100 eV). On the other hand, knock-collisions are very infrequent but each collision imparts a large energy to a target electron (>100 eV). These knock-on electrons are often called δ-rays or secondary electrons. Theoretical and experimental evidence suggested that approximately one-half of the electronic energy loss is due to glancing collisions and the other half to knock-on collisions [3].

Electronic stopping is determined mainly by the charge state of the ion and its velocity. When an ion passes through a medium, its orbital electrons are stripped off in varying degree depending upon the ion velocity (V_{ion}). The effective charge on a positive ion is given, in terms of ion velocity and Bohr velocity (V_B) [4] as:

$$Z^*_{eff} = Z\left[1 - a\exp(-b\frac{V_{ion}}{V_B}Z^{-2/3})\right], \tag{II.2}$$

where Z is the atomic number, and a and b are fitting constants.

He-ions are almost completely stripped to an average charge of +2 at around 1 MeV. The higher the Z, the higher the energy required to fully strip an atom.

In conclusion, the stopping of ions penetrating through matter is governed by a number of scattering processes such as excitation of target electrons, electron capture, projectile excitation and ionisation, ionisation of target atoms and recoiling nuclei [4]. The relative significance of these processes depends primarily on the speed and the atomic number of the penetrating ion and to some extent on target parameters and projectile state.

2.1.2. Stopping power

The most important parameter in understanding the effects of the nuclear and electronic processes in materials is the energy deposited per unit ion path length, linear energy transfer (LET) or stopping power (S).

The stopping power is the sum of electronic and nuclear contributions,

$$S = \frac{dE}{dx} = \left(\frac{dE}{dx}\right)_{elect.} + \left(\frac{dE}{dx}\right)_{nucl.} = S_{elect.} + S_{nucl.} \qquad \text{(II.3}$$

Accurate stopping power values are important in the development of different applications, not only in elements but also in multi-element targets, for example polymers. In view of the great number of ion-elemental target combinations and wide energy range of potential interest it does not appear feasible to adequately cover the entire parameter space with experimental data. This implies that theory is indispensable.

The mainstream research may be conveniently be classified by keywords like [5]: electronic and nuclear stopping, high-speed and slow ions, light and heavy ions, bare and screened ions, elemental and compounds targets, insulators and conductors, etc. Regimes of ion stopping may be categorised primarily in terms of projectile speed and atomic number. On the other hand, several significant effects depend on the atomic number of the target. A qualitative survey of stopping regimes for light and heavy target has been presented [6,7].

Two empirical models have been advanced to infer the stopping power of multi-element targets [8]. Bragg's rule calculates the stopping power of compound targets from the weighted average of stopping powers of pure elemental targets:

$$S_{compound} = \sum_i (c_i S_i) \qquad \text{(II.4}$$

where c_i is the atomic fraction of the element i and S_i the stopping power of this element. As example, for polystyrene (C_8H_8), Bragg's rule is derived from the stopping power of pure carbon and hydrogen and can be written as:

$$S_{PS} = \frac{1}{2}(S_C + S_H) \qquad \text{(II.5}$$

The core-and-bonds (CAB) model is specifically designed for organic materials. In this model, each molecule is described as a set of atomic cores and bonds, corresponding to the non-bonding core and bonding valence electrons, respectively. In the case of polystyrene, which consists of eight carbon cores, six carbon-carbon single bonds, three carbon-carbon double bonds and eight carbon-hydrogen bonds, the stopping power can be expressed as:

$$S_{PS} = 8S_{C(1s)} + 6S_{C-C} + 3S_{C=C} + 8S_{C-H} \qquad \text{(II.6}$$

The values for the stopping contribution of each type of core or bond have been tabulated [9].

As a result of the huge theoretical work, computer codes for the calculation of stopping powers, simulation of range and damage distribution even in three dimensions appeared [10,11]. The most known one among them, maybe because of its availability, is the TRIM code (Transport and Range of Ions in Matter). The computer software base on this code is named SRIM – The Stopping and Range of Ions in Matter software [12].

SRIM is a group of programs that calculate the stopping and range of ions (10 eV - 2 GeV/amu) into matter using the theory of ion-atom collisions. During collisions, the ion and atom have a screened Coulomb collision, including exchange and correlation interactions between the overlapping electron shells. The ion also has long-range interactions with target atoms creating electron excitations and plasmons within the target. These are described by including a description of the target's collective electronic structure and interatomic bond structure when the calculation is setup. The charge-state of the ion within the target is described using the concept of effective charge, which includes a velocity dependent charge state and long-range screening due to the collective electron sea of the target [13].

Most of the experimental information on stopping power has been obtained by transmission and backscattering techniques or combination of them [14]. With the transmission techniques, the energy loss of particles passing trough thin self-supporting films is determined. This allows for a direct determination of the stopping power if the thickness of the foil is known [15]. In the backscattering method, the energy spectrum of ions scattered by a target is measured [8,16]. Stopping powers are then extracted from a detailed analysis of these spectra. An alternative method is the derivation of stopping powers from the range measurements by differentiating the range-energy curves [17].

Usually solid-state detectors are used for the recording of the particle spectra [18]. The energy loss of the ion beam may be determined by means of magnetic field measurements in the magnetic spectrographs [19,20] or spectrometers [21]. Another accurate method is the calorimetric technique [22]. In this method, the energy loss of the ions can be measured directly instead of energy difference. The time-of-flight technique is a powerful method for determining the energy loss when low energy particles are employed [23,24,25]. The stopping power is determined by measuring the ion velocity with and without the sample foil in position.

Small sections of the experimentally obtained stopping power curves may be approximated by various expressions as a function of incident ion energy E. In regions well above the stopping power curve maximum, the expression

$$S(E) = B\frac{\ln(\beta E)}{E} \qquad \text{(II.7}$$

is generally applied [26]. Here, B and β are factors which depend on the ion and target material atomic number and mass.

At the regions close to the curve maximum, different relations for the stopping power are used, for example polynomial.

$$S(E) = \sum_{i=0}^{m} k_i E^i \qquad \text{(II.8}$$

where k_i are the fitting parameters. The order of the polynomial may be five [24, 27] or six [28].

At the low energy regime, the expression:

$$S(E) = kE^p \qquad \text{(II.9}$$

with k and p fitting parameters, was used with success in fitting stopping power values for alpha particles from 60 to 240 keV in polymer targets [29].

An extended interpolation formula, based on the previous ones, was also proposed [16]:

$$S(E) = \frac{E^{\frac{1}{2}}\ln(e+\beta E)}{\alpha_0 + \alpha_1 E^{\frac{1}{4}} + \alpha_2 E^{\frac{1}{2}} + \alpha_3 E^{\frac{3}{4}} + \alpha_4 E + \alpha_5 E^{\frac{3}{2}}} \qquad \text{(II.10}$$

Here both low and high energy asymptotic forms $S \sim E^p$ with $p=1/2$ and $S \sim \ln(\beta E)/E$, respectively are built in.

2.1.3. Range and range straggling

One of the most important considerations in any description of ion-solid interactions is the depth distribution (range) of the implanted ions. A large amount of experimental and theoretical work has been devoted to the task of understanding the energy-loss processes that govern the distribution, and now it is possible to predict quite accurately most of the factors involved.

The range distribution of an ensemble of monoenergetic projectiles, incident under a given direction in a thick layer of matter, is defined as the probability of finding the projectiles at rest after complete slowing down. In good approximation the mean range R of heavy ions in matter can be calculated within the continuous-slowing-down model [30],

$$R(E) = \int_0^{E_0} (dE/dx)^{-1}\, dE \qquad \text{(II.11}$$

where E_0 is the incident kinetic energy and dE/dx is the total stopping power.

Because the incident ion is deflected by elastic collisions with the target nuclei, its path is not straight. Different geometrical range concepts may be defined [31]. The total range R_{tot} of an ion is the total path length penetrated in the medium, the vector range R_v is the vector between the entrance point and stopping point and the projected range R_p is the normal projection of the vector range on the starting direction (Figure II-1). Angular deflection causes the lateral range $R_\perp$, which is the lateral distance from the incident direction. The lateral and the projected ranges add up to the vector range ($R_v^2 = R_p^2 + R_\perp^2$). For many applications, R_p is the relevant observable.

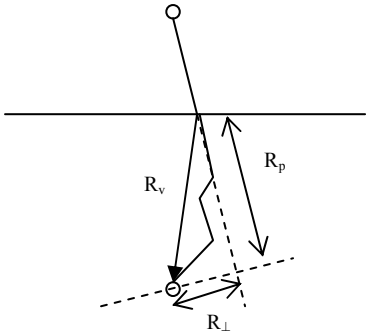

Figure II-1. Vector range R_v, projected range R_p and lateral range $R_\perp$ for an incident particle in matter

The statistical nature of energy deposition and angular scattering determines the range distribution of an ensemble of ions entering the medium [32]. Variations in the

range from ion to ion arise because of statistical fluctuations in the energy losses in elastic collisions and in the direction of the ion after a collision. Those collisions that involve greater energy transfers also involve greater deflections. The inelastic collisions are assumed to constitute a smooth braking force, and hence, do not contribute to the straggling in range.

Range distributions can be calculated within the framework of transport theory. A good approximation for the variance of the range distribution for incident monoenergetic and collimated ions is the following relation based on equation II.11 [31]:

$$\Omega_R^2(E) = \int_0^{E_0} \frac{d\Omega^2 / dx}{(dE/dx)3} dE \qquad \text{(II.12}$$

In this equation, the differential energy straggling $d\Omega^2/dx$ is the sum of variances of the different energy straggling contributions.

Typically, interactions follow a statistical process, and the implanted profile is often approximated by a Gaussian distribution as follows [33]:

$$N(x) = N_p \exp\left(\frac{-(x - R_p)^2}{2\Delta R_p}\right) \qquad \text{(II.13}$$

where the average distance an ion travels before it stops is called the projected range R_p. The peak concentration N_p occurs at a range of R_p. Because of the statistical nature of the process, some ions will obviously penetrate beyond the projected range R_p and some will not travel as far as R_p. The spread of the distribution of the implanted ions is characterized by the standard deviation ΔR_p and is called the straggle. The area under the Gaussian distribution curve is the implanted fluence ϕ:

$$\phi = \int_0^{\infty} N(x)dx \qquad \text{(II.14}$$

The experimental determination of the range is strongly linked to the study of redistribution phenomena of implanted ions; therefore, it will be presented in the section 4.1.

2.2. Physico-chemical modifications

2.2.1. Primary phenomena

During irradiation, various physical and chemical processes take place in the polymer. Nuclear collisions cause atomic displacements, which can then lead to

chain scission or release of pendant atoms. Superposition of phonon waves can also lead to bond breakage, but the probability of such events is small because phonons have insufficient energy density to start with. Polymers have a large free volume, often larger than 20%, and atomic density in such a loose system is relatively small compared to that in a medium with a compact lattice structure, such as a metal. Therefore, in polymers, most nuclear displacements occur independently. The probability to cause simultaneous displacement of two atoms from neighbouring chains and create two radical pairs for cross-linking is small in nuclear processes [3].

On the other hand, when the electronic LET is high, a considerable volume around the ion projectile is influenced because of the coulombic field produced by glancing collisions and ionisation (δ-rays) by knock-on collisions. The result is the production of active chemical species, cations, anions, radicals, and electrons along the polymer chains [34]. Coulombic attraction and repulsion among these active species cause violent bond stretching and segmental motion in the polymer chains, which can then lead to cross-linking as well as bond breakage [35].

Thus, both electronic and nuclear energy transfers can induce cross-linking as well as scission. However, as pointed out above, nuclear stopping causes more scission due to the nature of independent displacement damage and the simultaneous production of two radicals in neighbouring chains is low. On the other hand, electronic stopping cause more cross-linking due to collective excitation (plasmons), which produces a large excited volume thereby resulting in coercive interaction among the ions and radical pairs produced within the volume [36].

Whereas the individual nuclear collisions lead to a deviation of the projectile flight direction from its original one, this is not the case for electronic energy transfer. Hence, for projectiles with dominant nuclear energy transfer, the particles will follow a zig-zag movement until they come to rest. This gives rise to a spatially extended damage distribution. For contrast, projectiles with dominant electronic energy transfer follow a straight flight path. The damaged zone around that ion trajectory is called the "latent ion track". The zone of maximum damage along this track is called "ion track core", surrounded by a radial zone of greatly reduced damage, the "penumbra" [1].

Various gaseous molecular species are released during irradiation. The most prominent emission is hydrogen, followed by less abundant heavier molecular species, which are scission products from the pendant side groups and chain-end segments, and their reaction products [37,38]. The gaseous products reflect both the atomic composition and the molecular structure of the polymers.

The volatile, gaseous degradation products may migrate to the sample surface and eventually escape from the sample. Taking a rather conservative estimate of $D=10^{-10}$ cm^2/s as a diffusion constant of small gaseous molecules in pristine polymers and typical irradiation times $T=10^3$-10^4 s, diffusion distances $((DT)^{-1/2}$ larger than few microns results, which are sufficient for most degradation products to reach the sample surface during the implantation [39].

The outward migration of the degradation products may be enhanced by the pressure gradient between the sample interior and the vacuum in the implanter target chamber. On the other hand, diffusion may be hindered by the trapping of some migrating species on the radiation defects produced in near surface by the ion irradiation.

By measuring the pressure rise in the irradiation chamber during the bombardment of poly(methyl methacrylate), PMMA films with a variety of high energy ions a strong dependence on fluence and on ion type was observed [40]. In another study, numerous molecular species, liberated during irradiation of PMMA with 2 MeV He^+ and Ar^+ ions, were recorded by a residual gas analyser [36]. Twenty-nine peaks were identified below mass number 50 for both ions, but the relative peak intensity differed for each mass depending upon the employed ion species, even though the same 2 MeV was deposited for both cases.

The formation of unsaturated sites is another important structural change induced by irradiation. Unsaturation is primarily due to loss of adjacent substituents on the chain or side group (for instance H atoms in polyethylene) or to radical-radical termination reactions that occur by disproportionation. Double bonds, once formed, may subsequently participate in cross-linking reactions via radical addition.

After exposing the irradiated polymers to air, oxygen penetrates to the surface layer of the polymer and participates in the reactions of free radicals up to the formation of stable oxygen-containing groups.

The equations below outline the reactions in radiation-induced oxidation [41].

$$R \xrightarrow{irrad.} R\cdot \qquad \text{Initiation} \qquad \text{(II.15}$$

$$\left.\begin{aligned} R\cdot &\xrightarrow{O_2} RO_2\cdot \\ RO_2\cdot &\xrightarrow{RH} RO_2H + R\cdot \end{aligned}\right\} \text{Propagation} \qquad \text{(II.16}$$

$$\left.\begin{aligned} RO_2H &\rightarrow RO\cdot + \cdot OH \\ RO\cdot &\xrightarrow{RH} ROH + R\cdot \\ \cdot OH &\xrightarrow{RH} H_2O + R\cdot \end{aligned}\right\} \text{Chain branching} \qquad \text{(II.17}$$

$$RO_2H,\ RO_2\cdot,\ R\cdot \rightarrow \qquad \text{Scission and cross-linking} \qquad \text{(II.18}$$

$$2RO_2\cdot \rightarrow RO_2R + O_2 \qquad \text{Termination} \qquad \text{(II.19}$$

Because of its high diffusional mobility and its high reactivity toward radicals, oxygen serves to trap radicals in an efficient manner, greatly impeding the radical reaction that occur in absence of oxygen, and channelling the course of the reactions into predominantly oxidative routes. Chemical oxidation products include oxidised structures within the polymer, such as ketone, carboxylic acid, and alcohol functionalities as well as peroxide species. Gaseous products include those arising

under inert-atmosphere irradiation, together with significant amounts of CO_2, CO and H_2O. The intensity of the oxygen reaction and the concentration of the formed groups are determined by the concentration of the initial free radicals and their distribution [42-44].

Due to the relatively poor thermal conductivity of polymers, the ion-beam heating of polymer is more restricted to the ion-irradiated regions. The diffusional dissipation of the thermal energy do not occur as rapidly as, e.g., in metals so that the local overall thermal load may become severe in the case of high-flux irradiations. To reduce the thermal load, an efficient heat removal is necessary. Therefore, it is appropriate to fix the polymeric target as tightly as possible to massive metallic holders, and to use polymer films as thin as possible. Furthermore, the ion flux should be kept low enough to avoid excessive target heating [45].

A general parameter used to describe the effects of an ionising radiation in a polymeric target is the chemical yield, G – number of events produced per 100 eV of absorbed energy. The G values depend on the type of polymer and of irradiation [46].

2.2.2. Parameters influencing physico-chemical modifications

The characteristic parameters affecting ion-polymer interactions are the ion type (size), ion energy, ion fluence, and the composition of the target. These parameters determine the amount of energy delivered, the relative importance of the energy deposition mechanism and the penetration range of the impinging ions or the thickness of the modified layer.

In order to illustrate the discussion, we use results of calculation made with the SRIM simulation software. Three ions types were selected for the simulations ^{7}Li, ^{7}Be and ^{84}Kr. The reason for this choice is that in our implantation experiments we used these three types of ions. In this way, the importance of the atomic mass (7 for ^{7}Li and ^{7}Be and 84 for ^{84}Kr) and atomic number (3 for ^{7}Li, 4 for ^{7}Be and 36 for ^{84}Kr) on the physico-chemical modifications of the polymer materials can be pointed up. The target material selected for the simulations is polypropylene, because his density of 0.9 g/cm^3 is the same as the density of the copolymer used in our implantation experiments.

To a first approximation, the projected range R_P depends on the ion mass and incident energy, whereas the relative width $R_p/\Delta R_p$ of the distribution depends primarily on the ratio between the ion mass and the target atom mass [33]. The range curves of ^{7}Li, ^{7}Be and ^{84}Kr ions as a function of ion energy in a polypropylene target, calculated with SRIM, are presented in Figure II-2.

For a given projectile ion, at low energies nuclear stopping is dominant, while electron stopping dominates at high energies as shown in the stopping power curves

of ^{7}Be ions in polypropylene (Figure II-3). As the atomic number of the ion increases for a fixed target, the energy values corresponding to the maximum of two curves shift to higher numbers.

Generally, for light ions and large values of incident ion energy, the predominant mode of energy transfer is electronic energy loss [47]. For heavy ions and relatively low energy values, the nuclear mode of energy transfer predominates.

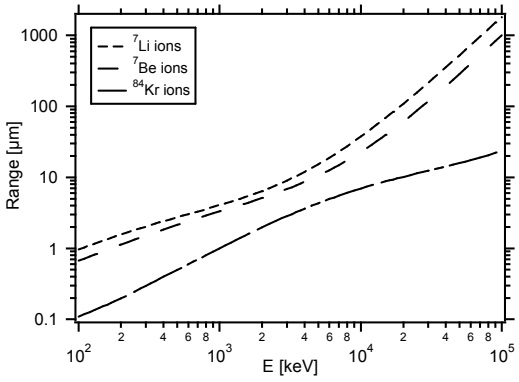

Figure II-2. Range of ^{7}Li, ^{7}Be and ^{84}Kr ions as a function of ion energy in a polypropylene target (SRIM calculation)

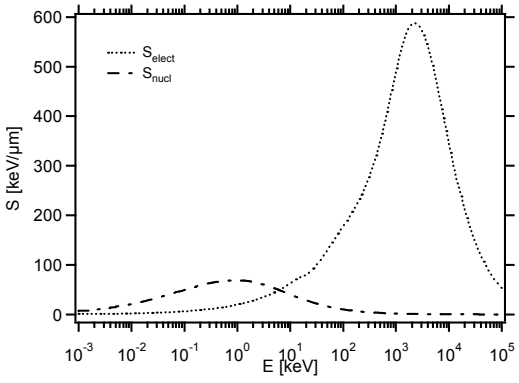

Figure II-3. Electronic and nuclear stopping power of ^{7}Be in polypropylene as a function of ion energy (SRIM calculation)

Figure II-4 illustrates the variation of the stopping powers as a function of ion energy for the three ion types: ^{7}Li, ^{7}Be and ^{84}Kr in a polypropylene target, calculated with SRIM. The crossover point for incident ^{7}Li ions is 6 keV, for ^{7}Be ions is approximately the same, 6 keV, but for ^{84}Kr it is roughly 800 keV.

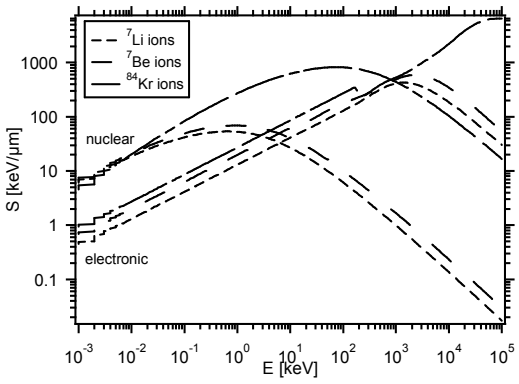

Figure II-4. Nuclear and electronic stopping powers of ^{7}Li, ^{7}Be and ^{84}Kr in a polypropylene target as a function of ion energy (SRIM calculation).

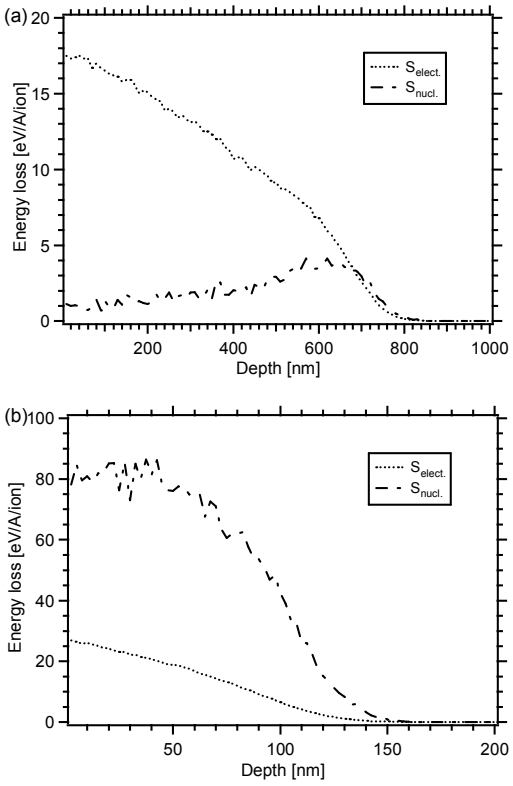

Figure II-5. Nuclear and electronic stopping power profiles of 100 keV (a) ^{7}Be and (b) ^{84}Kr ions in polypropylene (SRIM calculation)

The maximum values for S_{nucl} and their position, indicate also the different importance of the nuclear energy loss processes for the three ions types: from 53.7 keV/µm at 0.65 keV for ^{7}Li and 69.1 keV/µm at 1keV for ^{7}Be, to 822 keV at 80 keV for ^{84}Kr ions.

In Figure II-5, nuclear and electronic stopping power profiles calculated with SRIM are presented as a function of the depth in the polypropylene sample for ^{7}Be and ^{84}Kr ions at 100 keV initial energy. We can observe that in the case of ^{7}Be (Figure II-5.a), the energy loss by means of nuclear processes becomes significant only in the second part of the ion path. For ^{84}Kr ions (Figure II-5.b), the situation is completely different. At the entrance in the polypropylene sample, S_{nucl} is roughly three times larger than S_{elect} and this ratio increases along the ion path, thus, at the end it becomes almost seven times larger.

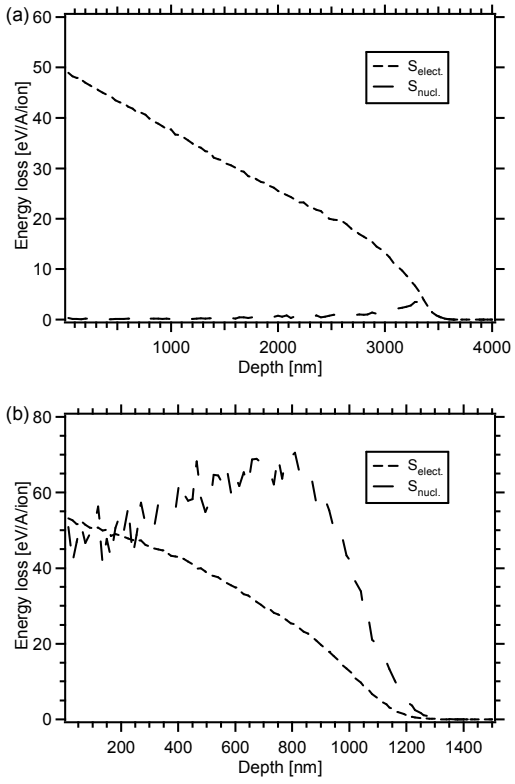

Figure II-6. Nuclear and electronic stopping power profiles of 1000 keV (a) ^{7}Be and (b) ^{84}Kr ions in polypropylene (SRIM calculation).

The difference between the implantation of the two ions becomes more visible at 1000 keV initial ion energy (Figure II-6). For ^{7}Be ions, the S_{nucl} becomes comparable with the S_{elect} only in the last 400 nm, which represents around ~10% of the ion range (Figure II-6.a). For the ^{84}Kr ions in the same conditions (Figure II-6.b),

the nuclear stopping remains the principal energy loss mechanism lengthways the ion path.

Another important parameter that influences the effects induced in a target material by the ion implantation is the number of implanted ions per cm^2, namely the ion fluenceϕ. With the increase of the fluence, the radiation effect (electronic and nuclear stopping) is enhanced.

For example, in the case of nuclear stopping processes, most nuclear displacements occur independently at low dose, due to the low atomic density (see Section 2.2.1 of this chapter). Therefore, the probability to cause simultaneous displacement of two atoms from neighbouring chains and create two radical pairs for cross-linking is small. The increase in ion fluence leads to the formation of more active bonds that connect with each other and the degree of cross-linking increases [34]. It is the case of PMMA, that at low fluence value show main-chain scission type comportment although at high fluence cross-linking becomes the main effect of the implantation.

A generally accepted conclusion is that chain scission predominates at lower fluences and cross-linking predominates at higher fluences [48].

Sometimes another parameter is used, the energy density or dose D *(eV/cm^3),* that may be defined as the product of ion fluence ϕ and energy loss S:

$$D = \phi \cdot S \qquad \text{(II.20}$$

Effects induced by different types of ions or by the same ion at different initial energies (so different stopping powers) may be compared using the energy density.

The chemical composition is strongly influencing the behaviour of the target material during the ion-polymer interactions. C-H bonds break more frequently than C-C bonds, in spite of the lower bond energy of the latter. This behaviour has been attributed to excitation energy transfers along the macromolecular chain preventing main chain scission, whereas C-H bond scission is favoured by the localisation of the excitation [49]. Some "weak" bonds result in enhanced bond cleavages. Thus, carboxylic acids generate large yields of CO_2, amines generate NH_3, and so on. The presence of chlorine 'sensitise' radiolysis, whereas aromatic groups tend to 'protect' the molecule [36].

Generally, polymers subjected to radiation degradation in the absence of oxygen can be grouped into two categories, those in which cross-linking predominates and those in which chain scission is predominant (Table II-1). A general empirical rule was derived [2]. When the structure of a vinyl polymer is such that each carbon atom of the main chain carries at least one hydrogen atom, the polymer is of cross-linking type. Alternatively, if a tetrasubstituted atom is present in the monomer unit, the polymer is a chain scission polymer. Steric inhibition of radical-radical recombination following chain break, leading to an increased yield of scission, is the most likely explanation of this phenomenon.

Cross-linking polymers	Chain scission polymers
Polyethylene	Polyisobutylene
Polypropylene	Poly (α-methylstyrene)
Polystyrene	Polymethacrylates
Polyacrylates	Polymethacrylamide
Polyacrylamide	Poly (vinylidene chloride)
Poly(vinyl chloride)	Cellulose and derivatives
Poly(vinyl alcohol)	Polytetrafluoroethylene
Polyamides	Polytrifluorochloroethylene
Polyesters	Poly(vinyl fluoride)
Polyvinylpyrrolidone	Poly(propylene sulphide)
Rubbers	
Polysiloxanes	
Polyacroleine	
Polybutadiene	
Poly(styrene-*co*-butadiene)	
Polyurethanes	
Poly(ethylene terephthalate)	
Polyimide	

Table II-1. Classification of polymers according to their predominant degradation mode when irradiated in an inert atmosphere [41].

The behaviour of these two groups of polymers is recognised in microlithography. Polymer of the main-chain scission type are designated as 'positive' resists, because the irradiated zones dissolve more easily than the unirradiated domains, whereas polymers of the cross-linking type are called 'negative' resists because the irradiated zones becomes less soluble (or less susceptible to plasma etching).

Polymers of the cross-linking type may undergo main-chain scission if irradiated in the presence of air, or if irradiated without prior deaeration, since oxygen is dissolved in the original polymer [36].

2.2.3. Macroscopic modifications

It has been well established that mechanical, physical, and chemical property changes in polymers are determined by the magnitude of cross-linking and scission, and that cross-linking enhances mechanical stability while scission degrades mechanical strength. Cross-linking produces strong chemically bonded networks, increases rigidity of the backbone structure, provides anchoring points for the chains and restrains chain movement, thus improving dimensional stability, hardness and elastic modulus[50], as well as wear resistance [51,52] and decreases solubility in chemical solvents [53,54].

Radiation-induced degradation, such as deformation of formerly expanded polymer chains due to the loss of volatile fragments and formation of double and triple bonds initiates their clustering to arrive at energetically favoured geometrical shapes. Radiation induced cross-linking may connect several such compacted chains to clusters [55]. Electrons of impurity bands, in such cluster embedded in a polymer will easily shift to the conduction band. Size and density of these clusters hence determine the electrical conductivity [56,57]. They also influence the optical properties of the material. Continuous addition of chains by cross-linking during the irradiation initiates cluster growth until they touch.

The appearance of polymers may change with dose, from transparent to white, light brown and finally black [58]. Whitening of the surface implies an increase in light scattering owing to roughening of the surface. The refractive index of the material is changed by the ion irradiation, and the modification profile generally follows the electronic stopping power profile in the sample [59,60].

The formation of crosslinked and carbon-rich structures in the surface area during the implantation process was observed by measuring the surface roughness modification using Atomic Force Microscopy [61] and a strong dependence of the surface morphology on the applied ion fluence was observed [62]. In some cases, cracking of the polymer film and/or peeling of the film from the substrate contribute to the roughening of the surface [63].

The crystallinity degree of a polymer is changed substantially by ion irradiation. Different studies shown that an ion bombarded semicrystalline polymer gradually loses its ability to crystallise and over a critical ion fluence, the chain becomes completely amorphous [64]. The drop in crystallinity from about 46% for the unimplanted sample to a relatively constant value of 19% for the implanted sample, with further decrease to 13% occurring at high fluence was observed in the case of poly(ethylene terephthalate) (PET) implanted with 6 MeV oxygen ions [58].

3. Redistribution of the implanted ions

In contrast to ion implantation into metals, semiconductors or ceramic materials, where the implanted ions distribute according to the theoretically predicted distributions, for polymeric targets strong deviations from the expected range profiles are frequently observed. It is accepted that these profiles result from diffusional redistribution of the as-implanted particles, their mobility being influenced by the defects in the polymer.

In the case of RII wear-measuring method, the calibration curve is obtained from the distribution of the ions in the sample (see Chapter I, section 3.1.3). Any inconsistency in the determination of the implantation profile will induce errors in the results of the wear measurement.

Therefore, we considered important to review briefly the field of experimental determination of range profiles. In the coming sections, we will present the possible experimental techniques used in the determination of the implanted ion distributions, their principles and limitations. Theoretical aspects linked to the redistribution of the implanted ions at room temperature will be also considered. We have to note that there is no universal theory able to explain all the experimental results.

3.1. Possible experimental techniques

Depth profile techniques provide a measure of the concentration profile perpendicular to the sample surface. Particle beams are particularly suited for this analysis because of their specific interaction with matter. The four analytical techniques based on the ion beam-sample interaction, suitable for impurity depth profile determination will be presented further on.

Rutherford Backscattering Spectrometry (**RBS**) is the most frequently used IBA method. The RBS experiment consists of a monoenergetic beam of ions, typically 1-2 MeV He ions that are focused on a sample. As the ions traverse the sample, they interact with the sample atoms and loss a well-defined amount of energy that is proportional to the travelled distance. At some depth in the sample, the ion can undergo a scattering event and the backscattered ion loses more energy as it travels out of the sample. Again, the energy loss is proportional to the distance.

The backscattered ions are energy analysed by a solid-state particle detector, positioned at a backscattered angle with respect to the incident ion beam (typically between 100° and 170° depending on the specific analysis). The energy of the backscattered ions are dictated by conservation of energy and momentum between the incident ion and the target atom and can be related to the depth and mass of the target. The amount of backscattered ions from any given element is proportional to its concentration. Therefore, RBS can be used as a tool to investigate quantitatively the depth profile of impurities in a solid [65].

Elastic Recoil Detection Analysis (**ERDA**) or **Forward Recoil Spectrometry** (**FReS**) is used if light elements in heavy substrates or elements lighter than the incident beam particles have to be detected. In this case, after the collision event, the incident ion can not be backscattered, but will continue in the forward direction. The target atom will be recoiled and expelled from the sample and can be detected in grazing angle geometry [65].

In order to discriminate between forward scattered projectiles and different types of recoiling particles, absorber foils or mass discriminating detectors have to be used. The great advantage of ERDA with a mass (or nuclear charge) discriminating detector is that the depth profiles of all light target elements can be obtained simultaneously well separated from each other. Ionisation chambers, combined silicon and time-of-flight detectors and combined magnetic and/or electrostatic spectrometers can be used [66-69].

The principle of **Nuclear Reaction Analysis** (**NRA**) is that MeV ion beams can induce nuclear reactions in the target nuclei. In the energy range accessible to accelerators used for materials analysis (up to ~50 MeV) this is especially the case of light projectiles impinging on light to medium heavy atoms. The yield and energy of the emitted charged reaction products (p,n,d, α, ^{3}He, etc.) are measured by surface barrier detectors. Comparing the emission intensity with that of a known standard leads to the quantitative determination of the concentration of the specific element in the target. The emitted particles lose energy as they exit the film; this energy loss provides a direct measurement of the depth of the originating nucleus.

Suitable reactions can be found for the analysis of virtually all elements up to mass 30. For heavier nuclei, only scarce reactions exist. Some examples of nuclear reactions suitable for NRA are: ^{7}Li(p,α)^{4}He, ^{11}B(p,α)^{8}Be, ^{12}C(d,p)^{13}C, ^{15}N(p,α)^{12}C, ^{19}F(p,α)^{16}O [70].

A particular case of NRA is the **Neutron Depth Profiling** (**NDP**) technique where the samples are placed in a beam of cold neutrons that induce capture reactions. For example, lithium depth profiles can be determined by the measurement of the energy of alpha particles and/or tritons from the ^{7}Li(n,α)^{3}He reaction [71].

Secondary Ion Mass Spectrometry (**SIMS**) is a surface analytical technique in which a sample is bombarded under vacuum with ions with energies of typically 0.5-25 keV. These primary ions strike and penetrate the surface setting the atoms into motion. Some of the atoms set into motion will strike nearby particles, ejecting them off the sample and into the vacuum. A portion of these atoms or molecules will have a net electrical charge, hence the term "secondary ion". The secondary ions are then accelerated in an electrostatic field to several keV and separated on the basis of their mass. SIMS analyses are typically divided in two modes, dynamic and static SIMS. **Dynamic SIMS** involves bombarding the surface continuously with an ion beam and monitoring elemental concentrations as a function of depth. SIMS depth profiling has become a well-established technique for characterising implantation profiles [72,73].

We have to mention also that **X-ray Photoelectron Spectroscopy** (**XPS**) or **Auger Electron Spectroscopy** (**AES**) can also been used for depth profile analysis when accompanied by ion sputtering [74,75].

The main problem with all the existing techniques is their detection limit. None of them is able to detect light elements (Li, Be, B) implanted in polymer targets at fluences less or equal to 10^{13} cm^{-2}, with implantation depths of a few μm. From the point-of-view of radioactive ions implantation for wear measurement, where the fluences are kept as low as possible (10^{10}-10^{11} cm^{-1}) in order to avoid material degradation and for radioprotection reasons, this value is much too high.

3.2. Bibliographic review of experimental results and theoretical aspects

It has been observed that, after implantation of monoenergetic ions into polymers at room temperature, the implanted ions do not always distribute strictly according to their theoretically predicted implantation profiles. A fraction of ions, after being stopped ballistically along their implantation profiles and probably neutralised, might be able to diffuse in the material. The position of the gaussian peak may differ from the predicted one, a broadening can also be observed, and in some cases, the shape of the distribution can be strongly different from the theoretical one [76,77]. It was observed that these modifications depend on the ion type (size and nature), implanting energy and fluence.

When studying diffusion processes it is important to distinguish between thermal and radiation-enhanced diffusion, which takes place either during, or immediately after ion implantation. In the first case, the intrinsic and thermally created free volume promotes the atomic transport, whereas, in the second case, the radiation-induced excess free-volume enables the non-thermal transport. The polymeric excess free volume may be created, for example, by the loss of the volatile components (see section 2.2.1). It is expected not to collapse immediately but to undergo some thermal migration during which the transport of embedded impurities is enabled [78].

Light ions such as Li, B and N implanted into polymers at room temperature and low fluences often redistribute partially, according to the shapes of the depth profiles of the energy transferred in electronic excitation and ionisation [79,80]. The redistributed fraction depends on the projectile energy and atomic number, hence on the stopping power and on the fluence [81,82]. The target material is also a strongly influencing factor.

For light ions, in general, the redistributed profiles can be characterised by a superposition of a regular profile and an other that has an additional tail directed towards the surface; in some cases, a gradual transition between these two curve shapes can be observed [79]. This redistribution appears to be induced by the radiation, rather than a thermal mobility of the implanted ions, because subsequent annealing hardly affects the ion distribution any longer [83].

In some cases, both electronic and nuclear depth profiles are influencing the redistribution of the implants. For example, in the photoresist S1813, approximately a 1:1 ratio is found between ^{10}B ions trapped at nuclear and at electronic defects [84]. Taking into account the 10 times lower abundance of nuclear defects, this signifies a ten times higher trapping efficiency of the nuclear defects than that of electronic damage sites.

Heavy ions such as Cs, Hg, Au, Pb, Ag and others do not show this type of redistribution at room temperature under low fluence implantation [85-87]. In most cases, only heavy noble gases have been found to redistribute partially after the implantation into polymers at room temperature. In general, the experimental

distributions are shorter than the theoretically predicted, which might be attributed either to a compactation effect of the irradiated polymer layer [88], or to a diffusional redistribution according to the depth profiles of their nuclear energy transfer [89]. An additional tail towards the bulk indicates that part of the implanted material remains mobile after the implantation [90].

Even more striking deviations from the theoretical predictions appear at fluences exceeding 10^{15} cm^{-2}. Here, sputtering, the material progressive carbonisation, density changes and crack formation start playing a non-negligible role [76,91]. In general, the implanted profiles roughly resemble the theoretically expected distributions of nuclear damage, rather than those of the theoretical ion range or electronic damage distributions. It has been shown that boron atoms, which at low fluences redistribute according to their electronic energy transfer distributions, at high implantation fluences follow the nuclear energy distribution [92].

In order to explain the redistribution of the implanted ions according to the electronic or nuclear energy loss profile, the concept of mobile and trapped impurities in the presence of saturable and unsaturable traps has been introduced in polymeric diffusion theory [79].

Electronic defects (excited atoms or ions) do not create any excess free volume and often have a limited lifetime due to the recombination processes (i.e. short-range electronic and ionic transport processes). As electronic defects are no longer chemically active after bonding with an impurity, they act as saturable traps.

Defects introduced by nuclear collisions (recoil atoms, vacancies, voids and microcavities) appear to exhibit long-term stability and they are unsaturable traps. The collision-based free volume might attract more than one ion, which may be chemically reactive or inert such as a noble gas ion. At low fluences, the nuclear trapping efficiency vanishes rapidly upon annealing, possibly indicating a thermally stimulated self-repair process which releases the trapped impurities. At high fluences the nuclear traps exhibit a high trapping efficiency, and this probably indicates that at these fluences the nature of the nuclear defects changes. Larger voids are maybe formed, which exhibit more stability against the polymer self-repair phenomenon, or increasing cross-links of the neighbouring polymer diminish the polymer chain mobility [93].

The theory of saturable and unsaturable traps can be probed via post-diffusion experiments of dopants in implanted polymers [94,95]. For example, in air, ion-implanted polymers undergo spontaneous oxidation (see section 2.2.1). Investigation of the oxygen distribution in the polymer provides a significant information on the structure of the implanted layer since the trapped oxygen decorates the regions of high concentration of dangling carbon bonds produced in the course of implantation [96]. For light ions with fluences below 10^{16} cm^{-2} the oxygen depth profiles are generally coincident with the electronic loss distribution [91]. On the contrary, the oxygen depth profiles for the samples implanted with heavy ions to the fluence of 10^{13}-10^{14} cm^{-2} turn out to be more similar to that of nuclear losses.

Another possible explanation is that dynamical changes of the polymer structure and composition, such as cross-linking, chain scissions, carbonisation and double bond formations, alter the nature of the material, inducing changes in the stopping power values [97]. These modifications may be reflected in range distributions completely different from the theoretical ones.

In conclusion, that there is so far no universal theory able to explain all the experimental results. This implies that the redistribution of the ions should be carefully evaluated for each material of interest.

4. Radioactive ion implantation, the special case of radioactive emissions

The basis of the RNT wear measuring methods is the implantation of radioactive ions in the sample to be studied, so that wear processes can be characterised by a loss of material assessed by radioactivity measurements. When implanting radioactive ions in a polymer, beside the possible modifications induced by the ion implantation, the effects of the emitted radiation on the material properties have to be considered.

In this section, we present some basic aspects linked to the radioactive decay, and the case of the ^{7}Be radioisotope is detailed. The principles of the interaction between γ and X-rays emitted by ^{7}Be and polymers are also presented.

4.1. The radioactive decay

Radioactive decay is the set of various processes by which unstable atomic nuclei emit subatomic particles (radiation). Decay is said to occur in the parent nucleus and produces a daughter nucleus. The decay modes are presented in Table II-2.

Typically one decay mode predominates for a particular nuclide. Branching ratios are used when this is not true.The branching ratio is the probability that a nucleus will decay into a specific mode.

Radioactive decay is a statistical process which depends upon the instability of the particular radioisotope, but which for any given nucleus in a sample is completely unpredictable. Each atom lives for a finite amount of time before it decays, and the mean lifetime is the arithmetic mean of all the atoms lifetimes. The probability per second that a nucleus will decay, λ, is known as the **decay constant**, and is related to the atoms mean lifetime τ, by:

$$\lambda = \frac{1}{\tau} \qquad \text{(II.21}$$

A more commonly used parameter is the **half-life** $T_{1/2}$. Given a sample of a particular radionuclide, the half-life is the time taken for half the radionuclide atoms to decay. The half life is related to the decay constant as follows:

$$\lambda = \frac{\ln 2}{T_{1/2}} \qquad \text{(II.22}$$

Mode of decay	Principle	Emitted particle	Daughter nucleus
Decays with emission of nucleons:			
Alpha decay	An alpha particle emitted by the nucleus	α	(A-4,Z-2)
Proton emission	A proton ejected by the nucleus	p	(A-1,Z-1)
Neutron emission	A neutron ejected by the nucleus	n	(A-1,Z)
Spontaneous fission	Nucleus disintegrates into two or more random smaller nuclei	(A_x,Z_y)	
Cluster emission	Nucleus emits a specific type of smaller nucleus larger than an alpha particle	(A_1,Z_1)	(A-A_1,Z-Z_1) + (A_1,Z_1)
Different modes of beta decay:			
Beta decay	A nucleus emits an electron and an antineutrino	e^-, $\bar{\nu}$	(A,Z+1)
Positron emission	A nucleus emits a positron and a neutrino	e^+, ν	(A,Z-1)
Electron capture	A nucleus captures an orbiting electron and emits a neutrino	ν	(A,Z-1)
Electron capture with positron emission	A nucleus absorbs one orbital electron, emits one positron and two neutrinos	e^+, 2ν	(A,Z-2)
Double beta decay	A nucleus emits two electrons and two antineutrinos	$2e^-$, $2\bar{\nu}$	(A,Z+2)
Double positron emission	A nucleus emits two positrons and two neutrinos	$2e^+$, 2ν	(A,Z-2)
Double electron capture	A nucleus absorbs two orbital electrons and emits two neutrinos	2ν	(A,Z-2)
Transition between states of the same nucleus:			
Gamma decay	Excited nucleus releases a high-energy photon (gamma ray)	γ	(A,Z)
Internal conversion	Excited nucleus transfers energy to an orbital electron and ejects it	-	(A,Z)

Table II-2. Radioactive decay modes

The **activity** (**A**) of a material is defined as the number of decays per unit of time. The international (SI) unit for activity is becquerel (Bq). One becquerel is equal to one nuclear transformation per second. Another unit used is curie (Ci).

$$1\ Ci = 3.7 \cdot 10^{10}\ Bq \qquad \text{(II.23}$$

The activity of a particular material depends on the total number of radioactive nuclei N existing at the given moment of time and on the decay constant λ.:

$$A = -\frac{dN}{dt} = \lambda N \qquad \text{(II.24}$$

The negative sign indicates that N decreases with each decay event. The solution to this first-order differential equation is the following function:

$$N(t) = N_0 e^{-\lambda \cdot t} \qquad \text{(II.25}$$

or, by multiplication with λ:

$$A(t) = A_0 e^{-\lambda \cdot t} \qquad \text{(II.26}$$

4.2. ^{7}Be radioactive decay

Beryllium is a rare, hard, light metallic element in the second column of the periodic table, an alkaline earth element. Its nucleus contains four protons, and the usual stable form also contains five neutrons, and thus has a mass number of nine. ^{7}Be is a lighter isotope of beryllium with a mass number of seven, with only three neutrons in its nucleus.

The production of ^{7}Be in the sun is a result of a very small branch of the proton-proton chain $^{3}He(\alpha,\gamma)^{7}Be$. ^{7}Be is formed in the atmosphere by the interaction of cosmic rays with nitrogen and oxygen, for example via $^{14}N(n,^{8}Li)\ ^{7}Be$ and $^{14}N(p,2\alpha)\ ^{7}Be$ reactions [98]. It is a very reactive element and attaches instantaneously to particulate material, for example atmospheric aerosol particles [99].

In laboratory conditions, ^{7}Be is produced via several nuclear reactions, among which we can enumerate:

$^{7}Li(p,n)\ ^{7}Be$ [100-102] or $p(^{7}Li,\ ^{7}Be)n$ [103]

$^{10}B(p,\alpha)\ ^{7}Be$ [104] or $p(^{10}B,\ ^{7}Be)\alpha$ [105]

$^{11}B(d,\alpha n)\ ^{7}Be$ [104]

$^{9}Be(^{3}He,\alpha n)\ ^{7}Be$ [106,107]

$^{12}C(^{3}He,2\alpha)\ ^{7}Be$ [107]

^{7}Be is unstable and decays to ^{7}Li by electron capture, with a half-life of 53.3 days, or equivalently an average lifetime of 77 days. If the energy difference between initial and final states is low (less than 1.022 MeV), the electron capture can occur without being accompanied by positron emission [108]. It is the case of ^{7}Be decay. Here, one of the orbital electrons, from the K or L electron shell (K-capture, or L-capture) [109,110], is captured by a proton in the nucleus, forming a neutron and a neutrino [111]:

$$p^{+} + e^{-} \rightarrow n^{0} + \nu \qquad \text{(II.27}$$

Since the proton is changed to a neutron, the number of neutrons increases by 1, the number of protons decreases by 1, and the atomic mass number remains unchanged. By changing the number of protons, electron capture transforms the nuclide into a new element, ^{7}Li. The atom moves into an excited state with the inner shell missing an electron. An outer shell electron falls into the inner shell and emit X-rays and/or Auger electrons.

In 89.6% of the decays the ^{7}Be nucleus goes to the ^{7}Li ground state, with a maximum detectable energy of 112 eV, which is the limit for the traditional detection techniques. In 10.4% of the decays the ^{7}Be nucleus go to a 478 keV excited state of ^{7}Li. In this case, electron capture decay is followed, with a half-life of 73 fs, by the emission of a 478 keV γ ray [112,113]. In Figure II-7 the ^{7}Be decay scheme is shown.

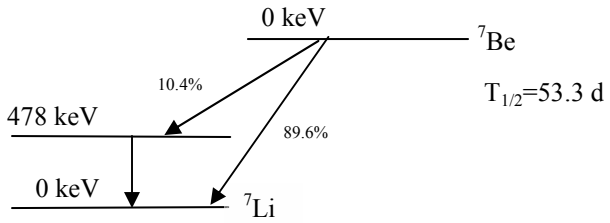

Figure II-7. The ^{7}Be electron capture decay scheme

It is of note that radioactive isotopes which decay by pure electron capture can be inhibited from radioactive decay if they are fully ionized (stripped). Chemical bonds can also affect the rate of electron capture to a small degree depending on the proximity of electrons to the nucleus [114-116].

4.3. Electromagnetic radiation and matter

When high energy photons, such as γ or X rays penetrate a material energy is deposited by three ionisation mechanisms: the photoelectric effect, Compton scattering and pair production. The energy of the incident radiation and the atomic

composition of the absorbing medium determine which of the above mechanisms predominate.

By the photoelectric effect, a photon is absorbed and an orbital electron is ejected, having the energy of the incident radiation minus the binding energy.

In Compton scattering, an incident gamma photon looses enough energy to an orbital electron to cause its ejection, with the remainder of the original photon's energy being emitted as a new, lower energy gamma photon with an emission direction different from that of the incident gamma photon. Finally, when these reduced-energy photons have energies where the photoelectric effect dominates (E<100 keV), the remaining energy is transferred in totality to an electron. Compton scattering is thought to be the principal absorption mechanism for gamma rays in the intermediate energy range 100 keV to 1 MeV.

A positron-electron pair is produced in the pair production mechanism (important above 1.022 MeV). The subsequent annihilation of the positron generates γ-rays of 0.511 MeV that may further interact by the first two mechanisms.

The ^{7}Be-emitted X-rays, with 112 eV energy ($2.4 \cdot 10^{16}$ Hz frequency), are situated at the very low limit of the X-ray spectrum. In this case, the only possible ionisation mechanism is the photoelectric effect. We have to take into account also that at this energy, the penetration depth of the photon in the material is very short (~100 nm for polymers).

For the γ - rays emitted by ^{7}Be, the situation is different. The energy of 478 keV indicates that they will loose energy especially by the Compton effect. In this case, the emitted electrons will have a continuous energy distribution between 0 keV and a maximum value given by [117]:

$$E_{\max} = \frac{2 \cdot \frac{(h\nu)^2}{m_e c^2}}{1 + 2 \cdot \frac{h\nu}{m_e c^2}} = 462\ keV \qquad \text{(II.28}$$

with $h\nu = 478\ keV$, the energy of the incoming gamma rays, m_e the electron rest mass and c the speed of light.

The range of the electrons can be calculated using [118]:

$$d(cm) = 0.35 \cdot \frac{E}{\rho} \qquad \text{(II.29}$$

where E is the energy of the electron in MeV and ρ is the density of the target material in g/cm^3. For example, for the maximum energy of the electrons (462 keV), the maximum range in the polypropylene (ρ = 0.9 g/cm^3) will be 1.8 mm.

These electrons, with energies between 0 and 462 keV will interact with the target nuclei (elastic scattering) and with the target electrons (inelastic scattering) [119]. Due to the large difference in the mass of the two colliding particles, the interaction with the target nuclei will induce a very small energy loss, but a strong deviation of the electron. The second type of interaction is the principal mechanism of energy loss (by excitation and ionisation of target atoms), and at the same time, will induce an important deviation of the incident electrons.

An electron can cause ionisation of further molecules, producing more electrons. As a result, a localised chain reaction of ionisation events is set in motion. Coulombic attraction causes the positively charged ions produced to disappear rapidly as electrons recombine with them. This results in the production of highly excited electronic states [41]. In addition, a portion of the interactions of the radiation with the material can result in energy transfer that is insufficient to cause ionisation, but that result directly in an electronically excited electronic state of the molecule.

The excited-state molecules may undergo radiationless decay to the ground state. Heat is produced, which can result in a rise of the temperature of the sample. Depending on the particular molecular structures involved, the excited states may also undergo radiative decay (i.e. phosphorescence or fluorescence), thereby emitting light. Exciting states can also decay by means of chemical reactions via heterolytic bond cleavage, leading to ions, or by homolytic bond cleavage, leading to formation of free radicals. The radiation-induced free-radical chemistry that follows formation of the initial radical pair is analogous to those occurring in the case of ion irradiation of polymers [120,121].

5. References

1. D. Fink, L.T. Chadderton, Ion-solid interaction: status and perspectives, Braz. J. of Phys., 35 (2005) 735.

2. H. Dong, T. Bell, State-of-the-art overview: ion beam surface modification of polymers towards improving tribological properties, Surf. Coat. Technol. 111 (1999) 29.

3. E.H. Lee, Ion beam modifications of polymeric materials – fundamental principles and applications, Nucl. Instr. and Meth. in Phys. Res. B 151 (1999) 29.

4. P. Sigmund, Charge-dependent electronic stopping of swift nonrelativistic heavy ions, Phys. Rev. A 56 (1997) 3781.

5. P. Sigmund, Stopping power in perspective, Nucl. Instr. and Meth. in Phys. Res. B 135 (1998) 1.

6. P. Sigmund, A. Schinner, Binary theory of electronic stopping, Nucl. Instr. and Meth. in Phys. Res. B 195 (2002) 64.

7. L. Glazov, Energy-loss spectra of swift ions, Nucl. Instr. and Meth. in Phys. Res. B 161-163 (2000) 1.

8. L. Leblanc, G.G. Ross, W.E. Wallace, Measuring stopping powers of hydrogen and helium in polystyrene near their maximum values, , Nucl. Instr. and Meth. in Phys. Res. B 95 (1995) 457.

9. D.I. Thwaites, Review of stopping power in organic material, Nucl. Instr. and Meth. in Phys. Res. B 27 (1987) 293.

10. H. Paul, A. Schinner, An empirical approach to the stopping power of solids and gases for ions from $_3$Li to $_{18}$Ar, Nucl. Instr. and Meth. in Phys. Res. B 179 (2001) 299.

H. Paul, A. Schinner, An empirical approach to the stopping power of solids and gases for ions from $_3$Li to $_{18}$Ar – Part II, Nucl. Instr. and Meth. in Phys. Res. B 195 (2002) 166.

11. Y. Miyagawa, H. Nakadate, F. Djurabekova, S. Miyagawa, Dynamic-sasamal: simulation software for high-dose ion implantation, Surf. Coat. Tehnol. 158-159 (2002) 87.

12. www.srim.org.

13. J.F. Ziegler, J.P. Biersack, U. Littmark, The Stopping and Range of Ions in Solids, Pergamon Press, New York, 1985.

14. R. Liguori Neto, N. Added, F.A.S. Coutinho, A new experimental method for precise energy loss measurements, Nucl. Instr. and Meth. in Phys. Res. B 161-163 (2000) 159.

15. W.H. Trzaska, T. Alanko, V. Lyapin, J. Räisänen, A novel method for obtaining continuous stopping power curves, Nucl. Instr. and Meth. in Phys. Res. B 183 (2001) 203.

16. D. Niemann, G. Konac, S. Kalbitzer, Stopping power measurements of ^{1}H, ^{4}He and ^{14}N in Si in the energy range of 0.02-1 MeV/amu, Nucl. Instr. and Meth. in Phys. Res. B 118 (1996) 11.

17. W.K. Chu, P.D. Bourland, K.H. Wang, D. Powers, Range and dE/dx of C,N,O,F and Ne in Be and C from 500 keV to 2 MeV, Phys. Rev. 175 (1968) 342.

18. J. Räisänen, U. Wätjen, A.J.M. Plompen, F. Munnik, Stopping power determination by the transmission technique, Nucl. Instr. and Meth. in Phys. Res. B 118 (1996) 1.

19. L.C. Northcliffe, Energy loss and effective charge of heavy ions in Aluminium, Phys. Rev. 120 (1960) 1744

20. P.E. Schambra, A.M. Rauth, L.C. Northcliffe, Energy loss measurements for heavy ions in Mylar and polyethylene, Phys. Rev. 120 (1960) 1758.

21. D.C. Lorents, E.J. Zimmerman, Stopping of low-energy H^{+} and He^{+} ions in plastics, Phys. Rev. 113 (1959) 1199.

22. H.H. Andersen, J.F. Bak, H. Knudsen, B.R. Nielsen, Stopping power of Al, Cu, Ag, and Au for MeV hydrogen, helium, and lithium ions. Z_1^3 and Z_1^4 proportional deviations from the Bethe formula, Phys. Rev. A 16 (1997) 1929.

23. Y. Zhang, G. Possnert, W.J. Weber, Measurement of electronic stopping power of swift heavy ions using high-resolution time-of-flight spectrometer, Appl. Phys. Lett. 80 (2002) 4662.

24. Y. Zhang, G. Possnert, H.J. Whitlow, Measurements of the mean energy-loss of swift heavy ions in carbon with high precision, Nucl. Instr. and Meth. in Phys. Res. B 183 (2001) 34.

25. Y. Zhang, High-precision measurement of electronic stopping powers for heavy ions using high-resolution time-of-flight spectrometry, Nucl. Instr. and Meth. in Phys. Res. B 196 (2002) 1.

26. G. Konac, Ch. Klatt, S. Kalbitzer, Universal fit formula for electronic stopping of all ions in carbon and silicon, Nucl. Instr. and Meth. in Phys. Res. B 146 (1998) 106.

27. Y. Zhang, G. Possnert, Electronic stopping power of swift heavy ions in carbon, Nucl. Instr. and Meth. in Phys. Res. B 190 (2002) 69.

28. Y. Zhang, W.J. Weber, A. Razpet, G. Possnert, Electronic stopping powers for Be, Ca and Ti in SiC, Nucl. Instr. and Meth. in Phys. Res. B 242 (2006) 82.

29. C.A. Sautter, E.J. Zimmerman, Stopping cross sections of carbon and hydrocarbon solids for low-energy protons and helium ions, Phys. Rev. 140 (1965) 490

30. J. Oddershede, J.R. Sabin, Stopping powers from velocity distributions derived from Compton profiles, Phys. Rev. A 35 (1987) 3283.

31. H. Geissel, H. Weick, C. Scheidenberger, R. Bimbot, D. Gardès, Experimental studies of heavy-ion slowing down in matter, Nucl. Instr. and Meth. in Phys. Res. B 195 (2002) 3.

32. H.F. Mark, D.F. Othmer, C.G. Overberger, G. Seaborg, Encyclopedia of chemical technology, Vol. 13, Wiley, New York, 1981, p. 706.

33. M. Nastasi, J.W. Mayer, J.K. Hirvonen, Ion-Solid Interactions: Fundamentals and Applications, Cambridge Univ. Pr., 2004.

34. J.S. Chen, S.P. Lau, Z. Sun, B.K. Tay, G.Q. Yu, F.Y. Zhu, D.Z. Zhu, H.J. Xu, Structural and mechanical properties of nitrogen ion implanted ultra high molecular weight polyethylene, Surf. Coat. Technol. 138 (2001) 33.

35. Y.Q. Wang, Ion beam analysis of ion-implanted polymer thin films, Nucl. Instr. and Meth. in Phys. Res. B 161-163 (2000) 1027.

36. E.H. Lee, G.R. Rao, L.K. Mansur, LET effect on cross-linking and scission mechanisms of PMMA during irradiation, Rad. Phys. and Chem. 55 (1999) 293.

37. J. Chen, F. Zhu, H. Pan, J. Cao, D. Zhu, H. Xu, Q. Cai, J. Shen, L. Chen, Z. He, Surface modification of ion implanted ultra high molecular weight polyethylene, Nucl. Instr. and Meth. in Phys. Res. B 169 (2000) 26.

38. A. Valenza, A.M. Visco, L. Torrisi, N. Campo, Characterization of ultra-high-molecular-weight polyethylene (UHMWPE) modified by ion implantation, Polymer 45 (2004) 1707.

39. V. Hnatowicz, V. Perina, V. Havranek, V. Vosecek, J. Novotny, J. Vacik, V. Svorcik, V. Rybka, A. Kluge, Degradation of polyimide and polyethyleneterephtalate irradiated with 150 and 200 keV Ar^+ ions, studied by RBS and ERD techniques, Nucl. Instr. and Meth. in Phys. Res. B 161-163 (2000) 1099.

40. W.L. Brown, Ion beam induced chemical changes in molecular solids, Nucl. Instr. and Meth. in Phys. Res. B 37/38 (1989) 270.

41. H.F. Mark, N.M. Bikales, C.G. Overberger, G. Menges, Enciclopedia of polymer science and engineering, Vol. 13, Wiley, New York, 1985, p. 667-707.

42. J. Zekonyte, J. Erichsen, V. Zaporojtchenko, F. Faupel, Mechanisms of argon ion-beam surface modification of polystyrene, Surface Science 532 (2003) 1040.

43. A. Kondyurin, R. Khaybullin, N. Gavrilov, V. Popok, Pulse and continuous ion beam treatment of polyethylene, Vacuum 68 (2003) 341.

44. K. Proskova, V. Svorcik, V. Rybka, V. Hnatowicz, Selected degradation reactions in polyethylene irradiated with Ar^+ and Xe^+ ions, Rad. Phys. Chem. 58 (2000) 153-156

45. D. Fink (Ed.), Fundamentals of Ion-Irradiated Polymers, Springer - Material Science, Berlin , 2004.

46. A. Chapiro, General considerations of the radiation chemistry of polymers, Nucl. Instr. and Meth. in Phys. Res. B 105 (1995) 5.

47. J. San, J. Liu, B. Zhu, Z. Mo, Q. Zhang, C. Dong, Metal-ion implantation effects on nano-hardness and tribological properties of Nylon6, Surf. Coat. Technol. 161 (2002) 1.

48. T. Kobayashi, A. Nakao, M. Iwaki, Wear properties of tungsten-implanted polyimide, Nucl. Instr. and Meth. in Phys. Res. B 206 (2003) 1110.

49. J. Davenas, I. Stevenson, N. Celette, S. Cambon, J.L. Gardette, A. Rivaton, L. Vignoud, Stability of polymers under ionising radiation : The many faces of radiation interactions with polymers, Nucl. Instr. and Meth. in Phys. Res. B 191 (2002) 653.

50. R.J. Rodriguez, J.A. Garcia, R. Sanchez, A. Perez, B. Garrido, J. Morante, Modification of surface mechanical properties of polycarbonate by ion implantation, Surf. Coat. Technol. 158 (2002) 636.

51. J. San, J. Liu, B. Zhu, Z. Liu, C. Dong, Q. Zhang, Tribological properties of ion implanted polyethylene oxide (PPO), Wear 251 (2001) 1504.

52. J. San, B. Zhu, J. Liu, Z. Liu, C. Dong, Q. Zhang, Mechanical properties of ion-implanted polycarbonate, Surf. Coat. Technol. 138 (2001) 242.

53. W. Yuguang, Z. Tonghe, Z. Huixing, Z. Xiaoji, D. Zhiwei, Polymer modification by MEVVA source deposited and ion implantation, Surf. Coat. Technol. 131 (2000) 520.

54. L. Guzman, R. Celva, A. Miotello, E. Voltolini, F. Ferrari, M. Adami, Polymer surface modification by ion implantation and reactive deposition of transparent films, Surf. Coat. Technol. 103-104 (1998) 375.

55. D. Fink, R. Klett, L.T. Chadderton, J. Cardoso, R. Montiel, H. Vazquez, A.A. Karanovich, Carbonaceous clusters in irradiated polymers as revealed by small angle X-ray scattering and ESR, Nucl. Instr. and Meth. in Phys. Res. B 111 (1996) 303.

56. V.N. Ppopok, V.B. Odzhaev, I.P. Kozlov, I.I. Azarko, I.A. Karpovich, D.V. Sviridov, Ion beam effects in polymer films: Structure evolution of the implanted layer, Nucl. Instr. and Meth. in Phys. Res. B 129 (1997) 60.

57. J. Davenas, X.L. Xu, G. Boiteux, D. Sage, Relation between the structure and electronic properties of ion irradiated polymers, Nucl. Instr. and Meth. in Phys. Res. B 39 (1989) 754.

58. C.M. Balik, M.A. Said, High-energy ion implantation of polymers: poly(ethylene terephthalate), J. Polym. Science B 25 (1987) 817.

59. M. Guenther, G. Gerlach, G. Suchaneck, K. Sahre, K.J. Eichhorn, B. Wolf, A. Deineka, L. Jastrabik, Ion-beam induced chemical and structural modification in polymers, Surf. Coat. Technol. 158-159 (2002) 108.

60. D.M. Rück, S. Brunner, K. Tinschert, W.F.X. Frank, Production of buried waveguides in PMMA by high energy ion implantation, Nucl. Instr. and Meth. in Phys. Res. B 106 (1995) 447.

61. K. Sahre, K.J. Eichhorn, F. Simon, D. Pleul, A. Janke, G. Gerlach, Characterization of ion-beam modified polyimide layers, Surf. Coat. Technol. 139 (2001) 257.

62. V. Svorcik, E. Arenholz, V. Rybka, V. Hnatowicz, AFM surface morphology investigation of ion beam modified polyimide, Nucl. Instr. and Meth. in Phys. Res. B 122 (1997) 663.

63. M. Ikeyama, Y. Hayakawa, M. Tazawa, S. Nakao, K. Saitoh, Y. Miyagawa, S. Miyagawa, Changes in surface morphology and optical properties of polymers induced by ion implantation, Thin solid Films 281-282 (1996) 529.

64. L. Calcagno, Ion-chains interactions in polymers, Nucl. Instr. and Meth. in Phys. Res. B 105 (1995) 63.

65. R.J. Composto, Application of ion scattering techniques to characterize polymer surfaces and interfaces, Mat. Sci. Eng. 38 (2002) 107.

66. J.F. Ziegler, RBS/ERD simulation problems : Stopping powers, nuclear reactions and detector resolution, Nucl. Instr. and Meth. in Phys. Res. B 136-138 (1998) 141.

67. N. Added, J.F.D. Chubaci, M. Matsuoka, R.A. Castro, M. Radtke, E. Alonso, R. Liguori Neto, M.A. Rizzuto, M. Tabacniks, R.D. Mansano, Light element analysis using ERDA method with an ionisation chamber, Nucl. Instr. and Meth. in Phys. Res. B 175-177 (2001) 787.

68. F. Schiettekatte, A. Chevarier, N. Chevarier, A. Plantier, G.G. Ross, Quantitative depth profiling of light elements by means of ERD E X B technique, Nucl. Instr. and Meth. in Phys. Res. B 118 (1996) 307.

69. M.Geoghegan, F. Abel, High resolution elastic recoil detection analysis of polystyrene depth profiles using carbon ions, Nucl. Instr. and Meth. in Phys. Res. B 143 (1998) 371.

70. www.lbl.gov/msd/Internal/Facilities/MSD_Ion_Beam.html.

71. G.P. Lamaze, H.H. Chen-Mayer, D.A. Becker, F. Vereda, R.B. Goldner, T. Haas, P. Zerigian, Cold neutron depth profiling of lithium-ion battery materials, J. Power Sources 119-121 (2003) 680.

72. R.G. Wilson, G.E. Lux, C.L. Kirschbaum, Depth profiling and secondary ion mass spectrometry relative sensitivity factors and systematics for polymers/organics, J. Appl. Phys. 73 (1993) 2524.

73. M.S. Janson, M.K. Linnarsson, A. Hallen, B.G. Svensson, Ion implantation range distributions in silicon carbide, J. Appl. Phys. 93 (2003) 8903.

74. I.H. Tan, M. Ueda, R.S. Dallaqua, J.O. Rossi, A.F. Beloto, M.H. Tabacniks, N.R. Demarquette, Y. Inoue, Treatment of polymers by plasma immersion ion implantation for space applications, Surf. Coat. Techn. 186 (2004) 234.

75. F. Faupel, W. Frank, M.P. Macht, H. Mehrer, V. Naundorf, K. Ratzke, H.R. Schober, S.K. Sharma, H. Teichler, Diffusion in metallic glasses and supercooled melts, Rev. Mod. Phys. 75 (2003) 237.

76. R.G. Wilson, Ion implantation ranges and range straggles in organic polymers and comparison with calculations, J. Appl. Phys. 73 (1993) 2215.

77. V. Hnatowicz, J. Kvitek, V. Svorcik, V. Rybka, Long term changes of polypropylene implanted with I^+ ions, Eur. Polym. J. 31 (1995) 449.

78. D. Fink ed., Transport processes in ion-irradiated polymers, Springer-Verlag, Berlin, 2004, p.47-91.

79. D. Fink, M. Behar, J. Kaschny, R. Klett, L.T. Chadderton, V. Hnatowicz, J. Vacik, L. Wang, On the redistribution of $^6Li^+$ ions implanted into polypropylene foils, Appl. Phys. A 62 (1996) 359.

80. D. Fink, Depth distributions of megaelectronvolt ^{14}N implanted into various solids at elevated fluences, Mat. Sci. Eng. 2 (1989) 49.

81. D. Fink, M. Muller, S. Ghosh, V. Hnatowicz, J. Vacik, Tomographic study of the three-dimensional distribution of a high-fluence implant in a polymer, Appl. Phys. A 68 (1999) 429.

82. D. Fink, M. Muller, A. Schmoldt, J.K. Zhou, Implantation of polymers at medium ion fluences: a spatial heterogeneity of radiation damage due to dominant electronic stopping, Nucl. Instr. and Meth. in Phys. Res. B 65 (1992) 432.

83. J. Vacik, V. Hnatowicz, J. Cervena, V. Perina, V. Popok, V. Odzhaev, V. Svorcik, V. Rybka, E. Arenholz, D. Fink, Annealing behaviour of boron atoms implanted into polyethyleneterephtalate, Nucl. Instr. and Meth. in Phys. Res. B 166-167 (2000) 637.

84. M.R.F. Soares, M. Behar, D. Fink, M. Muller, A. Petrov, $^{10}B^{+}$ ion implantation into photoresist, Appl. Phys. A 77 (2003) 891.

85. M.R.F. Soares, L. Amaral, M. Behar, D. Fink, Diffusion of Ag implanted into the AZ1350 photoresist, Nucl. Instr. and Meth. in Phys. Res. B 191 (2002) 690.

86. K.M. Wang, B.R. Shi, J.T. Liu, X.D. Liu, K. J. Yao, Range profiles of Hg^{+}, Hg^{2+}, Hg^{3+} in polymer polyvinylalcohol, J. Appl. Phys. 66 (1989) 4577.

87. R.B. Guimaraes, M. Behar, R.P. Livi, J.P. de Souza, F.C. Zawislak, D. Fink, J.P. Biersack, Mass and energy dependence of implanted ion profiles in the AZ111 photoresist J. Appl. Phys. 60 (1986) 1322.

88. V. Hnatowicz, J. Vacik, J. Cervena, V. Perina, V. Svorcik, V. Rybka, on anomalous depth profiles of atoms implanted into polymers, Nucl. Instr. and Meth. in Phys. Res. B 136-138 (1998) 568.

89. D. Fink, M. Muller, Y. Nakao, K. Hirata, Y. Kobayashi, M. Behar, J.R. Kaschny, J. Vacik, V. Hnatowicz, Ion-induced redistribution of palladium in polymethyl methacrylate, Nucl. Instr. and Meth. in Phys. Res. B 166-167 (2000) 610.

90. J.R. Kaschny, M. Behar, Diffusion study of Kr, Rb and Xe implanted into positive and negative photoresist films, Nucl. Instr. and Meth. in Phys. Res. B 111 (1996) 51.

91. V.N. Popok, V.B. Odzhaev, I.P. Kozlov, I.I. Azarko, I.A. Karpovich, D.V. Sviridov, Ion beam effects in polymer films: Structure evolution of the implanted layer, Nucl. Instr. and Meth. in Phys. Res. B 129 (1997) 60.

92. J. Vacik, V. Hnatowicz, J. Cervena, V. Perina, V. Popok, V. Odzhaev, D. Fink, High fluence boron implantation into polyimide, Nucl. Instr. and Meth. in Phys. Res. B 148 (1999) 1126.

93. M.R.F. Soares, P. Alegaonkar, M. Behar, D. Fink, M. Muller, $^{6}Li^{+}$ ion implantation into polystyrene, Nucl. Instr. and Meth. in Phys. Res. B 218 (2004) 300.

94. V. Svorcik, V. Rybka, O. Jankovkij, V. Hnatowicz, Free volume-limited diffusion in ion-modified polymers, J. Appl. Polym. Sci. 61 (1996) 1097.

95. V. Hnatowicz, J. Vacik, V. Svorcik, V. Rybka, V. Popok, O. Jankovskij, D. Fink, R. Klett, Iodine diffusion and trapping in polyethylene implanted with 150 keV F^{+} and As^{+} ions to different fluences, Nucl. Instr. and Meth. in Phys. Res. B 114 (1996) 81.

96. A. Nakao, M. Iwaki, RBS study of Na-implanted polystyrene at various doses, Appl. Phys. A 71 (2000) 181.

97. V. Hnatowicz, J. Kvitek, V. Svorcik, V. Rybka, V. Popok, Oxygen incorporation in polyethylene implanted with 150 keV Sb^{+} ions, Cz. J. Phys. 44 (1994) 621.

98. P.A. Benioff, Cosmic-ray production rate and mean removal time of Beryllium-7 from the atmosphere, Phys. Rev. 104 (1956) 1122.

99. K.N. Yu, L.Y.L. Lee, Measurements of atmospheric ^{7}Be properties using high-efficiency gamma spectroscopy, Appl. Rad. Isot. 57 (2002) 941.

100. M. Gaelens, M. Cogneau, M. Loiselet, G. Ryckewaert, Post-acceleration of ^{7}Be at the Louvain-la-Neuve radioactive ion beam facility, Nucl. Instr. and Meth. in Phys. Res. B 204 (2003) 48.

101. G. Ryckewaert, J.M. Colson, M. Gaelens, M. Loiselet, N. Postiau, Recent results from the Louvain-la-Neuve RIB-facility, Nucl. Phys. A 701 (2002) 323.

102. L. Campajola, L. Gialanella, K. Brand, A.D'Onofrio, U. Greife, E. Huttel, R. Kubat, G. Oliviero, H. Rebel, V. Roca, C. Rolfs, M. Romano, M. Romoli, S. Schmidt, W.H. Schulte, F. Strieder, F. Terrasi, H.P. Trautvetter, D. Zahnow, Production of an 8.0 MeV ^{7}Be ion beam at the Naples TTT-3 accelerator, Z. Phys. A 356 (1996) 107.

103. C.N. Davis, A.J. Elwyn, B.W. Filippone, S.B. Kaufman, K.E. Rehm, J.P. Schiffer, Branching ratio in the electron-capture decay of ^{7}Be, Phys. Rev. C 28 (1983) 885.

104. F. Ditroi, S. Takács, F. Tárkányi, A. Fenyvesi, J. Bergman, S.J. Heselius, O. Solin, Investigation of the charged particle nuclear reactions on natural boron for

the purposes of the thin layer activation (TLA), Nucl. Instr. and Meth. in Phys. Res. B 103 (1995) 389.

105. R.J. Smith, J.J. Kolata, K. Lamkin, A. Morsad, K. Ashktorab, F.D. Becchetti, J. Brown, J.W. Janecke, W.Z. Liu, D.A. Roberts, Production and use of radioactive ^{7}Be beams, Nucl. Instr. and Meth. in Phys. Res. A 294 (1990) 26.

106. F. Ditroi, I. Mahunka, Thin layer activation of non metallic materials by using nuclear implantation, Nucl. Instr. and Meth. in Phys. Res. B 113 (1996) 415.

107. F. Ditroi, S. Takacs, F. Tarkanyi, I. Mahunka, Study of the ^{nat}C(^{3}He, 2α)^{7}Be and ^{9}Be(^{3}He, αn)^{7}Be nuclear reactions and their application for wear measurements, Nucl. Instr. and Meth. in Phys. Res. B 103 (1995) 412.

108. H.D. Young, R.A. Freedman, University physics, 10th ed., Addison-Wesley, 2000.

109. P. A. Voytas, C. Ternovan, M. Galeazzi, D. McCammon, J. J. Kolata, P. Santi, D. Peterson, V. Guimaraes, F. D. Becchetti, M. Y. Lee, T. W. O'Donnell, D. A. Roberts, S. Shaheen, Direct Measurement of the L/K ratio in 7Be electron capture, Phys. Rev. Lett. 88 (2002) 012501.

110. A. Ray, P. Das, S. K. Saha, S. K. Das, A. Mookerjee, Effect of host medium on the L/K ratio in 7Be electron capture, Phys. Rev. C 66 (2002) 012501.

111. H.D. Young, R.A. Freedman, University physics, 10th ed., Addison-Wesley, 2000.

112. M. Galeazzi, F. Gatti, P. Meunier, S. Vitale, BeO μ calorimeter for the ^{7}Be electron capture decay measurement, Phys. Rev. C 57 (1998) 2017.

113. E.B. Norman, T.E. Chupp, K.T. Lesko, J.L. Osborne, P.J. Grant, G.L. Woodruff, ^{7}Be decay scheme and the solar neutrino problem, Phys. Rev. C 27 (1983) 1728.

114. C.A Huh, Dependence of the decay rate of ^{7}Be on chemical forms, Earth and Planet. Sc. Let. 171 (1999) 325.

115. T. Ohtsuki, H. Yuki, M. Muto, J. Kasagi, K. Ohno, Enhanced Electron-Capture Decay Rate of ^{7}Be Encapsulated in C_{60} Cages, Phys. Rev. Lett., 93 (2004) 112501.

116. A. Ray, P. Das, S. K. Saha, S. K. Das, J. J. Das, N. Madhavan, S. Nath, P. Sugathan, P. V. M. Rao, A. Jhingan, Change of ^{7}Be decay rate in exohedral and endohedral C_{60} fullerene compounds and its implications, Phys. Rev. C 73 (2006) 034323.

117. I.M. Popescu, Fizica, vol. 2, Ed. Did. Pedag., Bucharest, 1983.

118. G. Choppin, J.O. Liljenzin, J. Rydberg, Radiochemistry and nuclear chemistry, 3rd ed., Chalmers Univ., 2002, p187.

119. D. Corbin, Etude de l'oxydation et de la tenue d'élastomères irradiés : conséquences sur l'intégrité des câbles électriques lors d'une situation accidentelle d'un réacteur à eau pressurisée, Doctoral thesis, University of Caen, 2001.

120. J. Guillet, Polymer photophysics and photochemistry, an introduction to the study of photoprocesses in macromolecules, Cambridge University Press, 1985.

121. T. Devanne, Vieillissement radiochimique d'un réseau époxyde, Doctoral thesis, École Nationale Supérieure d'Arts et Métiers Centre de Paris, 2003.

Chapter III
Be^7 ion implantation in polymers - experimental implantation profile

1. Introduction

In Chapter I, the radionuclide techniques used for wear measurement were presented, and we concluded that the only methods suitable for wear measurement of polymer materials may be the radioactive ion implantation methods, namely radioactive recoil implantation and direct ion implantation techniques. We also underlined that the direct implantation of ^{7}Be ions in polymers is the method with the less apparent damaging effects. Therefore, it was decided to concentrate our work on the main features of this technique, when applied to polymers and the first aspect taken into consideration was the determination of the implantation profile, hence, of the calibration curve.

The methods used generally for the determination of the calibration curve, presented in Chapter I, have specific limitations, determined for example by the nature of the sample material or sample thickness. The polishing method, where the residual activity is measured after removing thin layers of material by mechanical or chemical polishing is a method not recommended for soft and ductile materials as polymers [1]. For this type of materials, and when very low activated depths are planned, the best method is the deposition on a substrate of thin films of same composition as the investigated sample with various thicknesses [2]. One drawback of this method is the long time required for the implantation of each film separately. In our case, the $^7Be^{4+}$ beam intensity is quite low, approximately 15 pA = $2.7*10^7$ pps (particle per second), so it was essential to reduce the total implantation time as much as possible. Therefore, we decided to use the stacked foils method, that is, to implant a stack of films made of the copolymer material studied.

Our goal was to verify whether it is possible to predict the experimental implantation profile by means of simulations with the Stopping and Range of Ions in Matter software (SRIM-2003) [3]. This would simplify considerably the wear measurement experiments mainly by offering the possibility to prepare properly the implantation for a given application.

Section 2 presents the implantation of a stack of copolymer films and the activity measurements performed to determine the implantation profile. We decided to use a particular energy distribution of ^{7}Be ions, therefore two energy degraders (gold and aluminium foils) were used to modulate the energy of the ion beam during the implantation. The preparation of the film stack, the alpha spectrometry experiment performed to establish the thickness of the gold and aluminium degrader foils and the method used to determine the experimental energy distribution used during the implantation are also described.

The experimental results are presented and discussed in section 3 in comparison with simulated results. The three subsections include the results of the thickness measurements (section 3.1), the ion energy distributions (section 3.2), experimental stopping power values for ^{7}Be ions in aluminium (section 3.3) and the ion implantation profiles and calibration curves (section 3.4).

2. Experimental section

2.1. Copolymer foils preparation

The material used was the SEPS poly(styrene-*block*-(ethylene-*co*-propylene)-*block*-styrene) tri-block copolymer, with the commercial name Hybrar 7215, already presented in Chapter I, section 4.3. The samples were prepared by spin coating at 2000 rpm from a toluene solution (50 mg/ml). The substrate used was glass (microscope slides cut in squares). Before spin coating, the glass squares were washed with ethanol. The solvent was evaporated at room temperature, under a vacuum, for 24 hours.

Aluminium frames and a support to fix them together were designed and made at the mechanical workshop of the Centre de Recherches du Cyclotron (CRC), Université catholique de Louvain (UCL). The polymer films were floated off on cold distilled water. Each of them was then picked up by an aluminium frame having a 17x15 mm^2 hole at his center.

Fourier Transform Infrared Spectroscopy (FT-IR) of each film was performed in transmission mode using a Nexus 870 FT-IR spectrometer connected to a microscope (Continuum, from Nicolet). Using the interference fringes occurring in the spectra, the thickness of each film was obtained by the procedure described in the Annexe B.

Finally, ten film-supporting frames were mounted on the home-made support (Figure III-1). In the front of the stack, an empty frame was fixed in order to limit the implantation area to the size of the films.

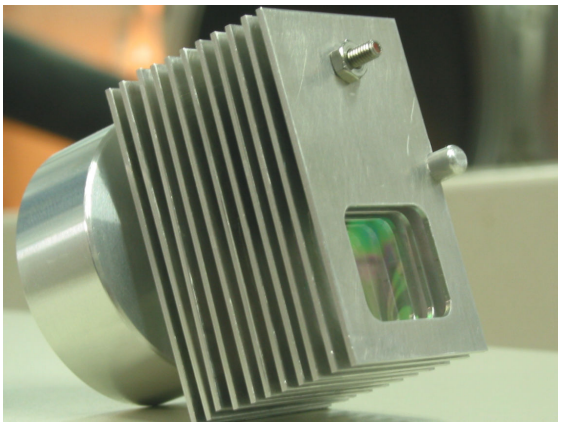

Figure III-1. Photograph of the stacked aluminium frames supporting the polymer foils.

2.2. Energy degraders thickness measurement

The thickness of the gold and aluminium degraders foils was determined by the measurement of the energy loss of alpha particles passing through the foils. A drawing of the setting used for the experiments is presented in Figure III-2.

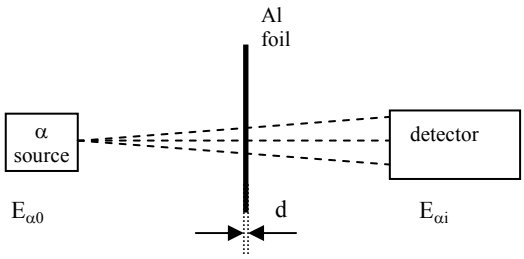

$$\Delta E_{\alpha_i} = E_{\alpha_0} - E_{\alpha_i} \xrightarrow{SRIM} d$$

Figure III-2. Drawing of the experimental setting used for the determination of the aluminium foil thickness

A mixed (Am^{241}, Cm^{244}, Pu^{239}) alpha source, cod AMR.33 from Amersham International, was used. The half-life $T_{1/2}$, the energy of the emitted alpha particles $E_{\alpha 0}$ and emission probability P of the alpha decay of the three radionuclides are presented in Table III-1. The energy was measured using a PIPS (Passivated Implanted Planar Silicon) detector, model number PD100-15-100RM from Canberra. A 2012 model amplifier, and a 2004 model preamplifier from Canberra, were also used.

radionuclide	$T_{1/2}$	$E_{\alpha 0}$ [MeV]	P [%]
Pu^{239}	$2.4 \cdot 10^4$ y	5.155	73.3
		5.143	15.1
		5.105	11.5
Am^{241}	433 d	5.486	85.2
		5.443	12.8
		5.388	1.4
Cm^{244}	18 y	5.805	76.7
		5.763	23.3

Table III-1. Alpha decay characteristics for the three radionuclides used to measure the thickness of the aluminium and gold foils

The detector was calibrated using the three main peaks (5.155 MeV, 5.486 MeV and 5.805 MeV) of the alpha source. For light particles, with Z≤7, the calibration data are well described by a linear relationship [4]. A typical example of calibration curve is presented in. The measurement was completed during two days; therefore, the second day, the calibration was repeated.

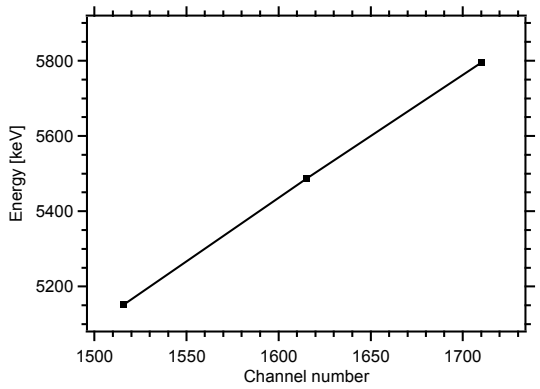

Figure III-3.Calibration curve of the detector used to record the energy of alpha particles.

The two linear detector calibrations were obtained with the following fitting functions:

$$E(ch) = 8.7067(\pm 12.6) + 3.1402(\pm 0.00719) \cdot ch \text{ , } [keV] \qquad (\text{III.1}$$

$$E(ch) = -38.244(\pm 21.3) + 3.1729(\pm 0.0122) \cdot ch \text{ , } [keV] \qquad (\text{III.2}$$

or, more generally:

$$E(ch) = a(\pm u(a)) + b(\pm u(b)) \cdot ch\left(\pm u(ch)\right) \qquad (\text{III.3}$$

where the (one) standard deviations of the fitting coefficients are presented in brackets. The uncertainty in the channel number *u(ch)* is around 2-3 channels and is determined principally by the nonlinearity of the amplifier and preamplifier used for the measurements [5,6].

The alpha source, the aluminium foil and the detector were installed in a sealed chamber, under a vacuum in the configuration presented in Figure III-2. The distribution of the alpha particles was recorded after passing through the aluminium foil in the area used for the implantation experiments. All exiting energy spectra are Gaussian distributions and the channel number corresponding to the distribution maximum was determined by Gaussian fitting. Only the peak corresponding to the 5.155 MeV alpha particles was used for the degrader foils thickness measurement. Figure III-4 presents as example, the distribution of the alpha particles for the first measurement with the aluminium foil.

The corresponding initial and final energies were calculated using the two calibration functions (equations III.1 and III.2). The energy loss ΔE_α in each case was calculated using:

$$\Delta E_{\alpha_i} = (a + b \cdot ch_0) - (a + b \cdot ch_i) = b(ch_0 - ch_i) = b \cdot \Delta ch_i \qquad (\text{III.4}$$

where i=1…6 is the index of the considered experiment, ch_0 = 1639 is the initial position of the considered peak and ch_i is the channel number corresponding to the peak of the distribution number *i*, after passing through the foil. The uncertainty in the energy loss was calculated with:

$$u(\Delta E_i) = \left[b^2 \cdot u^2(ch) + u^2(b) \cdot (\Delta ch_i)^2 \right]^{1/2} \qquad (\text{III.5}$$

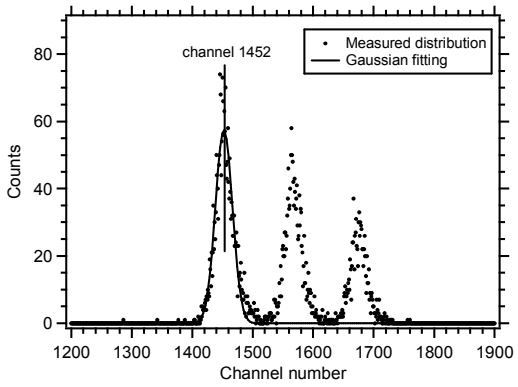

Figure III-4. Measured alpha particle distribution, and Gaussian fitting of one peak after passing through the aluminium foil.

The corresponding aluminium foil thicknesses were calculated using the Stopping and Range of Ions in Matter software (SRIM-2003.26). The same experiment was performed with the gold degrader foil.

2.3. Experimental and simulated energy distributions

Before the implantation, the energy distribution of the Be^7 beam after the two degraders was recorded using the detector and electronic configuration presented in the previous section (2.2.). A drawing of the experimental setting used is presented in Figure III-5a. The description of the ^7Be ion production and acceleration procedure is given in the Annexe A.

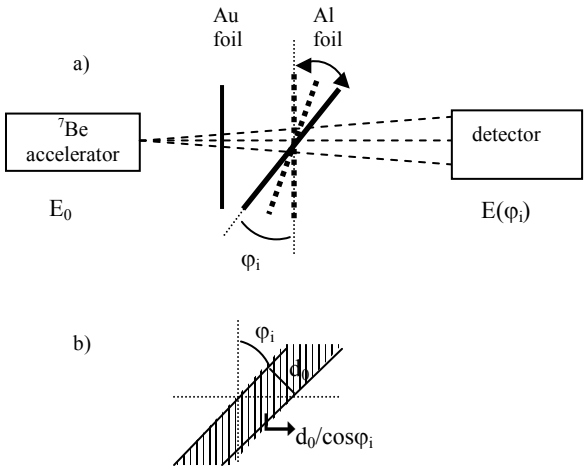

Figure III-5.a) Drawing of the experimental setting used for the determination of the energy distribution of the ^7Be beam after the two energy degraders; b) Drawing illustrating the variation of the real distance traversed by the ions in the aluminium foil with the tilting angle φ

The same calibration procedure was performed and the calibration line obtained was:

$$E(ch) = 128.6(\pm 56.5) + 3.3148(\pm 0.035) \cdot ch \text{ , } [keV] \quad \text{(III.6}$$

The uncertainty in the channel number was considered again to be ~ 2-3 channels.

The ion beam distributions were measured for six different tilting angles φ of the aluminium degrader, including the vertical position. In this way, the real distance traversed by the ions in the aluminium foil $d = d_0 / \cos \varphi$ was varied (Figure III-5b). Using the calibration function, the energy distributions were obtained.

During the measurement, the beam intensity was diminished down to approximately 1 fA, in order to protect the detector and to avoid the apparition of the pile-up effect.

2.4. Ion implantation in SEPS foils

The description of the implantation facility is given in the Annexe A. For this experiment the initial beam energy was 7 MeV and the two energy degraders were used, one fixed in the vertical position and the other one rotated to obtain different beam energies. A drawing of the experimental setup is presented in Figure III-6.

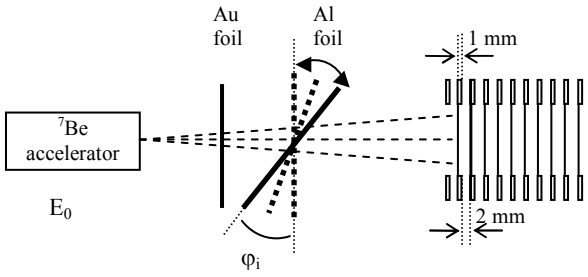

Figure III-6. Drawing of the experimental setting used for the ^{7}Be ion implantation in SEPS foils (approximately 500 nm thick each) supported by aluminium frames

The first degrader, the gold foil, was also used to measure the ion beam intensity during the implantation experiment. The second energy degrader, the aluminium foil, was rotated using an electrical step motor controlled by computer software. The angular position of the foil toward the vertical (angle φ) can be set between 0 and 65.16 degree, with steps of 0.18 degree. Another parameter controlled by the software is the period of time during which the degrader remains in a given position, before passing to the following one.

An energy distribution of the beam was selected for the implantation experiment and 16 different positions of the rotating energy degrader were encoded in the software controlling the motor. After the 16th step, the rotation continued, with the same positions but in reverse order. After each cycle of 32 positions, the foil is brought back to the vertical (the reference position). In this way, the risk to have an accumulation of errors is avoided.

The support with the eleven frames (10 with films and one empty frame) were installed in the implantation chamber. One picture of the experimental configuration is presented in Figure III-7. The implantation was carried out under high vacuum for 4 hours, with a mean beam intensity of 19 pA. After implantation, the samples were left under vacuum for 3 days in the implantation chamber.

2.5. Activity measurements

Five days after the implantation, the activity of the samples (films with frames) was measured with a high sensibility Germanium detector. The measured number of counts for each foil was used to calculate its activity A_k *[Bq]* using the formula:

$$A_k = \frac{n_k}{\varepsilon \cdot p \cdot t_m}, \quad k=1, 2...10 \qquad (\text{III.7}$$

where n_k is the total number of counts accumulated at 478 keV energy during time t, $\varepsilon = 0.00741$ is the global efficiency of the gamma spectroscopy channel at 478 keV, determined with a Europium 152 source, $p = 0.1042$ is the fraction of gamma emission for the ^{7}Be radio-nuclide and $t_m = 1$ hour, the active time of measurement.

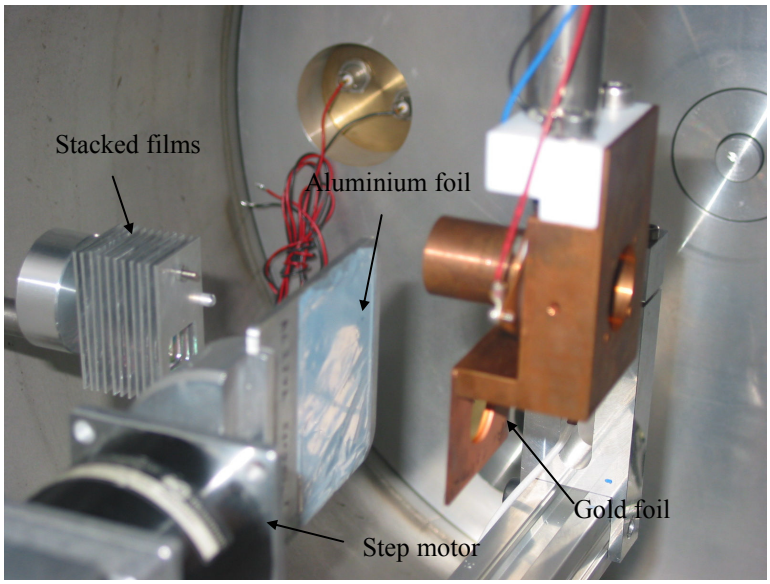

Figure III-7. Experimental configuration in the implantation chamber.

3. Results and discussion

3.1. Energy degraders thickness measurement

Using the SRIM software, the energy distributions of 5.155 MeV α particles passing through aluminium foils of different thicknesses were simulated. All exiting energy spectra are Gaussian distributions and the energy loss ΔE_α in each case was calculated using:

$$\Delta E_\alpha(d) = E_0 - E_{peak}(d) \qquad \text{(III.8}$$

where E_0 =5.155 MeV is the initial energy of alpha particles and $E_{peak}(d)$ is the mean value of the exiting energy distribution, which depends on the foil thickness *d*. The correlation between the thickness of the aluminium foil and the simulated energy loss is presented in Figure III-8. The simulation results were fitted with a linear function:

$$d(\Delta E) = 0.5813(\pm 0.069) + 0.0051(\pm 0.000118)\cdot \Delta E\ ,\ [\mu m] \qquad \text{(III.9}$$

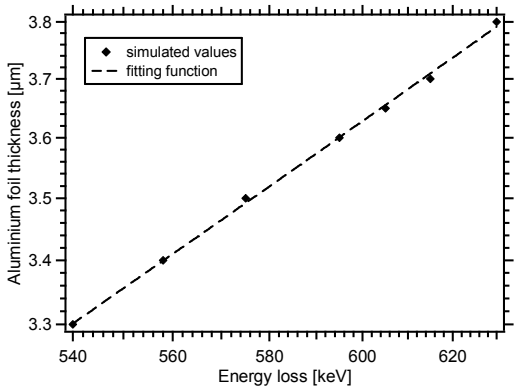

Figure III-8. SRIM predicted correlation between the aluminium foil thickness and the energy loss of alpha particles passing through the foil.

Using the linear fitting function, the aluminium foil thicknesses corresponding to the experimentally determined α particle energy losses were determined for six regions on the foil, in the area used during the implantations. The uncertainties in the thickness determinations were calculated taken into account the uncertainties in the energy loss determined before and the standard deviations for the fitting coefficients in equation III.7. The average value obtained was 3.574±0.106 µm. This represents a precision of about 3%. The summary of the results obtained for the aluminium foil are presented in Table III-2.

No.	ΔE	±u(ΔE)	d	±u(d)
	[keV]	[keV]	[µm]	[µm]
1	586	7.9	3.558	0.106
2	583.8	7.9	3.547	0.105
3	588	8.23	3.569	0.106
4	592	8.24	3.589	0.107
5	590	8.23	3.579	0.107
6	595.2	8.24	3.605	0.107

Table III-2. Summary of the results for the aluminium foil thickness determination

The same method was used for the gold foil (Table III-3) and the average thickness obtained was 1.06±0.107 μm.

No.	ΔE	±u(ΔE)	d	±u(d)
	[keV]	[keV]	[μm]	[μm]
1	482	7.93	1.065	0.11
2	476	7.93	1.055	0.11

Table III-3. Summary of the results for the gold foil thickness determination

3.2. Experimental and simulated energy distributions

The results of the energy measurements (Figure III-5a) for the six different tilting angles of the aluminium foil are presented in Table III-4.

No.	φ	d ± u(d)	±u(d)/d	E ± u(E)	±u(E)/E
	[deg]	[μm]	%	[keV]	%
1	0	3.574 ± 0.106	2.9	2260 ± 61.4	2.7
2	41.4	4.765 ± 0.141	2.9	1380 ± 58.6	4.2
3	46.08	5.152 ± 0.153	2.9	1094 ± 58.0	5.3
4	50.04	5.565 ± 0.165	2.9	807 ± 57.5	7.1
5	53.1	5.952 ± 0.176	2.9	551 ± 57.3	10.4
6	54.54	6.160 ± 0.183	2.9	430 ± 57.3	13.3

Table III-4. The computed distance traversed by the ^{7}Be ions in the aluminium foil tilted by φ from the vertical position and the corresponding measured energy of ^{7}Be ions after passing through the foil.

The uncertainties u(d) in the real distance *d [μm]* traversed by the ions in the aluminium foil were calculated using:

$$u(d) = \frac{u(d_0)}{\cos\varphi} = \frac{0.106}{\cos\varphi} \qquad \text{(III.10}$$

where $u(d_0)$ is the uncertainty in the thickness of the aluminium foil. The uncertainties in the energy determinations were calculated taking into account the uncertainty in the channel number and the standard deviations for the fitting coefficients in equation III.6.

In the SRIM simulation software, it is not possible to simulate exactly our experimental setting; more precisely, it is not possible to simulate the interaction between an ion beam and two target materials, one fixed and one tilted with a given angle. Thus, SRIM simulations were performed, using combinations of a gold target film of 1.06 μm with aluminium target films of thickness equal to the real distance traversed by the ^{7}Be ions in the experimental procedure (Figure III-9a).

The angle of incidence used in the simulation was 0°. The measured energy distribution spectra were compared with simulated energy spectra, for the same number of ions. For illustration, the experimental and simulated energy distributions for the aluminium foil tilted by $\varphi=41.4°$ are presented in Figure III-9b. It can be observed that the peak positions in the two spectra are very similar, but the peak widths and amplitudes differ strongly. The same behaviour was observed for all angles φ. The reason for this behaviour is that, after passing through the gold foil, the divergence of the beam is significantly increased. The diverging beam interacts differently with the tilted aluminium foil than with the simulated vertical thicker foil: path lengths in the material are actually more dispersed than simulated.

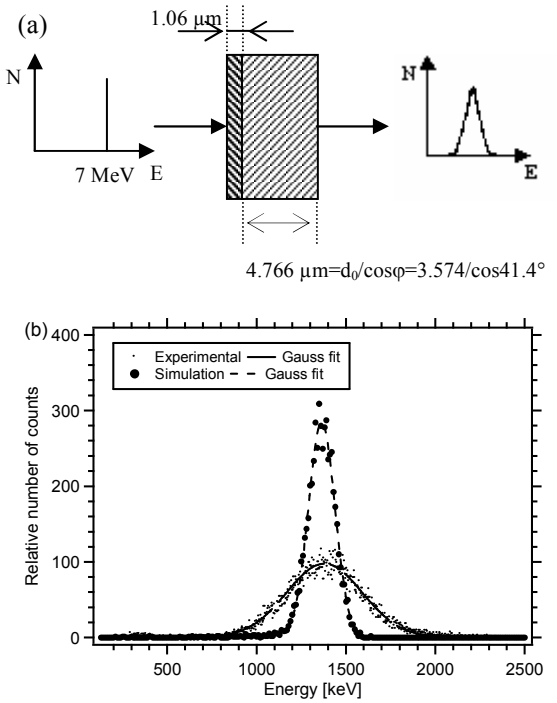

Figure III-9. a) Drawing of the setting used for the simulation corresponding to the experimental case of an aluminium foil tilted by $\varphi=41.4°$; b) Experimental and simulated energy distribution of the ^{7}Be ion beam for $\varphi=41.4°$.

Therefore, we decided to change the configuration used for the simulations. In this setting, the angle of incidence of the beam on the two foils was selected to be equal to the tilting angle of the aluminium foil, and the thickness of the gold foil was modified, in order to have in each situation the same distance traversed by the ion, 1.06 µm. This should be a better approximation than the previous one, since the ongoing beam is of low divergence, making it less sensitive to a tilt of the foil,

whereas the effect of aluminium tilting with respect to beam divergence after the gold foil will be properly taken into account.

Figure III-10a presents a drawing of the configuration used in the simulation, whereas Figure III-10b shows the simulated and experimental beam energy distributions for the same situation as presented before ($\varphi=41.4°$).

It can be observed that the peak positions in the two spectra are not changed, whereas the peak widths and amplitudes are in better agreement with the experimental data. The same behaviour was observed for five simulations. For the simulation with $\varphi=0°$, the peak amplitude (56 counts) was however is much larger than the experimental one (27.7), and the peak width (97.8 keV) was much smaller than the experimental one (211 keV).

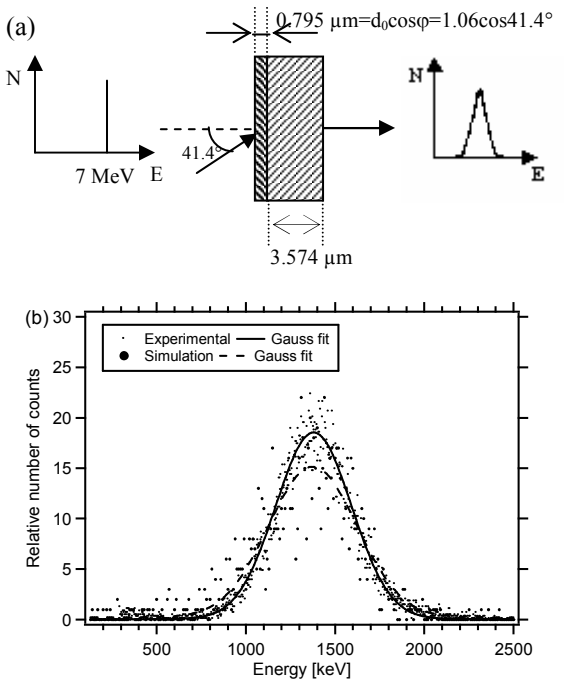

Figure III-10. a) Drawing of the setting used for the simulation corresponding to the experimental case of the aluminium foil tilted with $\varphi=41.4°$; b) Experimental and simulated energy distribution of the ^{7}Be ion beam for $\varphi=41.4°$.

In Figure III-11 are presented the peak positions, widths and normalised amplitudes for the experimental and simulated beam energy distributions as a function of the real thickness traversed by the ^{7}Be ions in the aluminium foil. The error bars indicates the uncertainties in the energy and thickness determinations (see Table

III-4). The values presented for the widths represent the standard deviation of the Gaussian distribution multiplied by the square root of two.

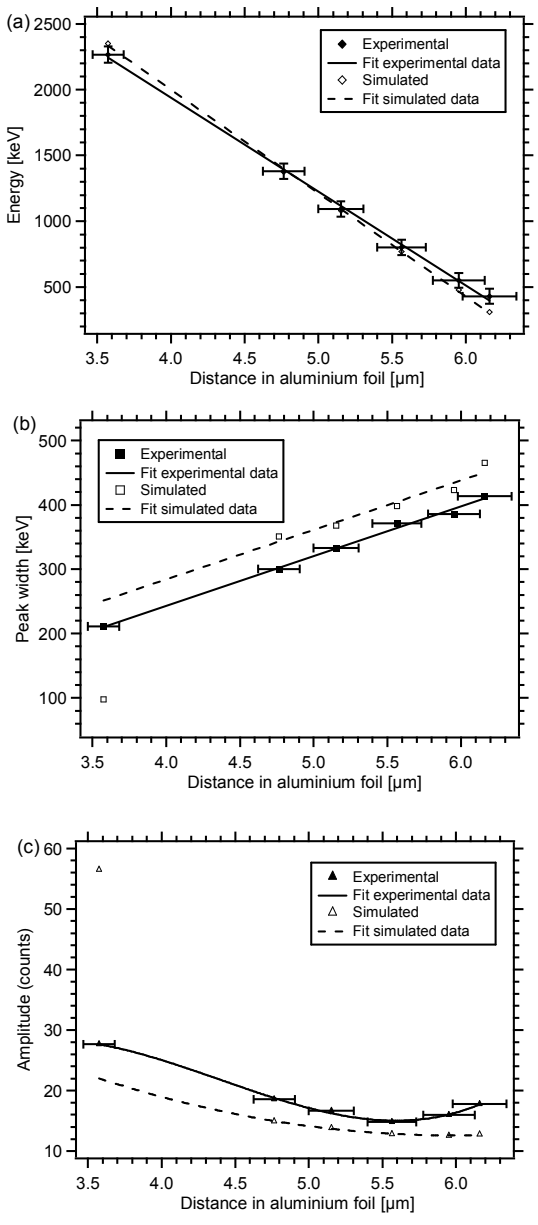

Figure III-11. Simulated and experimental values of the beam energy distribution: a) mean energy, b) width and c) normalised amplitude, as a function of the distance really traversed by the ions in the aluminium foil

The fittings of the simulated amplitudes and widths were made without the outlier point at d= 3.574 μm (φ=0°). The fitting functions were used to obtain the global experimental and simulated energy distributions for the implantation of the ten polymer foils (section 3.3).

The larger values observed for the simulated peak widths and consequently the smaller amplitudes, may be explained by the fact that in the simulations the incidence angles of the beam on the gold foil were different from zero. This induced a larger energy straggling of the beam than the one observed in the experimental situation. We consider that these differences are acceptable, compared to the results obtained with the first simulation setting used.

3.3. Experimental stopping power of ^{7}Be ions in aluminium

As already discussed in Chapter II, section 2.1, the most important parameter in understanding the effects of the electronic and nuclear processes in materials is the energy deposited per unit path length, namely, the stopping power (S).

For Be ions, the literature mentions only a few experimental values for the stopping power in aluminium [7]. In [8], five points were obtained, in the 10-30 keV/nucleon energy interval (that is, between 70 and 210 keV for ^{7}Be ions). For all five points, the experimental values are up to 9% larger than the corresponding ones calculated with SRIM. In [5], the measured stopping power at 1 MeV/nucleon, is approximately 20% larger than the value given by the calculation. Measurements around the stopping maximum (approximately 700 - 5000 keV) were also performed using high-resolution time-of-flight spectrometry [9] and the results are up to 9% smaller than the values given by SRIM.

In the previous section were presented the results of the ^{7}Be ion beam energy measurements after the two energy degraders. These measurements may be used to obtain experimental values of the ^{7}Be ion stopping power in aluminium, in the 550 - 2250 keV energy interval.

In our experiments, the distance traversed by the ions in the aluminium foil was modified by the variation of the tilting angle of the foil. The tilting angles and the corresponding distances were presented in Table III-4. The approach used to calculate the stopping power:

$$S = \frac{dE}{dx} = \left(\frac{dE}{dx}\right)_{elect.} + \left(\frac{dE}{dx}\right)_{nucl.} = S_{elect.} + S_{nucl.} \qquad (\text{III.11}$$

is presented in Figure III-12.

The increase in the distance traversed by the ions in the aluminium foil, due to the tilt angle φ_t, may be considered to arise from the addition of a supplementary

aluminium foil of thickness $\delta_i = \left(\frac{1}{\cos \varphi_i} - 1 \right)$ after the vertical aluminium foil. The measured energies from E_0 to E_4 may thus be considered one after another, as the energy of the ion beam before - and from E_1 to E_5 after - passing through a pseudo aluminium "foil" of thickness given by the difference:

$$\Delta\delta_{i,k} = \delta_k - \delta_i, \quad i = 0...4, \quad k = 1...5, \quad i < k \qquad \text{(III.12}$$

The corresponding energy losses are given by:

$$\Delta E_{i,k} = E_i - E_k, \quad i = 0...4, \quad k = 1...5, \quad i < k \qquad \text{(III.13}$$

and the mean stopping power values were calculated as:

$$S_{i,k}\left(E_{m_{i,k}}\right) = \left(\frac{\Delta E_{i,k}}{\Delta\delta_{i,k}} \right)_{Em_{i,k}} \qquad \text{(III.14}$$

where $Em_{i,k}$ is the mean energy in the energy interval E_k - E_i. Due to the nonlinear dependence of the stopping power with energy,

$$E_{m_{i,k}} \neq \frac{E_k + E_i}{2} \qquad \text{(III.15}$$

Therefore, we determined $Em_{i,k}$ as the energy corresponding to the theoretical (SRIM determined) mean value of the stopping power in the energy interval of interest.

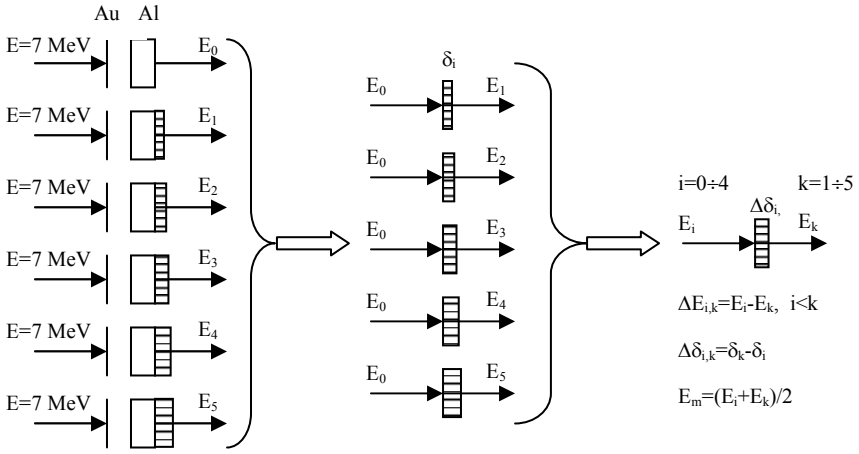

Figure III-12. Schematic representation of the approach used to calculate the stopping power values. (The drawings are not to scale)

In order to reduce the propagation of the uncertainty, each energy loss $\Delta E_{i,k}$ was calculated first in channel numbers and subsequently converted in energy units (keV) using the calibration III.6.

$$\Delta E = 3.3148(\pm 0.035)\cdot \Delta ch \text{ , [keV]} \qquad \text{(III.16}$$

$$u(\Delta ch) = \left[2\cdot u^2(ch)\right]^{1/2} = \sqrt{2}\cdot u(ch) = 3.5 \text{ channels} \qquad \text{(III.17}$$

For the same reason, the corresponding "foil" thicknesses were calculated as:

$$\Delta\delta_{i,k} = \frac{d_0}{\cos\varphi_k} - \frac{d_0}{\cos\varphi_i} = d_0\cdot\left(\frac{1}{\cos\varphi_k} - \frac{1}{\cos\varphi_i}\right) \qquad \text{(III.18}$$

with the uncertainty given by:

$$u(\Delta\delta_{i,k}) = u(d_0)\cdot\left(\frac{1}{\cos\varphi_k} - \frac{1}{\cos\varphi_i}\right) \qquad \text{(III.19}$$

Thus, the uncertainty in the energy loss was estimated by:

$$u(S_{i,k}) = u\left(\frac{\Delta E_{i,k}}{\Delta\delta_{i,k}}\right) = u\left(\frac{3.3148\cdot\Delta ch_{i,k}}{\Delta\delta_{i,k}}\right) =$$
$$= \left[\frac{3.3148^2\cdot 3.54^2 + 0.035^2\cdot(\Delta ch_{i,k})^2}{(\Delta\delta_{i,k})^2} + \frac{3.3148^2\cdot(\Delta ch_{i,k})^2\cdot u^2(\Delta\delta_{i,k})}{(\Delta\delta_{i,k})^4}\right] \qquad \text{(III.20}$$

The results are presented in Figure III-13 together with the theoretical curve obtained with SRIM.

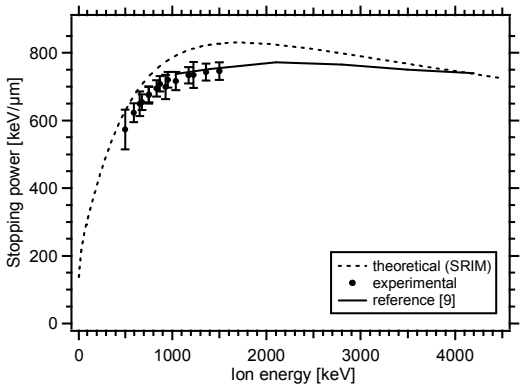

Figure III-13. Stopping power of ^{7}Be ions in aluminium

Our experimental values are up to approximately 9-10% lower than the theoretical ones. As already stated at the beginning of this section, similar results were obtained by means of high-resolution time-of-flight spectrometry [9]. Overall, considering the approximation made in our estimation, the agreement between experimental and theoretical stopping powers is satisfactory.

3.4. Implantation profile of Be^7 in SEPS

The approach for the analysis of the results is presented in Figure III-14.

The experimental and simulated energy distribution corresponding to the aluminium foil rotation parameters were calculated using the fitting functions for the energy peak positions, widths and normalised amplitudes obtained in the precedent section.

From the energy spectra, the corresponding simulated ion distributions in the stacked films were obtained using the SRIM software. The simulated implantation profiles were used to obtain the relative number of ions implanted in each foil, which was compared with the experimentally determined numbers.

At the end, calibration curves were obtained, which will be represented here as the total remaining activity after the "removal" of a polymer layer of thickness equal to the thickness of a polymer foil.

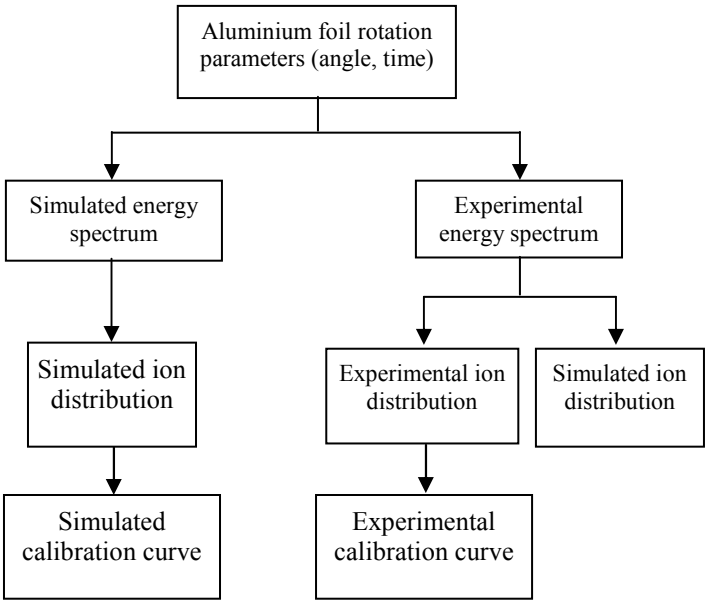

Figure III-14. Diagram of the approach for the analysis of the results of Be^7 implantation in stacked polymer foils.

The calculated experimental and simulated energy distributions of the beam after the aluminium foil are presented in Figure III-15. In order to give an indication on the uncertainty for different energy intervals, the experimentally determined energy values are also presented together with their error bars.

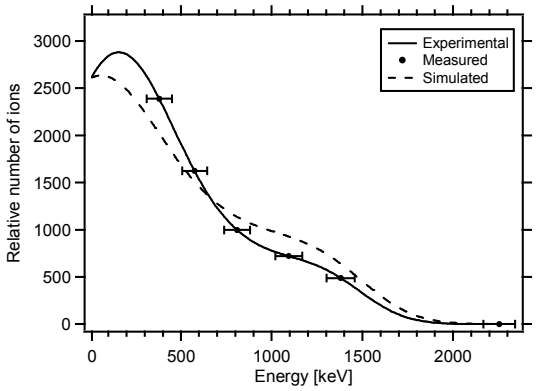

Figure III-15. Experimental and simulated energy distributions after the two energy degrader foils

Implantations of ^{7}Be ions with energies between 10 keV and 2000 keV in polymer target material were simulated with SRIM. The simulations were performed with beams directions perpendicular to the target; therefore, the divergence of the beam after the two energy degraders was not considered. The resulting implantation profiles are Gaussian and the peak position, amplitude and width were determined by fitting. Figure III-16 illustrates the values of the simulated implantation peak position as a function of ion energy and the related fitting function.

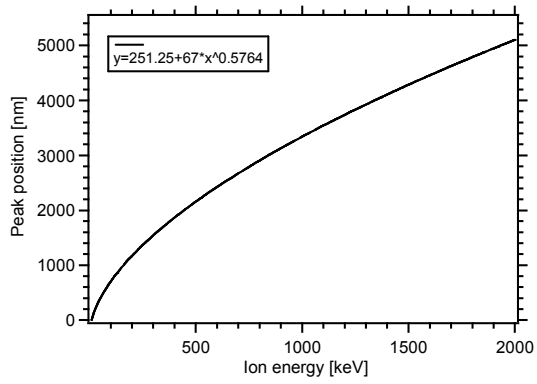

Figure III-16. Simulated implantation peak position as a function of ion energy

The simulated and experimental energy distributions (Figure III-15), together with the fitting functions for the implantation profiles peak position, amplitude and width

as a function of ion energy were used to calculate the corresponding global implantation profiles in the polymer. The results are presented in Figure III-17.

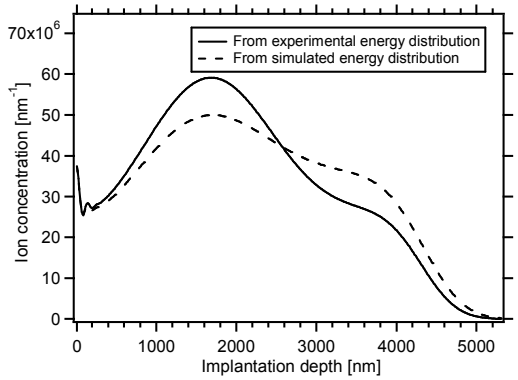

Figure III-17. Calculated implantation profiles

On the other hand, in order to determine the experimental implantation profile, the measured number of counts for each foil was used to calculate its activity A_k using equation III.7.

The number of implanted ions in each foil N_{0k} was then calculated using:

$$N_{0\,k} = \frac{N_k}{\exp(-\lambda \cdot t)} = \frac{A_k}{\lambda \cdot \exp(-\lambda \cdot t)} \qquad \text{(III.21}$$

where N_k is the number of remaining ions $t=5$ *days* after the implantation, and $\lambda = ln2/T_{1/2}$ is the decay constant (with $T_{1/2}=53.3$ *days*, the half-life of ^{7}Be). The results are presented in Table III-5.

The activity of the empty frame (used as an irradiation window) was also measured in the same conditions and the value obtained was 17525 Bq. The relative high level of activity in the aluminium frame, compared to the total activity of the films is a sign of an important beam divergence induced by the two degrader foils.

The uncertainty in the measurement of the copolymer film thicknesses d_k was u(d)=30 nm, independent of the film thickness. The other uncertainties presented in Table III-5 were determined as follows [10]:

$$u(n_k) = \sqrt{n_k} \qquad \text{(III.22}$$

$$u(n_{total}) = \left(\sum_{k=1}^{10} u^2(n_k) \right)^{1/2} \qquad \text{(III.23}$$

Foil[(1)]	d	n[(2)] ±u(n)	A±u(A)	N_0	±u(N_0)	±u(N_0)/ N_0
	[nm]	[counts]	[Bq]			%
A	470	383 ± 19.57	138 ± 7.04	$9.753 \cdot 10^8$	$5.0199 \cdot 10^7$	5.13
B	460	594 ± 24.37	214 ± 8.76	$1.512 \cdot 10^9$	$6.270 \cdot 10^7$	4.13
C	510	1911 ± 43.71	687 ± 15.72	$4.855 \cdot 10^9$	$1.145 \cdot 10^8$	2.35
D	520	7022 ± 83.79	2526 ± 30.14	$1.785 \cdot 10^{10}$	$2.347 \cdot 10^8$	1.31
E	530	10975 ± 104.76	3948 ± 37.68	$2.790 \cdot 10^{10}$	$3.072 \cdot 10^8$	1.09
F	500	11607 ± 107.73	4176 ± 38.75	$2.951 \cdot 10^{10}$	$3.182 \cdot 10^8$	1.07
H	530	11594 ± 107.67	4171 ± 38.73	$2.948 \cdot 10^{10}$	$3.179 \cdot 10^8$	1.07
I	490	9825 ± 99.12	3535 ± 35.65	$2.498 \cdot 10^{10}$	$2.869 \cdot 10^8$	1.14
J	520	8342 ± 91.33	3001 ± 32.85	$2.121 \cdot 10^{10}$	$2.599 \cdot 10^8$	1.22
L	520	5042 ± 71.00	1814 ± 25.54	$1.282 \cdot 10^{10}$	$1.940 \cdot 10^8$	1.50
Total	5050	67295 ± 259.4	24210 ± 93.32	$1.7111 \cdot 10^{11}$	$1.141 \cdot 10^9$	0.66

(1) The order of the foils in the stack was L (in the front of the stack), J, I, H, F, E, D, C, B, A (the last one).
(2) Number of counts in one hour of measurement (γ of 478 keV).

Table III-5. Activity and number of implanted ions for the ten copolymer foils

$$u(A_k) = \frac{u(n_k)}{\varepsilon \cdot p \cdot t_m} \qquad \text{(III.24}$$

$$u(A_{total}) = \left(\sum_{k=1}^{10} u^2(A_k) \right)^{1/2} \qquad \text{(III.25}$$

where k=1…10 and the uncertainties on ε, p and t_m were not considered. On the contrary, the uncertainty of the time after implantation t was considered to be around 10 hours, u(t)=36000 s, the time necessary to perform the counting for all ten foils. Therefore, the uncertainty in the number of ions implanted in each polymer film was calculated as:

$$\begin{aligned} u(N_{0_k}) &= u\left(\frac{A_k}{\lambda \cdot \exp(-\lambda \cdot t)} \right) = \\ &= \left[\frac{u^2(A_k)}{\left[\lambda \cdot \exp(-\lambda \cdot t)\right]^2} + \frac{A_k{}^2 \cdot u^2\left(\lambda \cdot \exp(-\lambda \cdot t)\right)}{\left[\lambda \cdot \exp(-\lambda \cdot t)\right]^4} \right]^{1/2} = \qquad \text{(III.26} \\ &= \left[\frac{u^2(A_k)}{\left[\lambda \cdot \exp(-\lambda \cdot t)\right]^2} + \frac{A_k{}^2 \cdot \lambda^4 \cdot \exp(-2\lambda \cdot t) \cdot u^2(t)}{\left[\lambda \cdot \exp(-\lambda \cdot t)\right]^4} \right]^{1/2} \end{aligned}$$

and for the total number of implanted ions:

$$u(N_{0\,total}) = \left(\sum_{k=1}^{10} u^2 \left(N_{0\,k} \right) \right)^{1/2} \qquad \text{(III.27}$$

From the implantation profile (Figure III-17), calculated from the experimental energy spectra, the simulated number of ions implanted in each polymer foil was calculated as follows:

1. The graph was divided in ten regions, corresponding to the ten polymer films, by taking into account the films thicknesses (Figure III-18).

2. Each resultant segment on the graph was then fitted with a linear function:

$$f_k(x) = a_k + b_k \cdot x \text{ , k=1…10} \qquad \text{(III.28}$$

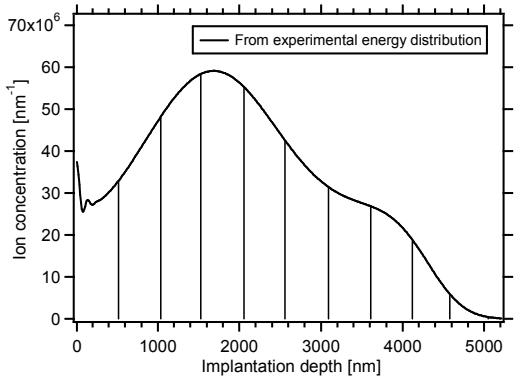

Figure III-18. Simulated implantation profile with the regions corresponding to the ten copolymer films.

3. The area of each region under the graph represents the simulated number of ions implanted in each foil and was calculated using:

4.
$$\begin{aligned} S_k &= \int_{x_{k-1}}^{x_k} (a_k + b_k \cdot x) dx \quad , \quad x_k = \sum_{i=1}^{k} d_i \,,\, x_0 = 0 \\ S_k &= a_k \cdot (x_k - x_{k-1}) + \frac{b_k}{2} \cdot x_k^2 - \frac{b_k}{2} \cdot x_{k-1}^2 = \\ &= a_k \cdot d_k + b_k \cdot d_k \cdot \frac{x_k + x_{k-1}}{2} = \\ &= d_k \cdot \left(a_k + b_k \cdot \frac{x_k + x_{k-1}}{2} \right) \end{aligned} \qquad \text{(III.29}$$

5. The uncertainties in the areas were calculated as:

$$u(S_k) = \left[a_k^2 \cdot u^2(d) + b_k^2 \cdot x_k^2 \cdot u^2(x_k) + b_k^2 \cdot x_{k-1}^2 \cdot u^2(x_{k-1})\right]^{1/2} =$$
$$= \left[a_k^2 \cdot u^2(d) + b_k^2 \cdot x_k^2 \cdot k \cdot u^2(d) + b_k^2 \cdot x_{k-1}^2 \cdot (k-1) \cdot u^2(d)\right]^{1/2} =$$
$$= \left[a_k^2 + k \cdot b_k^2 \cdot x_k^2 + (k-1) \cdot b_k^2 \cdot x_{k-1}^2\right]^{1/2} \cdot u(d) \qquad \text{(III.30}$$

where we took into account that :

$$u^2\left(x_k^2\right) = \sum_{i=1}^{k} u^2(d_i) = k \cdot u^2(d) \qquad \text{(III.31}$$

Figure III-19 presents the experimental and simulated numbers of implanted ions for the ten polymer films.

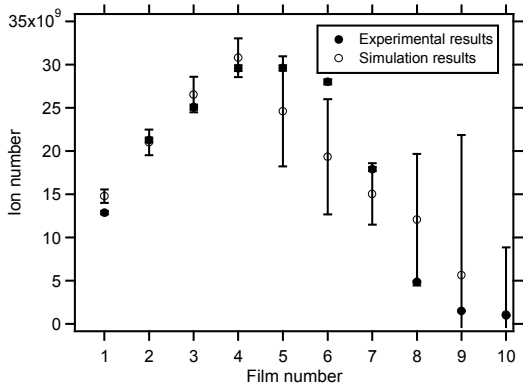

Figure III-19.Experimental and simulated number of implanted ions for each polymer film

Figure III-20 presents the ion concentration depth profiles in the two cases. The vertical error bars include the uncertainties in ion numbers and film thicknesses determination. The horizontal error bars indicates the uncertainty in the position of the middle of each foil.

For the first four foils, the correlation between the simulated and experimental results is good. For the following three foils, the experimental values are larger than the simulated ones and for the foils number 8 and 9, the situation is reversed. The differences may be explained by taking into account the important divergence of the beam after the two energy degraders, observed by measuring the activity of the frame used as implantation window. This implies a wide distribution of the incidence angles on the polymer foils, centred on 0°, while the simulations of the implantation were carried out with angles of incidence equal with 0°. With the increase of the incidence angle, some undesired phenomena occur, that will modify the distribution of the implanted ions in the polymer films.

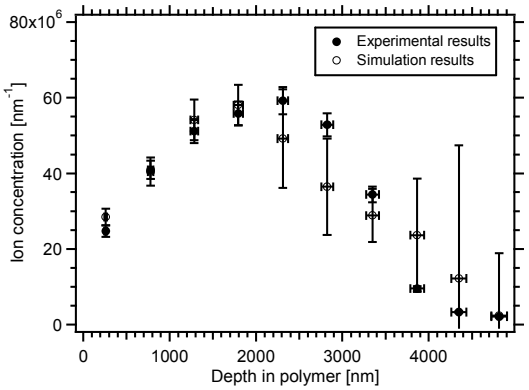

Figure III-20. Ion concentration depth profiles.

First, the projection of the ion path on the horizontal direction decrease, causing the stopping of the ion in polymer foils situated ahead of the planned ones. Namely, as presented in Figure III-21, in the case of two ions, with the same energy E_A=E_B, thus, with approximately the same projected range (see chapter 2, section 2.1.3), the ion with the large implantation angle i_B will be implanted in the fifth film, instead of the planed film number six.

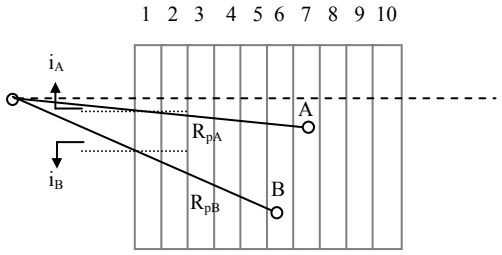

Figure III-21. Schematic presentation of the influence of the incidence angles i_A, i_B on the implantation position for two ions having the same projected range R_{pA}=R_{pB}

Second, the divergence of the beam at the exit of each polymer foil will be larger than the simulated one, and a fraction of ions will be implanted in the aluminium frame sustaining the next foil, instead of going further in the stack. Since we measured the activities of the films together with their frames, this will influence the results.

The second phenomenon is amplified by the fact that the foils are not laying one against the other, but spaced by 3 mm. For the films situated deeper in the stack, these distances add, and the effects are more important.

The calibration curves corresponding to the experimental and the simulated implantations are shown in Figure III-22. The measured values of activities of the polymer films were presented in Table III-5 together with their uncertainties.

To establish the simulated curve in Figure III-22, the simulated activities of each foil were calculated using (eq. III.21):

$$A_{k_{simul}} = \lambda \cdot N_{0k_{simul}} \cdot \exp(-\lambda \cdot t), \text{ k=1…10} \qquad \text{(III.32}$$

and the corresponding uncertainties are:

$$u(A_{k_{simul}}) = \left[\lambda^2 \cdot \left(u^2\left(N_{0k_{simul}}\right) \cdot \exp(-2\lambda \cdot t) + N_{0k_{simul}}^2 \cdot \lambda^2 \cdot \exp(-2\lambda \cdot t) \cdot u^2(t)\right)\right]^{1/2} =$$
$$= \lambda \cdot \exp(-\lambda \cdot t)\left[\left(u^2\left(N_{0k_{simul}}\right) + N_{0k_{simul}}^2 \cdot \lambda^2 \cdot u^2(t)\right)\right]^{1/2} \qquad \text{(III.33}$$

$N_{0ksimul}$ were determined before (equation III.29) as S_k, and the uncertainty in the time after measurement *t=5 days* was considered again to be 10 hours.

For both cases (experimental and simulated), the remaining total activity after the "removal" of the first *j* foils was calculated as:

$$A_{total_j} = \sum_{k=j+1}^{10} A_k \text{ , i=0÷9} \qquad \text{(III.34}$$

and the uncertainties, presented as vertical error bars on the calibration curves, as:

$$u\left(A_{total_j}\right) = \left[\sum_{k=j+1}^{10} u^2\left(A_k\right)\right]^{1/2} \qquad \text{(III.35}$$

The horizontal error bars on the calibration curves indicate the uncertainties in the total thickness of the *j* polymer foils "removed" from the stack.

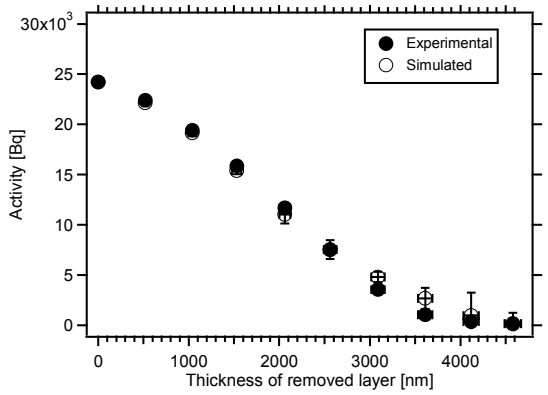

Figure III-22. Calibration curves

The differences between the experimental and simulated calibration curves become significant only after the "removal" of a polymer layer larger than 3000 nm. As was explained before, this is the effect of the implantation of a strongly divergent ion beam. Nevertheless, the agreement is good, which validates SRIM as a valid simulation method for our samples.

4. Conclusions

^{7}Be ions with a particular energy distribution were implanted in a stack of ten copolymer foils. We compared the calculated implantation profile and calibration curve, obtained with the SRIM software, to the experimental ones, determined by means of activity measurements.

The results are encouraging, indicating the possibility to predict the results of the implantation, which would simplify considerably the wear measurement experiments. However, the implantation experiments should be planed carefully, in order to reduce the effects of the beam divergence after the energy degraders. One possibility is to reduce the size of the second degrader foil; in this way, the distance between the second energy degrader and the sample can be reduced, even for large tilting angles. Another possibility is to replace the second energy degrader with several vertical foils, with different thicknesses placed, for example, on a circle.

Experimental values for the stopping power of ^{7}Be ions in aluminium were also determined, by means of transmission techniques, in the 500-1500 keV energy interval. The results are up to 9% smaller than the theoretical ones given by the SRIM software. This is comparable to other experimental determinations performed before.

In our experiment, the as-implanted depth profile was obtained. However, one may expect some redistribution of Be^7 ions after implantation, due to diffusion in the polymer. The stacked foils method avoids this problem, but this possible drawback must be assessed to evaluate properly the potential of radioactive ion implantation for the wear measurement of polymers. This will be done in Chapter V, which will present the study of the redistribution of the implanted ^{7}Be ions in the same target material, the SEPS poly(styrene-*block*-(ethylene-*co*-propylene)-*block*-styrene) tri-block copolymer.

5. References

1. P.M. Racolta, Nuclear methods for tribology, J. Appl. Rad. Isot. 46 (1995) 663.

2. K. Abbas, D. Gilliland, M.F. Stroosnijder, Radioactivity measurements for the thin layer activation technique, Applied Radiation and Isotopes 53 (2002) 179.

3. www.srim.org.

4. Y.Zhang, G. Possnert, H. Whitlow, Measurement of the mean energy-loss of swift heavy ions in carbon with high precision, Nucl. Instr. and Meth. in Phys. Res. B 183 (2001) 34.

5. C. Angulo, T. Delbar, S. Graulich, P. Leleux, Stopping powers of ions at 1 MeV per nucleon, Nucl. Instr. and Meth. in Phys. Res. B 170 (2000) 21.

6. www.canberra.com/literature/935.asp.

7. H. Paul, Stopping power for light ions; Collection of graphs, data and comments, www.uni-linz.ac.at.

8. P. Mertens, T. Krist, Stopping ratios, Nucl. Instr. and Meth. in Phys. Res. 168 (1980) 33.

9. Y. Zhang, High-precision measurement of electronic stopping powers for heavy ions using high-resolution time-of-flight spectrometry, Nucl. Instr. and Meth. in Phys. Res. B 196 (2002) 1.

10. Multi-agency radiological laboratory analytical protocols manual, Vol. III, National Technical Information Service (NTIS), www.ntis.gov.

Chapter IV
Physico-chemical modifications of ion implanted polymer

1. Introduction

In Chapter II, we presented some theoretical considerations regarding physical and chemical modifications induced by ion implantation in polymeric materials. Chapter IV can be considered as a continuation of this subject, from an experimental point of view.

Three ion types were used for the implantation experiments. Selecting ^{7}Be ions was obvious due to their use in the wear measurements based on radioactive ion implantation.

The reason for using ^{7}Li ions (ions with the same mass as ^{7}Be but with a different atomic number) is that the intensity of the ^{7}Be beam is around 10^{7} pps (particles per second); therefore a very long time of implantation is required to implant a larger number of ions in the sample (10^{12}). The intensity of the ^{7}Li beam is higher (~10^{9} pps) and we have the opportunity to compare the effect of the two different type of ions on the samples.

Kr ions were selected because they are heavy ions and therefore, it is expected that they will have a different comportment. The results of the characterisation of the Kr implanted samples can give a basis for comparison to evaluate the polymer modifications induced by the two light ions implantation.

As stated in Chapter II, section 4.3, the X-rays and especially γ rays emitted by ^{7}Be can also induce modifications in the polymer material; therefore, a complementary experiment was also set up were the copolymer samples were exposed only to the radioactive emissions of the ^{7}Be ions.

Section 2 presents details about copolymer films preparation, ion implantation experiments and characterization techniques used. The ten copolymer films on aluminium frames used in the experiment for establishing the experimental implantation profile (see Chapter III) were also checked for physico-chemical modifications.

The results of the characterisations (optical microscopy, AFM, FT-IR,XPS) are presented and discussed in section 3, separately for the two light ions (section 3.1) and Kr ions (section 3.2).

2. Experimental section

2.1. Copolymer films preparation

Two materials were used, the SEPS poly(styrene-*block*-(ethylene-*co*-propylene)-*block*-styrene) tri-block copolymer, with the commercial name Hybrar 7215, already presented in Chapter I, section 4.3 and a copolymer containing unsaturated bonds SIS poly(styrene-*block*-isoprene-*block*-styrene) tri-block copolymer. The styrene content in the SIS copolymer (~18%) is comparable with the one of SEPS (~13%).

The samples were prepared by spin coating from a toluene solution on a Si substrate at 2000 rpm. The concentration used was 150 mg/ml and the thickness of the obtained film was ~3 μm for the SEPS and ~3.5 μm for the SIS samples as determined by ellipsometry. After spin coating the samples were annealed in a vacuum at 140°C for 24 hours. The annealing in a vacuum was necessary so as to prevent the oxidation of the SIS samples.

The preparation of the ten SEPS copolymer foils on aluminium frames was presented in Chapter III, section 2.1.

2.2. Ion implantations

2.2.1. ^{7}Be and ^{7}Li ion implantation

The $^{7}Be^{4+}$ and $^{7}Li^{3+}$ implantations were performed in the implantation facility of the Centre de Recherches du Cyclotron (CRC), Université catholique de Louvain (UCL) and a description of the implantation facility can be found in the Annexe A. The initial beam energy was 7 MeV and energy degraders (thin metallic foils) were used, in order to decrease the energy of the ions to values at which the ions are not able anymore to pass through the samples, but they remain implanted in the samples.

Before the implantation, the distribution of the ^{7}Li and ^{7}Be beam after the degraders was recorded using the detector and electronic configuration presented in Chapter III, section 2.2. In that section, a description of the method used for the detector calibration can also be found.

All exiting energy spectra are Gaussian distributions and the energy corresponding to the distribution maximum was determined by Gaussian fitting. A value of 230 keV was obtained in the case of ^{7}Li ions and 350 keV for ^{7}Be ions. The corresponding implantation profiles in the two materials were simulated using Stopping and Range of Ions in Matter - SRIM software [1]. For all cases, the obtained position of the peak of the implantation profile (Gaussian distributions) was around 2 μm in depth.

During the implantations the beam intensity was ~$3 \cdot 10^9$ pps (particle per second, ~1.6 nA) for the $^7Li^{3+}$ beam and ~$4 \cdot 10^7$ pps (~24 pA) for the $^7Be^{4+}$ beam. The implanted area was 0.5 cm^2 and it was delimited by using thick aluminium masks. The details relating to the implanted samples are presented in Table IV-1.

Sample name	Copolymer	Implanted ions	Dose (ions/sample)
Be-SEPS-l	SEPS	^7Be	$3.22 \cdot 10^{11}$
Be-SEPS-h	SEPS	^7Be	$5.9 \cdot 10^{11}$
Li-SEPS-h	SEPS	^7Li	10^{13}
Li-SEPS-l	SEPS	^7Li	10^{12}
Li-SIS-h	SIS	^7Li	10^{13}
Li-SIS-l	SIS	^7Li	10^{12}

Table IV-1. Description of the ^7Be and ^7Li ions implanted samples

The total number of implanted ions/sample was determined by means of radioactivity measurements for the ^7Be-implanted samples. For the ^7Li-implanted samples, the number of implanted ions was calculated by taking into account the implantation time and the beam current.

The ^7Be ion implantation of the ten SEPS copolymer foils on aluminium frames was already described in section 2.4 of Chapter III, were the stacked foil experiment is presented. The details about the ten films (thickness, activity, number of implanted ions) can also be found in section 3.4 of the same chapter.

2.2.2. Kr ion implantation

The Kr ion implantation was carried out at the Laboratoire d'Analyse par Réaction Nucléaire (LARN), Namur, Belgium. Two series were completed, on 29 March 2004 and on 10 May 2004. The ion beam consisted in natural Krypton (Kr^{84} 57 %, Kr^{86} 17 %, Kr^{83} 11 % and Kr^{82} 11 %). The energy used was 100 keV with a beam current of 5μA. The implanted area was 0.785 cm^2. The parameters of the implanted samples used in the study of the physico-chemical modifications are presented in Table IV-2. The number of implanted ions was calculated by taking into account the implantation time and the beam current.

Sample name	Dose (ions/cm^2)	Conditions after implantation
0N13	$3.3 \cdot 10^{13}$	Freezer (-18°C)
0N14	$1 \cdot 10^{14}$	Freezer (-18°C)
0N15	$1 \cdot 10^{15}$	Freezer (-18°C)
1N13	$3.6 \cdot 10^{13}$	Normal
1N14	$1 \cdot 10^{14}$	Normal
1N15	$1 \cdot 10^{15}$	Normal

Table IV-2. Description of the Kr ions implanted samples

2.3. Exposure to the radioactive emission

A ^{7}Be containing source, with approximately the same activity as the total activity implanted in the ten stacked foils was used (50 kBq). The source was put in an open recipient with the walls thick enough to stop the X-rays but not enough to stop the γ rays.

The polymer samples (films on silicon wafers) were placed as follows: one over the recipient (sample1) and the other one was placed laterally (sample 2) (Figure IV-1). In this way, sample 1 was exposed to the γ and X-rays and sample 2 was exposed only to the γ rays.

We kept the sample under vacuum in the presence of the ^{7}Be source for three days, because after the implantation of the stacked foils, the samples were kept in the implantation chamber for three days. In this way, the results of the two experiments can be compared.

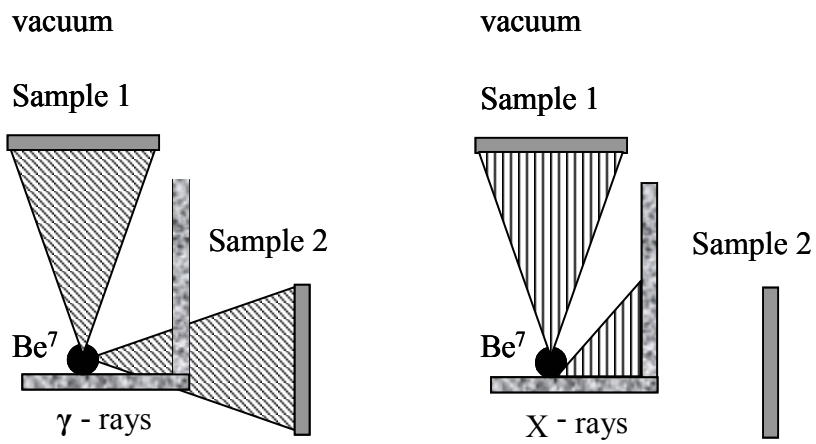

Figure IV-1. Experimental set-up for the exposure to the radioactive emissions.

2.4. Characterisation techniques

2.4.1. Optical microscopy

The surface morphology of the samples was observed using an Olympus AX 70 optical microscope and the images were taken with a Olympus, Camedia C-3040 ZOOM camera.

2.4.2. Atomic Force Microscopy

We studied the topography and structure of the samples by Atomic Force Microscopy in tapping-mode (TM-AFM), when the tip makes contact with the sample only for a short duration in each oscillation cycle. This method results in lower lateral forces compared to the conventional contact mode in which the tip slides across the surface, so the damages to the soft surface can be eliminated [2,3]. The images were recorded in air with an Autoprobe CP from Park Scientific Instruments (Sunnyvale, CA) using a 5 μm and a 100-μm scanner. A highly n^+ doped monolithic silicon AFM tip, Pointprobe NCL-100 was used. The tip apex radius of curvature is less than 7 nm and a cantilever has a force constant of 48 N/m (nominal value).

2.4.3. Fourier Transform Infrared Spectroscopy

We used a Nexus 870 FT-IR spectrometer connected with a microscope (Continuμm, from Nicolet). For the copolymer films on silicon substrate, all spectra were taken in reflection mode, and the results are presented in % Reflectance. For the SEPS copolymer foils on aluminium frames, the spectra were taken in transmission mode, and the results are presented in % Transmittance. Different 100 x 100 μm size areas of the samples were analysed, with a resolution of 8 cm^{-1}, with Happ-Genzel apodisation and Mertz phase correction. The spectrum was recorded in the region 4000-650 cm^{-1} with a MCT/A detector.

An example of resulted spectra is presented in Figure IV-2. It is evident that there is an interference phenomenon due to the planarity and parallelism of the film interfaces. The same behaviour was observed for all samples, over the entire surfaces.

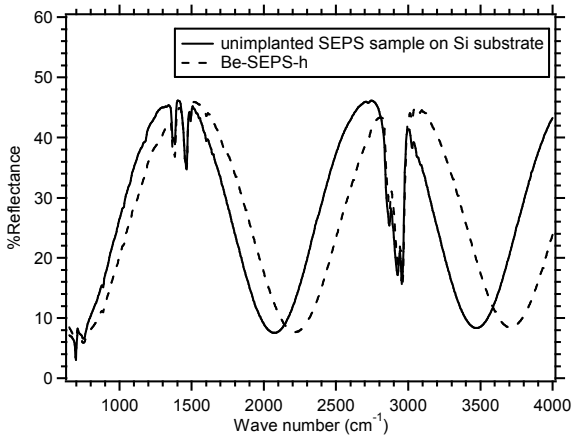

Figure IV-2. Infrared spectra with interference fringes for unimplanted SEPS sample and sample Be-SEPS-h

The presence of the interference fringes obstructs the interpretation of the spectra. We had to find a solution to remove the fringes. A procedure was written in order to simulate the interference phenomena, without the absorption peaks. The procedure was based on the theory of reflection and transmission for a thin film on top of a thick substrate system and it is presented in Annex B.

The corrected spectra allowed distinguishing the peaks (in the limits of the resolution). We were able to observe the apparition of new peaks and the vanishing of some previously existing ones. However, it was not possible to perform a quantitative analysis of the spectra, so we had to limit our interpretation only to a qualitative investigation.

The presence of the interference phenomenon allowed following the evolution of the refractive indexes of the polymer. The amplitude of fringes is proportional to the real part n of the refractive index while their period (the distance between two maximums) is proportional to optical path $n \cdot d$, where d is the thickness of the film, when the angle of incidence is kept constant [4].

2.4.4. X-ray Photoelectron Spectroscopy

XPS spectra were collected on an SSX-100/206 spectrometer (Surface Science Instruments) using monochromatic Al Ka X-rays (1486.6 eV). The spectra were referenced to C(1s) at 284.8 eV. All the spectra were recorded at a take-off angle of 35° (angle between the plane of the surface sample and the entrance lens of the analyser) with a 150 eV pass-energy.

3. Results and discussion

3.1. ^{7}Be and ^{7}Li ions – implantation and radioactive emission

3.1.1. Optical microscopy

No modification of the surface of implanted samples was detectable.

3.1.2. Atomic force microscopy

The morphology of SEPS consisting of discrete cylindrical PS microdomains in the rubbery EP matrix can be observed in Figure IV-3. This structure is explained by the incompatibility between the two phases forced to coexist with each other (see also Chapter I, section 4.3)

The roughness of the surface exposed to the ion beam is almost the same (between 4 and 4.4 Å) and it was measured on the 1 μm^2 size area. A power spectral analysis of the images failed to indicate any measurable change in the morphology.

Comparing the results obtained with AFM, we can conclude that no modification in the material surface topography or surface structure has occurred due to the ^{7}Be or ^{7}Li ion implantation.

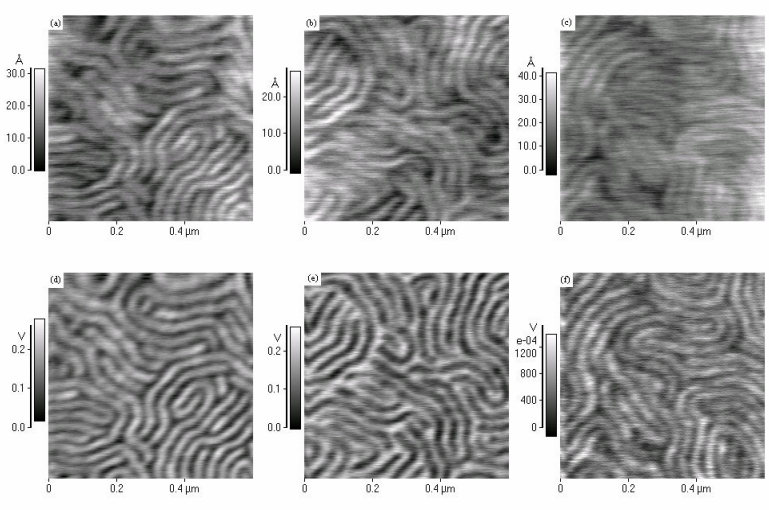

Figure IV-3. AFM topographic images of the SEPS samples: (a) unimplanted, (b) Be-SEPS-h, (c) Li-SEPS-h and corresponding AFM phase images of the same SEPS samples: (d) unimplanted, (e) Be-SEPS-h, (f) Li-SEPS-h

3.1.3. Fourier Transform Infrared Spectroscopy

Polymer films on silicon substrate

In the case of ^{7}Be implanted samples (Figure IV-2) the amplitude of the interference fringes was constant, which indicates that the polymer refractive index was not modified by the implantation. The period showed a small variation, given by the differences in thickness from sample to sample. The same behaviour was observed in the case of ^{7}Li ions implanted SEPS and SIS samples.

The corrected spectra for ^{7}Be implanted SEPS samples in the region 1800-650 cm^{-1} are presented in Figure IV-4. A small oxidation of the pristine SEPS sample is visible at 1712 cm^{-1} (C=O str.) and the presence of aliphatic unsaturated bonds is noticed at 1643 and 840 cm^{-1}.

After implantation new bands appeared, in each case, even for the regions not exposed directly to the ^{7}Be beam: 1754-1693 cm^{-1} (C=O str.), 1319-1218 cm^{-1} (C-O-

C asym. str.) and 1145-1103 cm^{-1} (C-O-C sym. str.) [5,6]. We can presume that a small amount of carboxylic acids, esters and ketones was formed.

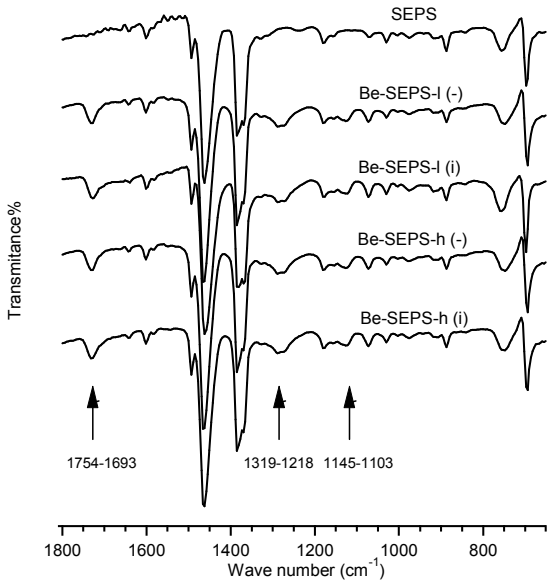

Figure IV-4. Corrected spectra for ^{7}Be implanted samples. In the parentheses after the name of the sample, the area is indicated (i)-implanted area, (-)-unimplanted area

The same modifications were observed on the ^{7}Li-implanted SEPS, but only for the dose of 10^{13} ions/sample and only in the irradiated area.

In the case of SIS samples, the samples were already oxidised before irradiation, due to their sensitivity to atmospheric oxygen. Therefore, we were not able to detect new bands, with the exception of a small one centred on 1727 cm^{-1} (C=O str.), probably ketones.

Stacked foils

The spectra were normalised on the peak at 1462 cm^{-1} and are presented in Figure IV-5.

From Figure IV-5 is evident that new peaks appear in the infrared spectra of the irradiated sample. The presence of the peaks at 1728 cm^{-1} (C=O), 1273 cm^{-1} (C-O-C) and 1122 cm^{-1} (C-O-C) indicate the formation of esters. The peak intensity is the same for all samples, independently of the position in the stack. The FT-IR analysis was repeated after one month and the results were the same.

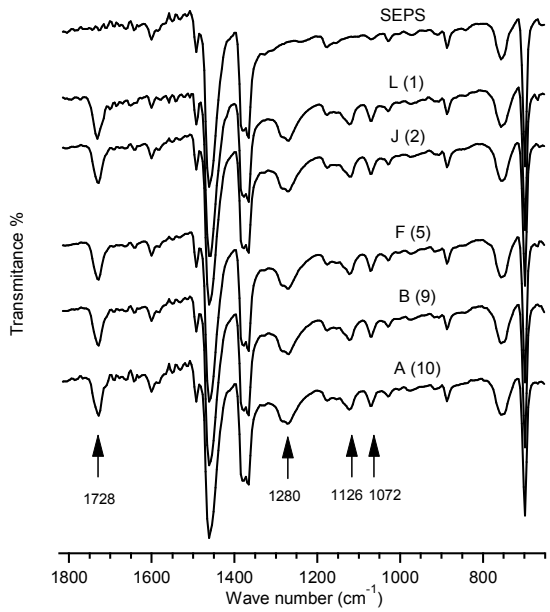

Figure IV-5. FT-IR spectra of one unimplanted (reference) and five implanted foils of SEPS stacked in the beam. Beside the foil name, the position in the foil stack is given, 1 being the foil closer to the source.

It is well known that the chemical modifications (oxidation, bond breaking, cross-linking etc.) are depending on the energy deposited per unit mass, namely with the dose absorbed. We calculated the relative dose absorbed by each foil using the definition of the dose absorbed:

$$D = \frac{(\Delta E)_{abs}}{\Delta m} = \frac{N \cdot \Delta E}{A \cdot \Delta x \cdot \rho} = \varphi \cdot \frac{\Delta E}{\rho \cdot \Delta x}$$
$$with: \quad (\Delta E)_{abs} = N \cdot \Delta E \qquad \text{(IV.1}$$
$$\Delta m = A \cdot \Delta x \cdot \rho$$

where $(\Delta E)_{abs}$ is the total energy absorbed, Δm is the mass of the material absorbing the energy $(\Delta E)_{abs}$, N is the total number of ions, ΔE is energy loss per ion, A is the surface of the material irradiated by the ions, Δx is the thickness of the sample, φ is the fluence and ρ is the density of the material.

$$\frac{\Delta E}{\rho \cdot \Delta x} \cong \frac{1}{\rho} \cdot \frac{dE}{dx} \qquad \text{(IV.2}$$

is the mass stopping power of the material. In our case, we used a distribution of energies of the beam after the two energy degraders so we have to take into account that the stopping power depends on the energy of the incoming ion. Moreover, in the

energy range used we have to consider both effects: the electronic and the nuclear stopping.

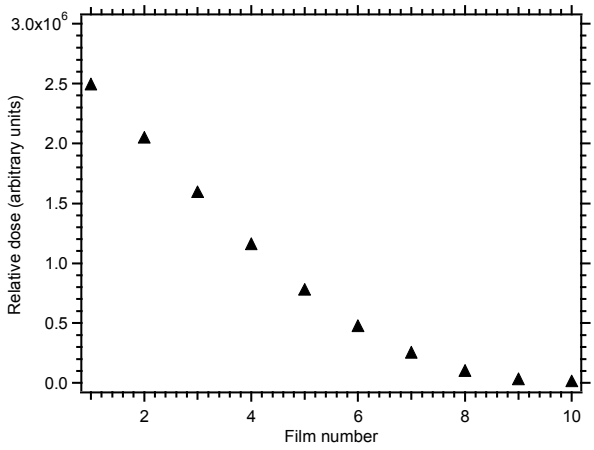

Figure IV-6. The relative dose deposited in each copolymer film

The relative dose deposited in each copolymer foil is presented in Figure IV-6. It is proportional to the fluence and to the stopping power:

$$D_k \sim \varphi_k \cdot \left(\frac{dE}{dx}\right)_{E_k}, \qquad k=1, 2\ldots10 \qquad \text{(IV.3}$$

where $E_{i,k}$ is the ion energy at the entrance of the film number k and φ_{ik} is the corresponding fluence. The stopping power used for the calculation of the dose is the total stopping power, the sum of the electrical and nuclear stopping power of the ions in the copolymer. In our calculation, we neglected the divergence of the beam, which induces small modifications in the fluence.

From Figure IV-6 it is visible that the relative energy doses received by each film due to ion irradiation are different. However, the FT-IR spectra of each foil are identical after implantation (Figure IV-5). A similar phenomenon was observed in the FT-IR analysis of the ^{7}Be ions implanted polymer films on silicon substrate (Figure IV-4), where the same oxidation peaks were observed for different doses, and even in the irradiated and unimplanted regions of the samples. For the ^{7}Li ion implanted polymer samples on silicon substrate, no modification in the unimplanted areas was observed.

Exposure to the radioactive emissions

To check whether the X-rays and γ rays emitted by the radioactive decay of ^{7}Be ions could be detrimental to the materials, films of SEPS on Si substrate were exposed to such rays. The obtained spectra (Figure IV-7) that the same chemical modifications

as described above were produced in both samples, namely, the apparition of oxidation products (carbonyl and C-O-C groups).

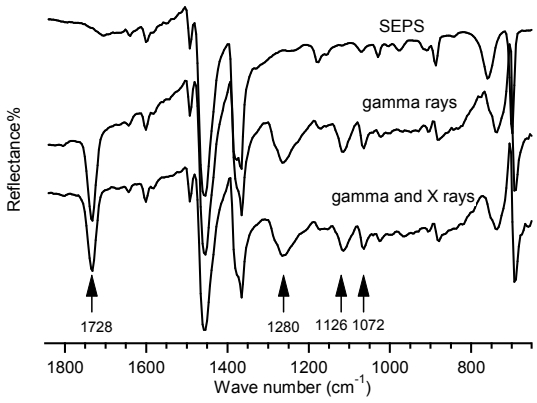

Figure IV-7. FT-IR spectra of one unexposed (reference) sample and the two samples exposed to the γ and X-rays.

Conclusions after FT-IR

We can see from the obtained spectra (Figure IV-7 and Figure IV-5) that the chemical modifications produced by the action of the radioactive emissions only are identical to the ones observed for the ten films implanted by ^{7}Be. Therefore, we can conclude that the oxidation of the ten polymer foils was induced by the γ rays emitted by the implanted ions and not by the ion implantation.

This conclusion is also supported by the results of the characterisations of ^{7}Li implanted samples. As already mentioned, modifications were detected only in the samples implanted with the highest dose, 10^{13} ions/sample and only in the irradiated area.

This can also explain the similar oxidation observed previously in implanted and unimplanted regions of ^{7}Be implanted samples (Figure IV-4) and provides a reason to justify that the 10 films are oxidized similarly, despite their ^{7}Be doses are quite different (Figure IV-6).

The possibility that the radioactive emissions are inducing physico-chemical modifications in polymer materials was already suggested by the review of the literature on the interaction between electromagnetic radiation and matter, presented in Chapter I, section 4.3.

The conclusion formulated at that time was that the gamma rays resulting from the radioactive decay of ^{7}Be via electron capture to the 478 keV state of ^{7}Li are able to pass through all the foils and will lose energy by Compton effect [7,8]. The resulting Compton electrons will induce excitation and ionisation of the target atoms. The

superposition of all this effects will have as result the formation of radicals in the polymer [9,10]; radicals that will interact will the atmospheric oxygen diffusing in the sample [11,12].

The ^{7}Be-emitted X-rays, with 112 eV energy ($2.4 \cdot 10^{16}$ Hz frequency), are situated at the very low limit of the X-ray spectrum; therefore, the only possible ionisation mechanism is the photoelectric effect. At this energy, the penetration depth of the photon in the material is very short (~100 nm for polymers). They will also play a role in degradation, but our experiments cannot determine to which extent, since the volume of sample irradiated by X-rays is very small when using an external source as done here.

3.1.4. X-ray Photoelectron Spectroscopy

In the air, ion implanted polymers undergo spontaneous oxidation, and the oxygen penetrating into implanted layer is fixed presumably in the form of carbonyl groups. Investigation of the oxygen distribution in the polymer target provides significant information on the structure of the implanted layer since the trapped oxygen decorates the regions of high concentration of dangling carbon bonds produced in the course of implantation. We checked the oxygen content of the Li implanted SEPS sample (10^{12} ions/sample) and we compared it with the pristine SEPS using X-ray photoelectron spectroscopy (Figure IV-8).

From the XPS spectra of the unimplanted sample, we can observe the oxygen is already present due to contamination or partial surface oxidation. In the implanted sample, the oxygen content is more or less the same (a little bit smaller) so the implantation did not induce significant oxidation in the first 100 Å of the sample (which is the depth probed by XPS).

The same results were obtained for all SEPS and SIS copolymer samples, without regard on the implanted fluences, or implanted ion (^{7}Be or Li). The conclusion is that the surface of the samples is initially so oxidised or contaminated, that the change due to implantation cannot be detected by XPS. By contrast, FT-IR, which probes a larger volume, successfully revealed the oxidation of the whole sample, following implantation.

3.2. Kr ion implantation

One reason for the implantation of Kr was that they are heavy ions and therefore, it is expected that they will have a different effect on the copolymer material compared to ^{7}Be and ^{7}Li ions. The results of the characterisation of the Kr implanted samples can give a basis for comparison to evaluate the polymer modifications induced by the two light ions implantation.

Another reason was that the bibliographic research on main aspects of ion implantation in polymers indicated, as presented in Chapter II, section 3.2, that

heavy ions redistribute very slowly at room temperature under low fluence implantation [13-15].

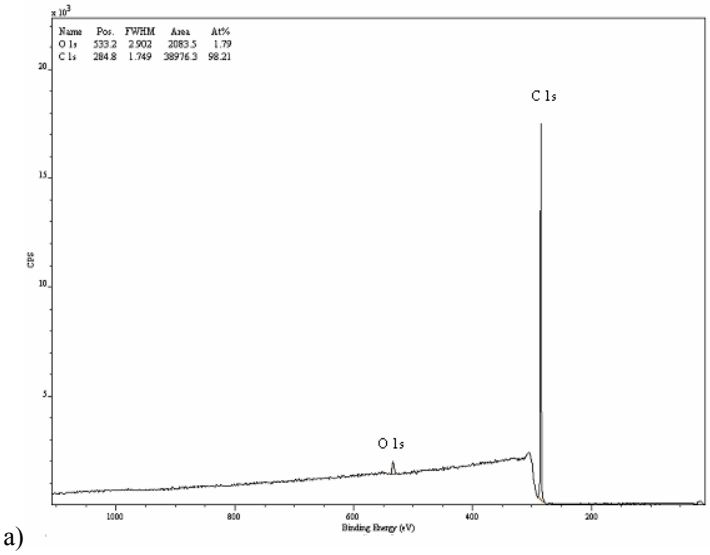

Figure IV-8. XPS spectra of SEPS: (a) before implantation; (b) after Li implantation

In the radioactive ion implantation wear measuring method it is very important that the implantation profile remains unchanged during and after the implantation, because, in order to have the same calibration curve during the wear measurement, the implanted radioactive ions have to remain at their implantation place during the

whole test. Therefore, from this point of view it was interesting to see whether implantation of heavy ions (as Kr) could be an alternative to the implantation of light ions (as ^{7}Be), even if a negative answer was expected, due to the probable modifications induced in the material (see also Chapter II, section 2.2).

3.2.1. Optical microscopy

From the optical microscopy observation, it was obvious that in the case of Kr implantation the modifications induced in the material are considerable. The behaviour of the samples was different as a function of implanted dose and the conditions after implantation, but in all cases the thickness of the film in the irradiated area was different from the rest of the sample.

For the samples kept at room temperature, the modifications following the implantation (after 24 hours) for different doses are presented in Figure IV-9. For all doses, the apparition of holes is visible. In the case of the two lower doses (samples 1N13 and 1N14), this special "hole network" is accompanied by the buckling of the sample surface.

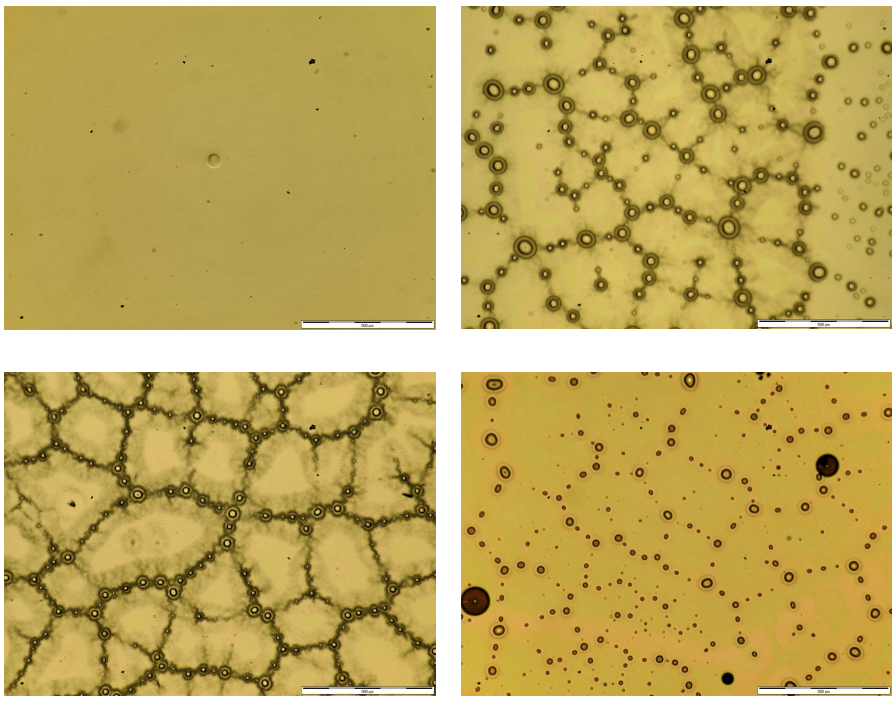

Figure IV-9. Surface optical microscopy images from unimplanted sample (upper left), implanted region on sample 1N13 ($3.6 \cdot 10^{13}$ ion/cm^2) (upper right), 1N14 ($1 \cdot 10^{14}$ ion/cm^2) (lower left) and 1N15 ($1 \cdot 10^{15}$ ion/cm^2) (lower right). The scale is 500 μm.

We examined the samples at different time intervals after the implantation. Figure IV-10 shows the evolution in time of the 1N13 sample surface at smaller scale.

For the samples kept at –18°C (freezer), for the two lower doses, no apparent modification was seen 24 hours after the implantation.. After 30 days, the appearance of the samples was comparable to that of the samples kept at room temperature, but without holes.

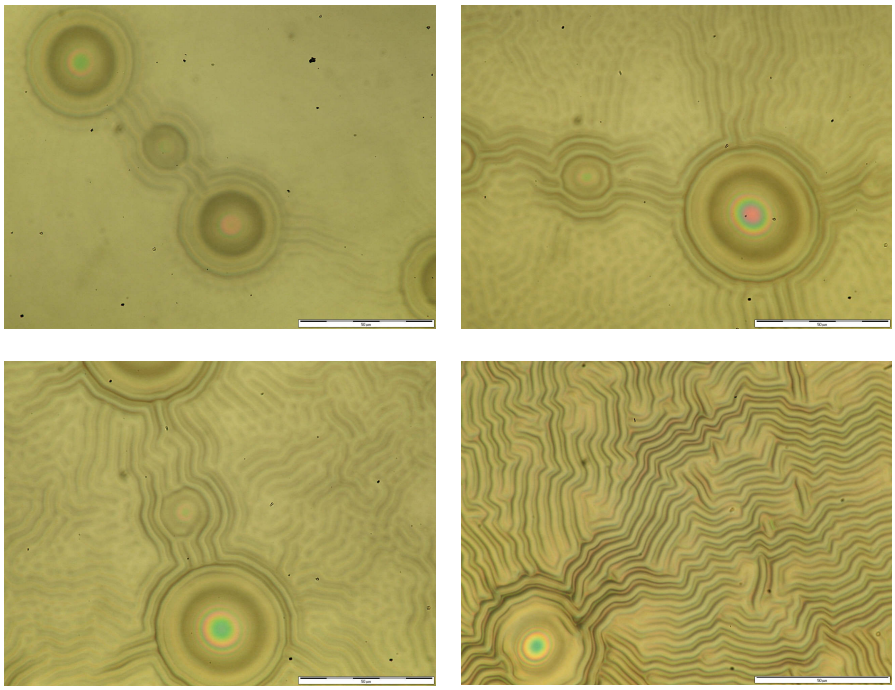

Figure IV-10. Optical microscopy images of implanted area on sample 1N13 (dose $3.6 \cdot 10^{13}$ ion/cm^2) at: 24 hours (upper left), 48 hours (upper right), 96 hours (lower left) and 30 days (lower right) after implantation. The scale is 50 µm.

The modifications (buckling) induced in the Kr implanted samples may be explained by the apparition of strong tensions between the implanted region and the unimplanted one. The tension may be due to the density gradient across the sample. The loss by evaporation of hydrogen and low molecular species created during the ion bombardment [16,17], cross-linking [18,19] or even carbonisation [20] are possible causes for the density increase in the implanted region.

For the samples implanted with the highest fluences (~10^{15} and 10^{16} ions/cm^2), no wrinkles are detectable in the implanted region. This can indicate that with increasing number of implanted ions, due to the increasing number of cross-linking, the density increase up to a level where the elasticity of the material is lost, therefore, the wrinkling is no more possible. In addition, buckling represents a

vertical heterogeneity of elastic properties and density, which may be lost for the higher doses.

This can also corroborate with the results of the FT-IR and XPS measurements (sections 3.2.3 and 3.2.4), where, with the increase of fluence over 10^{15} ions/cm^2, a decrease in the oxidation products was observed. There, a possible explanation is that the irradiation starts to induce cross-linking of the polymer, so that the number of radicals available for the oxidation is reduced.

For the high fluences, in the transition region, the orientation of the wrinkles is visible (Figure IV-11). The film is exposed to a strain that determines in some areas the collapse of the material, generating the apparition of holes for the samples kept at room temperature.

For the other set of samples, due to the low temperature of storage (-18°C), the mobility of the polymer chains was reduced, so the modification was not so severe.

A similar behaviour was reported previously, where bubble formation was observed in thin polymer films on hydrophilic solid substrates when heated (160°C in vacuum) after annealing [21]. The bubbles formed only when the polymer had unsaturated carbon double bonds. The bubbles size showed a tendency to increase with the sample thickness. The explanation given was that bubbles were generated by the release of gas resulting from the reaction between the polymer and the substrate. It is likely that in our case as well bubble of gas form due to the production of volatile components upon Kr irradiation.

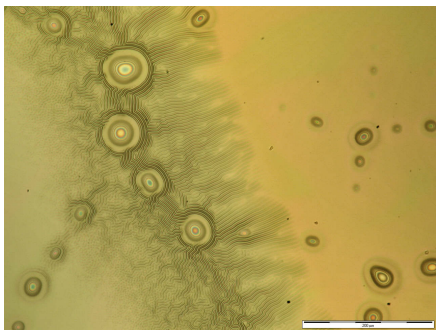

Figure IV-11. Transition region between implanted (right side) and unimplanted (left side) areas on sample implanted with $1 \cdot 10^{15}$ ions/cm^2. The scale is 200 µm.

3.2.2. Atomic force microscopy

The dimensions of the formed structure (buckles), already observed with optical microscopy, were determined using AFM. For the sample implanted with $1 \cdot 10^{15}$ ion/cm^2, the structure appears only in the transition region between the implanted

and unimplanted area. In this case, the topography of a 100x100 µm size zone is presented in Figure IV-12, together with a line profile analysis.

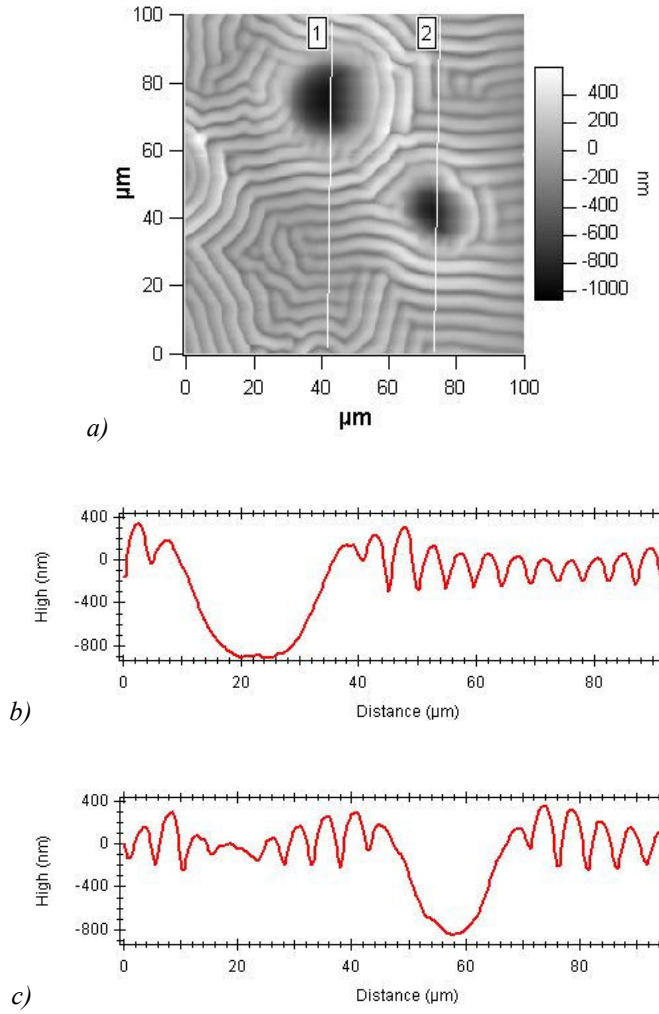

Figure IV-12. a) Topography image and topography profile along b) line 1 and c) line 2 for sample 1N15 ($1 \cdot 10^{15}$ ion/cm^2).

The AFM analysis of the samples also indicated that the copolymer morphology is modified by the implantation. The microstructure aspect is different for different regions on the sample. For example, in Figure IV-13 are presented the AFM - phase and topography - images taken with a 5 µm scanner on two distinct regions of the sample presented above. As comparison, images obtained on the unimplanted sample are also given. One sees that the regular microstructure of the original sample is fully destroyed upon irradiation.

We were not able to identify any relation between the microstructure modifications and the buckles formed after the implantation.

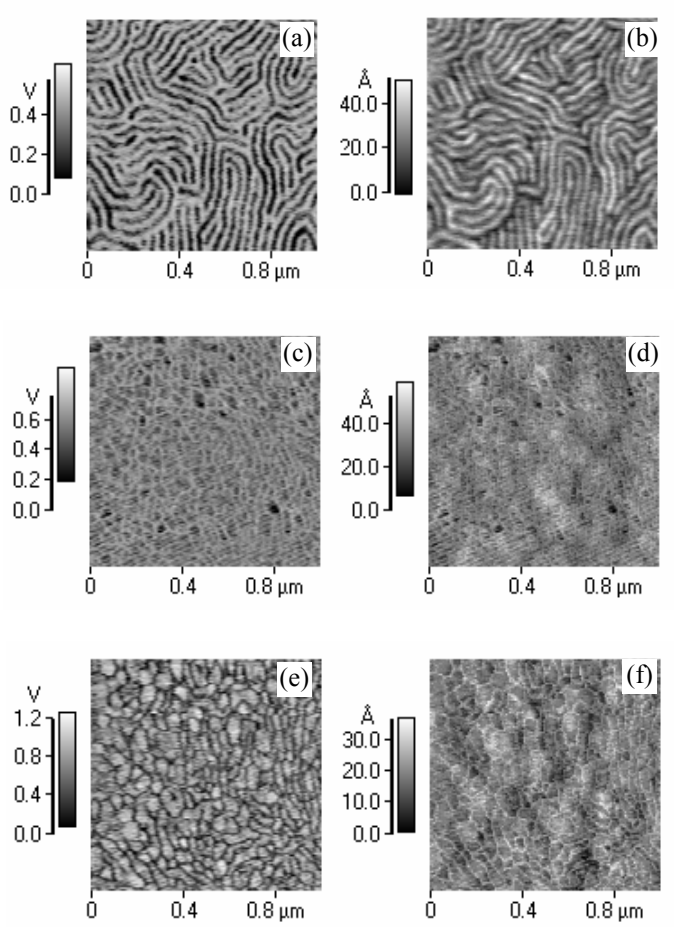

Figure IV-13. AFM phase (left) and topographic (right) images taken on: a), b) unimplanted sample, c), d), e), f) sample implanted with $1 \cdot 10^{15}$ ion/cm^2.

3.2.3. Fourier Transform Infrared Spectroscopy

The interference fringes were different in the implanted and unimplanted regions. For the unimplanted regions, we were not able to distinguish any modification of the refractive index from the amplitude and period of the interference fringes.

The situation was different for the implanted regions (Figure IV-14), were a strong alteration of the amplitude of the fringes was visible. The amplitude increased with the dose, indicating an increase of the refractive index of the material.

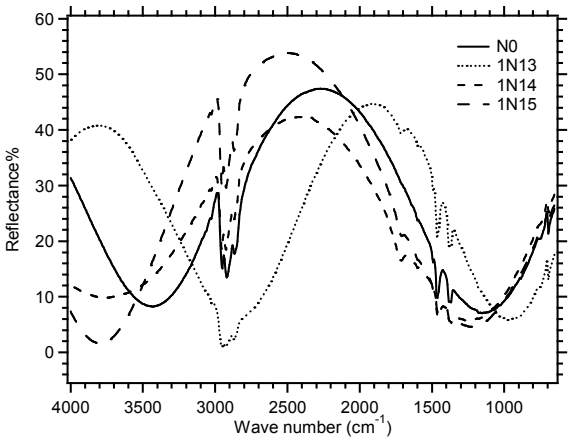

Figure IV-14. Experimental FT-IR spectra of Kr implanted sample (implanted regions). 1N13, 1N14 and 1N15 are samples kept at room temperature. For comparison, the spectrum of the unimplanted SEPS sample is given.

The physico-chemical modification induced in the polymer film during the irradiation was so important that we were not able to simulate the interference phenomena in this case using the model of a two-layer system. A possible explanation could be that during the irradiation, portions of the copolymer are strongly modified (cross-linking, carbonisation etc.), so a practically new material layer (or layers) appears. This would be in good agreement with the observation of buckles, since such phenomena appear when layers of different elastic moduli are submitted to compression forces.

The same comportment was observed for the samples kept in the freezer.

We managed more or less to correct the spectra in the region 2000-650 cm^{-1}. A normalisation of the spectra was necessary, because the sample thickness was modified during the implantation. The two sets of samples presented a different behaviour.

For the samples stored at room temperature (Figure IV-15) a broad band appeared in the 1900-1600 cm^{-1} wavelength interval (C=O str.) for all regions and no peaks were detected in the C-O-C characteristic regions. The band, with a maximum at 1716 cm^{-1} presented several shoulders indicating the presence of ketones, aldehydes, carboxylic acids and lactones.

For the implanted regions, the intensity of the carbonyl peak was higher than the specific peak at 1465 cm^{-1} ($-CH_2-$ scissoring) for doses equal or larger than 10^{14} ions/sample. This may be considered as an indication of a huge number of scissions in the polymer chains.

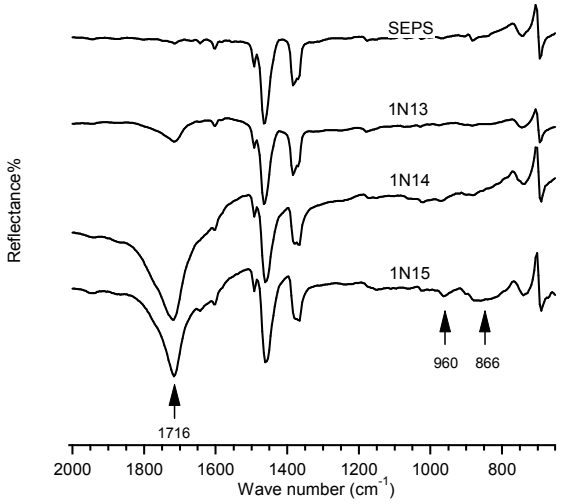

Figure IV-15. Corrected spectra for Kr implanted samples stored at room temperature. Implanted regions. Normalisation on the peak at 1461.8 cm^{-1}.

The intensity of the peak increased with the ion dose; however, for the higher dose ($1 \cdot 10^{15}$ ions/cm^2), a decrease was observed. This behaviour was also observed in the course of XPS analyses of the sample surfaces which is presented in section 3.2.4 of this chapter. In this situation it is possible that the irradiation starts to induce cross-linking of the polymer, so that the number of radicals available for the oxidation is reduced [22].

In addition, for the region implanted with 10^{15} ions/cm^2 new peaks appeared at approximately 866 and 960 cm^{-1} (CH out-of-plane bending of RR'C=CHR" and trans R-CH=CH-R', respectively).

In the spectra of the unimplanted (Figure IV-16) areas the intensity of the carbonyl peak is less important, but is still comparable to the $-CH_2-$ scissoring peak and is almost independent on the ion dose. The presence of this type of oxidation in the unimplanted regions may indicate that the heating of the sample during the implantation was considerable and affected the entire sample [23].

For the samples kept in the dark at approximately –18°C (freezer), we were not able to detect any significant modification in the spectra, even for the implanted regions. The diffusion of the oxygen in the samples was slowed down by the decrease in the permeability of the copolymer in the vicinity of the glass transition temperature (~13°C). This indicates that in the samples not stored in the freezer, the irradiation first generates radicals that transform progressively by reacting with oxygen or other radicals, provided the mobility of chains is high enough.

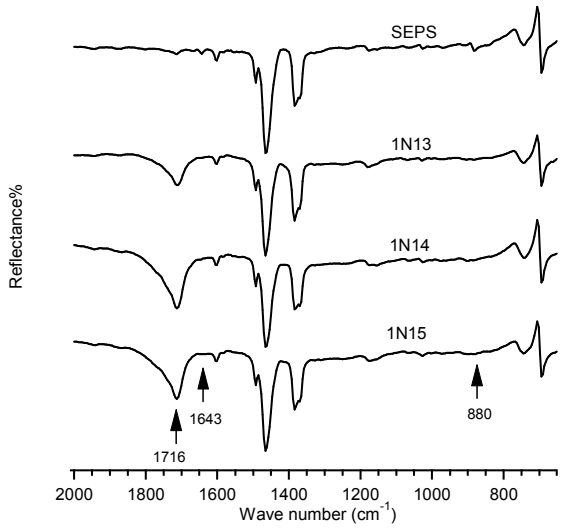

Figure IV-16. Corrected spectra for Kr implanted samples stored at room temperature. Unimplanted regions. Normalisation on the peak at 1461.8 cm^{-1}.

3.2.4. X-ray Photoelectron Spectroscopy

The XPS spectra of the unimplanted SEPS and sample implanted with the dose of $1 \cdot 10^{15}$ ion/cm^2 are shown in Figure IV-17.

In the pristine sample, the oxygen to carbon atomic ratio (O/C) is 0.0067. The oxygen content in the samples increases with the dose, up to $1 \cdot 10^{14}$ ion/cm^2. At higher doses, a decrease in the oxygen content can be observed (Figure IV-18).

A similar behaviour was observed during the FT-IR measurements of the Kr implanted copolymer samples. We can conclude that for the two lower Kr doses irradiation-induced bond scission results in the incorporation of oxygen. With the increase of the dose above a certain value, the probability to cause simultaneous displacement of two atoms from neighbouring chains and create two radical pairs for cross-linking will increase also. For this reason, for the two higher doses, the decrease in the oxygen content may be explained by the copolymer cross-linking.

This is also supported by the optical microscopy results, where an increase in the density of the implanted region of the sample due to an increase in the cross linking was concluded for fluences larger than 10^{15} ions/cm^2 (section 3.2.1).

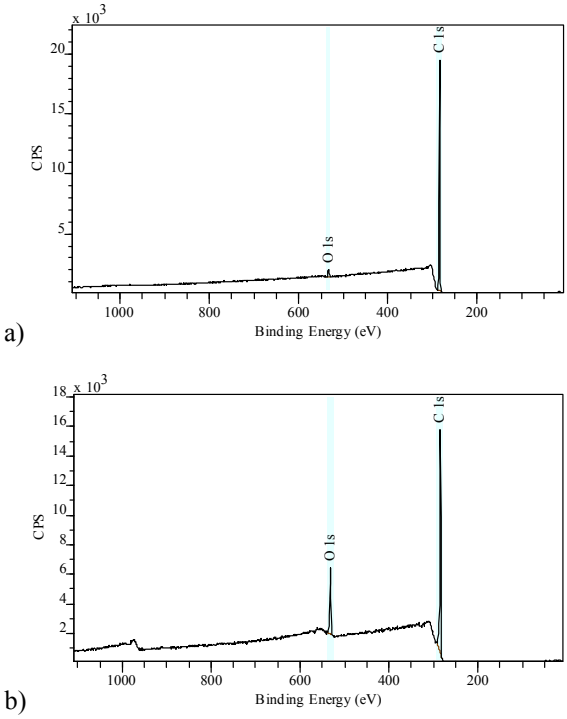

Figure IV-17. XPS spectra of a) unimplanted sample and b) sample implanted with $1 \cdot 10^{15}$ ion/cm^2.

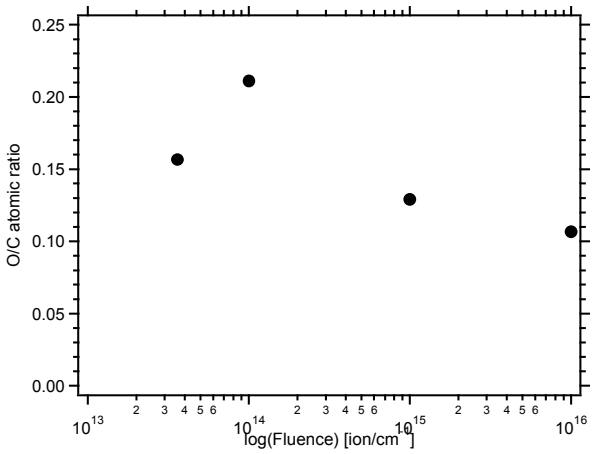

Figure IV-18. O/C ratio in the Kr implanted samples as a function of ion fluence.

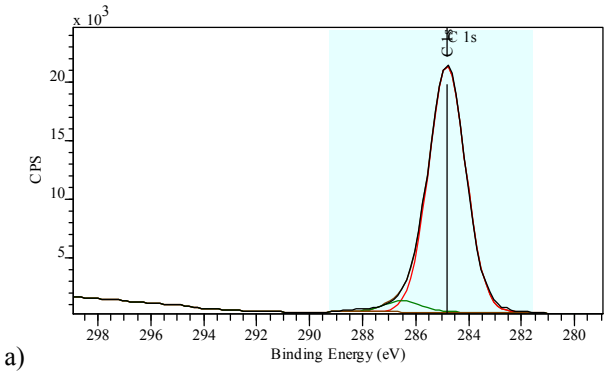

Figure IV-19. The XPS C 1s spectra for a) pristine SEPS and b) implanted with $1 \cdot 10^{15}$ ion/cm^2.

Figure IV-19 shows the XPS C 1s spectra of the unimplanted SEPS and sample implanted with the dose of $1 \cdot 10^{15}$ ion/cm^2, and Figure IV-20 presents the XPS O 1s spectra of the same samples. It can be seen in Figure IV-19 that Kr ion implantation induces the apparition of new chemical bonds in the surface layer. In the unimplanted copolymer the C 1s peak consists of C-(C,H) (≈284.8 eV) and C-O (≈286.5 eV) bonds. After irradiation, new component peaks appear, corresponding to O=C-O-C (≈288 eV) and O=C-OH (≈290 eV) groups.

Different from the behaviour of oxygen content, if we look only to the O=C-O bonds fraction, a continuous increase with the dose is visible (Figure IV-21).

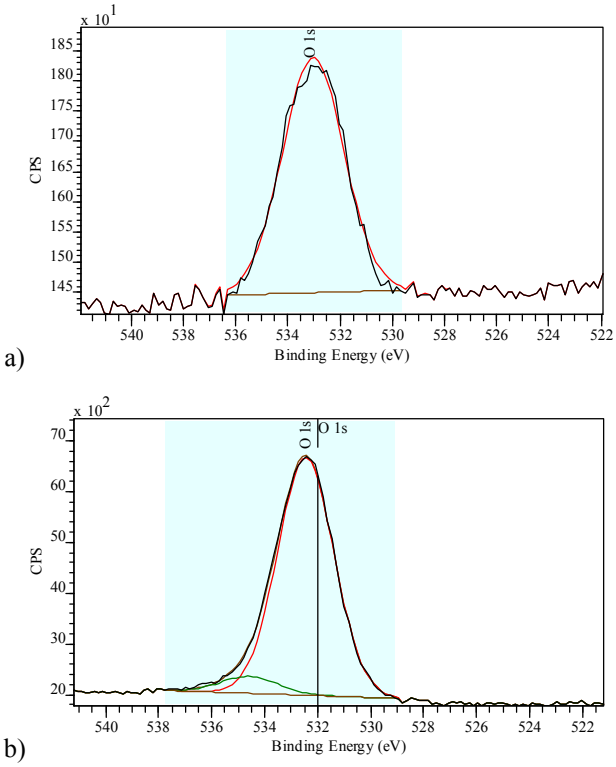

Figure IV-20. The XPS O 1s spectra for a) pristine SEPS and b) implanted with $9.8 \cdot 10^{14}$ ion/cm^2.

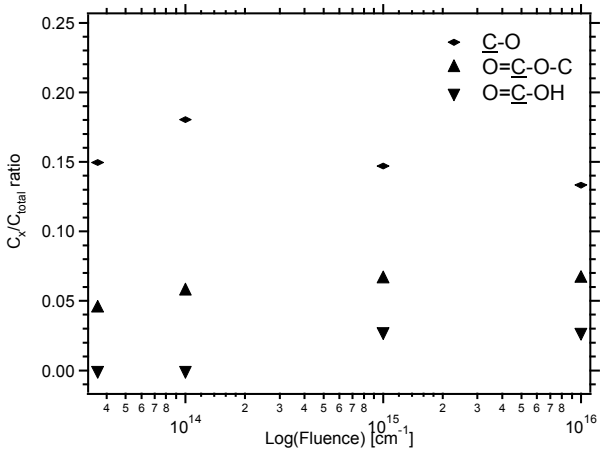

Figure IV-21.. Ratio of carbon bound in different functional groups to the total carbon content in the irradiated samples as a function of fluence.

4. Conclusion

As it was expected based on the theoretical considerations presented in Chapter II, the ^{7}Li and ^{7}Be ion implantation, in the selected conditions, does not induces significant modifications in the materials, even in the more sensitive SIS copolymer. The small amount of oxidation products formed and detected by IR spectroscopy probably will not influence the mechanical properties (wear resistance) of the material. They also appear in the SIS copolymer by simple oxidation in air, in absence of implantation. However, this hypothesis has to be checked by performing wear test on implanted and pristine samples.

Another important conclusion is that the modifications observed in the ^{7}Be implanted copolymer samples are induced by the ion implantation and by the γ and X-rays emitted by the radioactive ions, this part of the degradation being relatively important.

On the contrary, in the case of Kr ions implantation, the samples were strongly modified, even more than predicted by the theory. The modifications induced in the material are so important that not only the wear properties of the copolymer are modified, but also new material layers are created, as indicated for example by the changes of the interference fringes in the spectra of the copolymer. Therefore, although from the point of view of redistribution during and after the implantation heavy ions as Kr could be better candidates for the implantation than light ions as ^{7}Be (see introduction of section 3.2 of present chapter), there is no perspective in using heavy ions as Kr within the radioactive ion implantation wear measuring method in polymers.

The optical microscopy observations, together with the FT-IR and XPS measurements indicated that for low ion fluences, irradiation-induced bond scission results in the incorporation of oxygen. With the increase of the dose above a certain value, the probability to create two radical pairs for cross-linking will increase also. For this reason, for the two higher doses, the decrease in the oxygen content may be explained by the copolymer cross-linking.

Due to the vertical heterogeneity of the elastic moduli after irradiation (layering), and to the apparition of compression stress resulting from evaporation and cross-linking, buckling of the surface occurs. It is interesting to note that this wrinkling of polymer surfaces under ion bombardment has recently been proposed for the formation of a “stiff skin”, with protecting role on polymeric substrates [24].

5. References

1. www.srim.org

2. K.D. Jandt, Atomic force microscopy of biomaterials surfaces and interfaces, Surface Science 491 (2001) 303.

3. R. Garcia, R. Perez, Dynamic atomic force microscopy methods, Surface Science Reports 47 (2002) 197.

4. A. Van der Lee, Grazing incidence specular reflectivity: theory, experiment and applications, Solid State Sci. 2 (2000) 257.

5. J. Coates, Interpretation of infrared spectra, a practical approach, in Encyclopaedia of Analytical Chemistry, Wiley, Chichester, 2000, p. 10815-10837.

6. G. Socrates, Infrared and Raman characteristic group frequencies: tables and charts, Willey, 2004.

7. G. Choppin, J.O. Liljenzin, J. Rydberg, Radiochemistry and nuclear chemistry, 3rd ed., Chalmers Univ., 2002, p187.

8. J. Guillet, Polymer photophysics and photochemistry, an introduction to the study of photoprocesses in macromolecules, Cambridge University Press, 1985.

9. H.F. Mark, N.M. Bikales, C.G. Overberger, G. Menges, Enciclopedia of polymer science and engineering, Vol. 13, Wiley, New York, 1985, p. 667-707.

10. V. Gueguen, L. Audouin, B. Pinel, J. Verdu, Radiochemical oxidation of an ethylene-propylene-hexadiene terpolymer, Radiat. Phs. Chem. 44 (1994) 557.

11. C. Decker, F.R Mayo, Aging and degradation of polyolefins II : γ-initiated oxidations of atactic polypropylene, J. Polym. Sci. Polym Chem. 11 (1973) 2847.

12. C. Decker, F.R Mayo, H. Richardson, Aging and degradation of polyolefins III : Polyethylene and ethylene-propylene copolymers, J. Polym. Sci. Polym Chem. 11 (1973) 2879.

13. M.R.F. Soares, L. Amaral, M. Behar, D. Fink, Diffusion of Ag implanted into the AZ1350 photoresist, Nucl. Instr. and Meth. in Phys. Res. B 191 (2002) 690.

14. K.M. Wang, B.R. Shi, J.T. Liu, X.D. Liu, K. J. Yao, Range profiles of Hg^{+}, Hg^{2+}, Hg^{3+} in polymer polyvinylalcohol, J. Appl. Phys. 66 (1989) 4577.

15. R.B. Guimaraes, M. Behar, R.P. Livi, J.P. de Souza, F.C. Zawislak, D. Fink, J.P. Biersack, Mass and energy dependence of implanted ion profiles in the AZ111 photoresist J. Appl. Phys. 60 (1986) 1322.

16. J. Chen, F. Zhu, H. Pan, J. Cao, D. Zhu, H. Xu, Q. Cai, J. Shen, L. Chen, Z. He, Surface modification of ion implanted ultra high molecular weight polyethylene, Nucl. Instr. and Meth. in Phys. Res. B 169 (2000) 26.

17. A. Valenza, A.M. Visco, L. Torrisi, N. Campo, Characterization of ultra-high-molecular-weight polyethylene (UHMWPE) modified by ion implantation, Polymer 45 (2004) 1707.

18. J.S. Chen, S.P. Lau, Z. Sun, B.K. Tay, G.Q. Yu, F.Y. Zhu, D.Z. Zhu, H.J. Xu, Structural and mechanical properties of nitrogen ion implanted ultra high molecular weight polyethylene, Surf. Coat. Technol. 138 (2001) 33.

19. T. Kobayashi, A. Nakao, M. Iwaki, Wear properties of tungsten-implanted polyimide, Nucl. Instr. and Meth. in Phys. Res. B 206 (2003) 1110.

20. D. Fink, R. Klett, L.T. Chadderton, J. Cardoso, R. Montiel, H. Vazquez, A.A. Karanovich, Carbonaceous clusters in irradiated polymers as revealed by small angle X-ray scattering and ESR, Nucl. Instr. and Meth. in Phys. Res. B 111 (1996) 303.

21. J. Kim, H.H. Lee, Bubble formation in thin polymer films on solid substrates, Macrom. Mater. Eng. 286 (2001) 201.

22. A. Kondyurin, R. Khaybullin, N. Gavrilov, V. Popok, Pulse and continuous ion beam treatment of polyethylene, Vacuum 68 (2003) 341.

23. A. Chapiro, General considerations of the radiation chemistry of polymers, Nucl. Instr. and Meth. in Phys. Res. B 105 (1995) 5.

24. M-W. Moon, S. H. Lee, J-Y. Sun, K. H. Oh, A. Vaziri, J. W. Hutchinson, Wrinkled hard skins on polymers created by focused ion beam, Proc. Nat. Acad. Sc. of U.S.A, 104 (2007) 1130.

Chapter V
Implanted ^{7}Be ions diffusion in SEPS copolymer

1. Introduction

The key aspect of the radioactive ion implantation wear measuring method is to know with precision the distribution of the radioactive ions in the sample, namely, to establish with precision the calibration curve (see Chapter I, section 3).

In Chapter III we demonstrated that the theoretical predictions of the implantation distribution are confirmed by experimental measurements; therefore, it can be considered that the implantation profile can be established by means of simulations. The question which remains to be answered to is what happens with the ions immediately after the implantation and later, because, in order to have the same calibration curve during the wear measurement, the implanted radioactive ions have to remain at their implantation place during the whole test.

This issue was presented in Chapter II, section 3, when the possible redistribution of implanted ions during or after the implantation was discussed, by reference to possible experimental techniques used in the determination of the implanted ion distributions, their principles and limitations. Theoretical aspects linked to the redistribution of the implanted ions at room temperature were also considered.

At that time, we emphasized that the main problem with all the existing experimental techniques is their detection limit. None of them is able to detect light elements (Li, Be, B) implanted in polymer targets at fluences less or equal to 10^{13} cm^{-2}, with implantation depths of a few μm. From the point-of-view of radioactive ions implantation for wear measurement, where the fluences are kept as low as possible (10^{10}-10^{11} cm^{-1}) in order to avoid material degradation and for radioprotection reasons, this value is already much too high.

Therefore, to our knowledge, up to present, no studies were performed in order to establish whether the Be^{7} ions diffuse after or during the implantation process. From our point of view, it is essential to elucidate this aspect, in order to establish whether or not the Be^{7} radioactive ion implantation wear measuring method is a reliable wear measuring method for polymers.

In order to achieve this goal, we decided to implant Be^{7} ions with a known theoretical distribution in the copolymer material used in the previous experiments and to remove layers of material using plasma etching. As indicated in Figure V-1, by measuring the thickness of the remaining layer and the corresponding remaining

activity, the calibration curve can be reconstructed. The corresponding depth profiles are obtained by derivation.

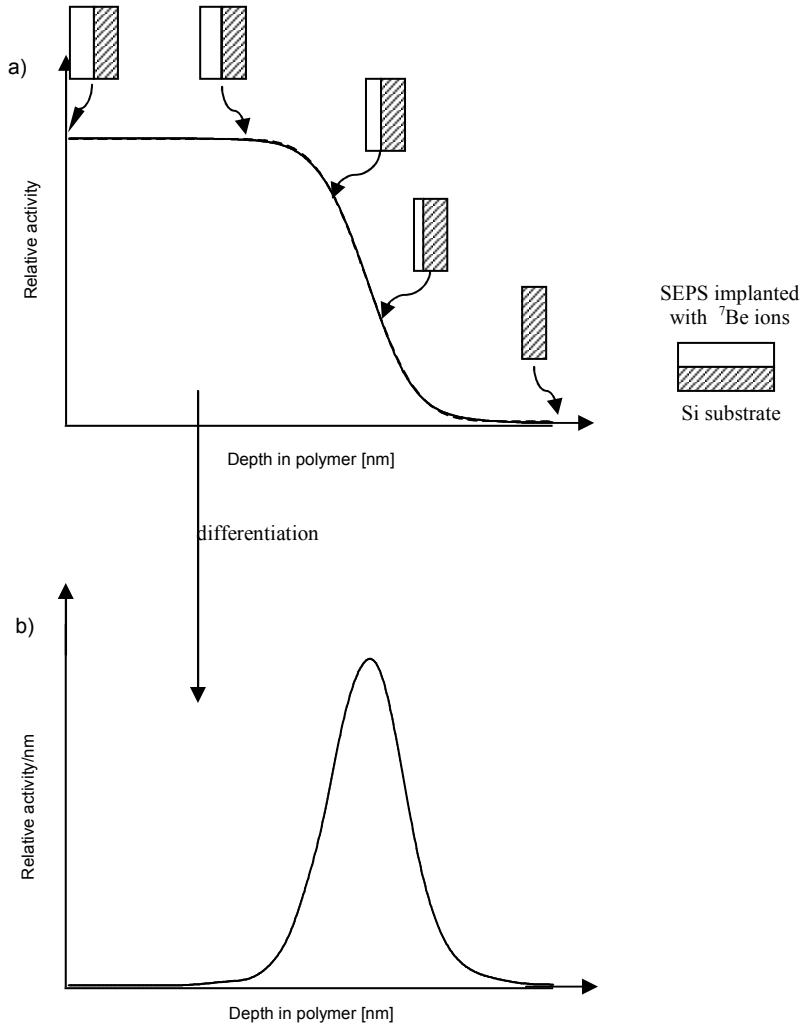

Figure V-1. a)Schematic of the methodology used to determine the experimental calibration curves; b) the corresponding depth profiles

At the beginning of this chapter, some theoretical aspects related to the plasma etching processes are presented and the accent is put on the plasma etching of polymers. Plasma parameters with effects on the etching rates of polymers (section 2.2.1) and the influence of some physical and chemical properties of the polymer (sections 2.2.2 and 2.2.3) are presented.

The experimental section 3, gives details about the sample preparation method, ion implantation, the parameters of the plasma etching process and the analysing and characterisation methods used (radioactivity measurement, thickness measurement by spectroscopic ellipsometry and atomic force microscopy).

The results and discussion (section 4) are divided in three parts, the first two related to the plasma etching process, namely, the determination of the etching speed of the copolymer, and AFM microscopy results about modifications induced on the polymer surface. The last part of section 4 gives the results of the experiments on the diffusion of the implanted Be^{7} ions in the SEPS copolymer sample.

2. Plasma etching

2.1. Generalities

The chemical/physical removal of a material from a substrate, also known as etching, is one of the most widely used subtractive techniques for micromachining. Etching may be divided in two main groups: gas and vapour phase dry etching processes and liquid phase etching. In the following, we will concentrate only on the dry etching techniques; liquid phase etching is not related to the subject of the present work.

Dry etching covers a family of methods by which the material removal is obtained, physically by ion bombardment, chemically by a chemical reaction through a reactive species at the surface, or by combined physical and chemical mechanisms. Plasma-assisted dry etching is categorised according to the specific setup as **glow discharge**, where the plasma is generated in the same vacuum chamber where the sample is located or **ion beam techniques**, where plasma is generated in a separate chamber from which ions are extracted and directed in a beam toward the sample by a number of grids.

Taking into account that the ion beam techniques were already presented in Chapter II together with the problems related to these methods, in this chapter we will focus on the glow discharge methods. Three alternatives are generally used, namely, reactive gas plasma etching (chemical mechanisms), reactive ion etching (physical/chemical mechanisms) and sputter etching with an inert plasma gas (physical mechanisms). In the following section, different aspects linked to the plasma etching techniques are developed for the case of a polymer sample.

2.2. Plasma etching of polymers

Plasma etching of polymers can proceed through three different pathways.

Firstly, a polymer substrate is etched by chemical reaction of reactive plasma species (e.g. radicals, ions) with the surface, referred to as chemical etching. In chemical etching, activated gas phase species merely react with a surface resulting in the formation of volatile products. The reactive etchant species are created by the plasma through collisions of accelerated, energetic free electrons with gas molecules, which induces dissociation or excitation of the feed gas (e.g. O_2, CF_4, Ar). These inelastic electron-neutral collisions maintain the supply of ions, metastable species and radicals that are continuously lost by reaction and recombination. Examples of reactions that can occur in the plasma phase can be found in the literature [1,2].

The chemical etching process can be summarised by as many as six primary steps, as illustrated in Figure V-2.

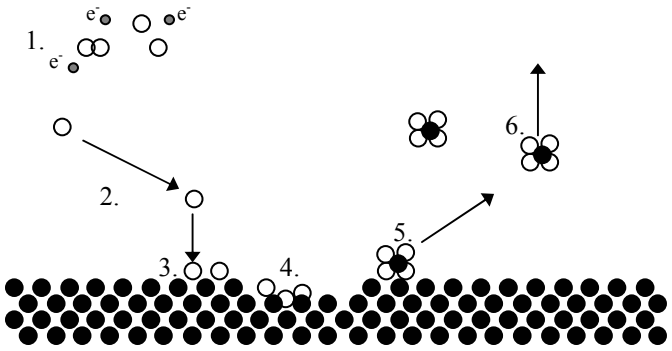

Figure V-2. Primary process occurring in a chemical plasma etching process: 1. Generation of etchant species; 2. Diffusion to surface; 3. Adsorption; 4. Reaction; 5. Desorption; 6. Diffusion into bulk gas [3].

Secondly, during gas plasma etching, the surface of a polymer is slowly sputtered by the bombardment of ions from the plasma phase, which is a physical process. When a substrate is exposed to plasma, it will directly be negatively charged by accelerated electrons. As a result, low energetic positive ions are accelerated through the plasma sheath towards the substrate surface. In this way, material fragments are ejected from the surface, which makes sputtering a purely physical process [4]. Due to this physical component of the reactive ion etching process, which tends to affect most materials similarly, the achievable selectivity is less than that attainable in chemical etching processes [5].

Finally, the plasma is also a source of ultraviolet radiation, having energies greater that some polymer ionisation potentials, resulting in several effects on organic materials [6,7]. Firstly, vacuum ultraviolet radiation with wavelengths of less than 178 nm can cause photo-ionization. Furthermore, ultraviolet radiation can cause

dissociation of bonds yielding free radicals and may excite specific groups [8,9]. This can lead to chain scissions, which leads to formation of low molecular weight material, rearrangements or even elimination of that specific functional group [10]. The radicals created on the surface can cause cross-linking [11], can react with species from the plasma phase or can react with oxygen to form peroxides, when exposed to air afterwards.

The chemical effects of the bombardment of electrons on the surface have to be also taken into account. Because low energetic electrons have a substantial penetration depth in insulators (larger than 500 Å for 20 eV electrons [12]), their action is not restricted to the outermost surface. It seems likely that the electrons are substantially retarded when they approach a self-biased substrate in plasma, resulting in an increased penetration depth.

In general, these three etching mechanisms occur simultaneously during the plasma treatment of a polymer and induce a flow of volatile (low molecular weight) products from the substrate to the plasma [3]. This causes a gradual weight loss of the treated polymeric material.

The etching rate (Å/s) of a polymer largely depends on the plasma treatment conditions (e.g. discharge gas, pressure, discharge power, substrate temperature, and treatment time) and on the polymer's chemical and physical properties [13].

2.2.1. Plasma parameters influencing the etching rates of polymers

Probably, the most important discharge parameter is **the type of gas** (etchant) being used. Oxygen gas plasmas are known to be very reactive etchants. This reactivity is due to the reaction of atomic oxygen with a polymer surface, which is the starting point for the etching process. Attack of a polymer by atomic oxygen can proceed through a variety of mechanisms including abstraction, addition to unsaturated moieties, or to a lesser extent by absorption of the O_2 dissociation energy [14]. After atomic oxygen attack, the radical site can be subsequently attacked by molecular oxygen leading to significantly weakened C-C bonds. A possible autoxidation process leading to bond weakening was also proposed [15]. From these created structures, polymer backbone chain scissions can occur, eventually leading to volatile etch products such as CO and CO_2 [16].

Addition of fluorine containing gases , such as CF_4, C_2F_6, SF_6 to an oxygen plasma will even further increase the etching rate of a polymer by increasing oxygen atom concentrations relative to those obtained in pure oxygen plasmas [17]. It appears that the major role of fluorinated gas addition in increasing oxygen atom densities in the plasma is by increasing the number density and/or energies of electrons in the plasma [18].

Gas additives as N_2 and N_2O are among the gases that, when added to oxygen, produce increased oxygen atom concentrations in the plasma and result in larger polymer etching rates [19].

Inert gases like argon or helium generally induce relatively low etching rates compared to oxidative and fluorinating plasmas (rule of thumb: $Ar<CF_4<CO_2<air<O_2$). Inert gas plasma can induce cross-linking at a polymer surface as well as modifications of the surface roughness [20,21].

The plasma etching rate of a given polymer increases with **discharge power** [22]. Upon higher energy input, the density of plasma reactive species as well as their acceleration towards the substrate will increase, resulting in more severe etching of the substrate's surface.

The etching rate of a polymer substrate also increases upon **temperature** elevation during plasma treatment. Besides accelerated etching reactions, low molecular weight etch products will evaporate more easily at higher substrate temperatures which may further increase the etching rate. While higher temperatures induce higher plasma etching rates, plasma etching in its turn leads to an increase of surface temperature [23]. A continuous surface bombardment of plasma reactive species induces heat development, while exothermic surface chemical reactions will also generate energy. Due to the low thermal conductivity of most polymers, the surface temperature can be raised considerably during continuous plasma etching. Besides influencing the etching rate this increase in temperature might also have a major effect on the polymer surface structure.

The etching rate of polymers can be significantly enhanced when a **bias voltage** is applied to the polymer substrate (cathode), which results in a bombardment by ions of higher energy.

Although the **plasma pressure** is an important discharge parameter, its effect on the etching rate is ambiguous. Upon rising plasma pressures, increases as well as decreases of etching rate have been observed [24]. A plausible explanation can be found in the fact that higher pressures increase the plasma gas concentration, but also decrease the electron density. The concentration of plasma reactive species, which directly influences the etching rate, results from the superposition of these counteracting effects. Furthermore, the energy of the ions impinging on the substrate decreases with rising pressure, which reduces the sputtering effect.

In general, plasma etching will reach an equilibrium state (i.e. constant etching rate) in the course of treatment time. Initial fluctuations of the etching rate may arise due to changes of surface temperature and surface chemistry. For example, cross linking in the surface layer of the substrate during plasma treatment could suppress the initial etching rate of a polymer.

2.2.2. Etching rate versus chemical structure

The chemical structure of polymers has a major influence on the etching rate. Many studies have been aimed at providing more understanding about the relation between etch resistance and a polymer's chemical structure [15,25,26]. One of the first studies in this field was performed by Taylor and Wolf who studied the oxygen plasma etching behaviour of 40 different polymers [27]. They found that the strength of polymer backbone bonds mainly determines the rate of weight loss in most cases. Weak backbone bonds enhance polymer removal, while weak backbone-side chain bonds also enhance degradation. Weak bonds not immediately pendant to the main polymer chain have little effect on the etching rate. They also concluded that aromatic functional side groups and certain polar functional side groups promote etch resistance, possibly by enhancing deactivation of normally reactive species. Finally, they found that organometallic polymers such as poly(dimethyl siloxane) exhibit extremely good etch resistance, most likely due to the formation of a thin metal oxide layer that protects the polymer from further etching.

In general, some basic guidelines can be formulated concerning the etching behaviour of polymers in relation to their chemical structure [27]:

- Aromatic polymers have lower etching rates than their aliphatic analogues.

- Polymers containing little (or no) oxygen and no halogen other than fluorine are most resistant to oxygen plasma etching.

- Polymers containing chlorine are rapidly eroded in an oxygen plasma (weak C-Cl bonds).

- Cyano (-CN) and fluorine substituents in the polymer enhance the etch resistance, due to strong bonding to the backbone chains.

2.2.3. Etching rate versus physical properties

Besides the chemical structure, the physical properties (melting temperature, glass-transition temperature, crystallinity) of a polymer also influence the etching rate. Polymers with a high thermal stability are likely to be less susceptible than low-melting polymers [28], since a substantial temperature rise can be expected at the polymer's surface during plasma etching (discussed in section 2.2.1).

For semi-crystalline polymers it is generally known that the crystalline regions are more etch resistant than the amorphous segments [29]. The results of this study indicated that the amorphous regions of PE were preferentially etched during the treatment with ultraviolet radiation in the presence of ozone, resulting in a fine scale surface topography.

The most plausible explanation for the etch selectivity in semi-crystalline polymers is found in the fact that the permeability of plasma reactive species into a dense, crystalline structure is lower than into loosely packed, amorphous material. The

diffusion of reactive particles into a polymer is known to be an important factor in the chemical etching processes of materials.

3. Experimental section

3.1. Copolymer films preparation

The material used was the SEPS poly(styrene-*block*-(ethylene-*co*-propylene)-*block*-styrene) tri-block copolymer, with the commercial name Hybrar 7215, already presented in Chapter I, section 4.3. The samples were prepared by spin coating from a toluene solution (150 mg/ml) on silicon substrate at 400 rpm, in order to obtain copolymer films with thicknesses larger than 5000 nm. The solvent was evaporated at room temperature, under a vacuum, for 24 hours. The samples were then annealed for 18 hours, under a vacuum, at 150°C.

Due to the low rotation speed of the spin coater, the thickness of the film was not uniform over the surface of the substrate. Thus, on each sample, regions with a uniform thickness were selected and marked for the implantation experiments and for the plasma etching experiments.

3.2. Ion implantation

The description of the implantation facility is given in the Annexe A. As mentioned in the introduction of this chapter, the scope of the implantation was to implant ^{7}Be ions in the SEPS films to a known depth, approximately 4000 nm, with a narrow implantation profile. Therefore, as indicated by the theory (simulation using SRIM), the energy of the ion beam had to be around 1380 keV.

Based on the results of our previous experiments presented in Chapter III, table III-4, for this experiment, the initial beam energy was 7 MeV and the two energy degraders were used, the gold foil in vertical position and the aluminium foil at 41.4° toward the vertical. Figure V-3a presents the drawing of the experimental setting used for the ^{7}Be ion implantation in SEPS films on silicon substrate and Figure V-3b presents the resulting implantation profile. Before the implantation, the energy distribution of the Be^{7} beam after the two degraders was recorded using the detector and electronic configuration presented in Chapter III, section 2.2.

A circular mask with a diameter of 0.8 cm was used; thus, the implanted surface area was 0.5 cm^2. Due to the low and oscillating ^{7}Be beam current, with an intensity of approximately 0.7 pA, the implantation of the first sample (S1) necessitated around four and a half hours. For the second sample (S2), the time required to implant approximately the same number of ions was only one hour and a half, at a beam intensity of approximately 3 pA.

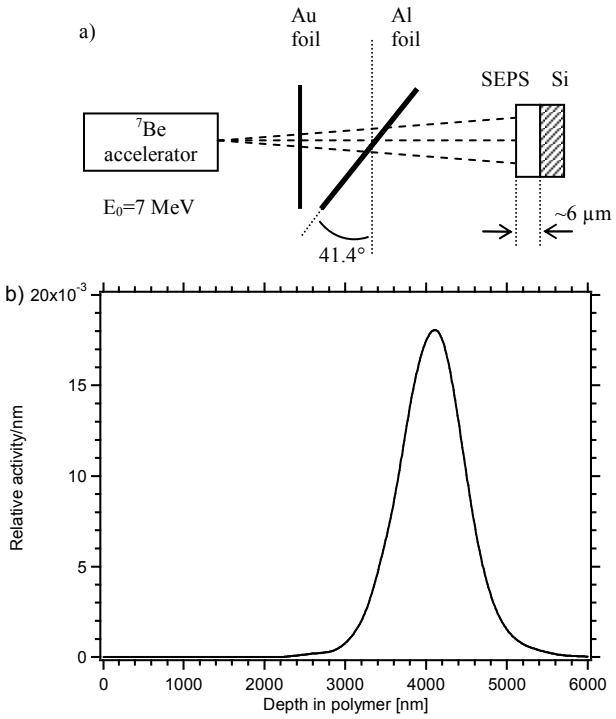

Figure V-3.a) Drawing of the experimental setting used for the ^{7}Be ion implantation in SEPS films on silicon substrate; b) Implantation profile

Immediately after implantation, the implanted sample was placed in sealed boxes and introduced in a Dewar containing liquid nitrogen. In this way, the diffusion of the ions after the implantation was stopped. At the same moment, an unimplanted sample was also introduced in the liquid nitrogen reservoir, in order to be used later, as a reference sample, during the plasma etching experiments.

3.3. Plasma etching

In our case, the material to be removed in layers is a copolymer material, including a hard phase (polystyrene) and a soft, rubbery phase; therefore, the key-point was to decide on a method with low selectivity and high etching rate to avoid enriching the material in polystyrene upon etching. As it was presented before, reactive ion etching is a combination of chemical and physical etching, resulting in high etch rates and low etch selectivity, therefore, the best solution for our problem.

Reactive-ion-etching (RIE) with an oxygen plasma has been performed in an Electrotech Plasmafab 310-340 parallel-plate system with an RF generator operating

at 13.56 MHz. The oxygen pressure was 15 mTorr, with a power of 100 W and the etch time was varied in order to keep the thickness of removed layer per etching step relatively constant.

Oxygen plasma was selected for its low selectivity and high etching rate compared to other gases (He, Ar, Xe, N_2) [30,31]. Another reason was that oxygen plasma induces less structural modifications on the polymer surface exposed to plasma treatment [32,33].

Some trials were made, in order to find out the etching time necessary for the removal of a approximately 400 nm thick copolymer layer. The results indicated that with each etching step, the time needed to obtain the same removal rate increased. This was a warning about the variation of the etching rate with the total etching time for the given sample.

In the first plasma etching experiment, a set of thirteen unimplanted samples, one reference sample plus twelve samples was put in the etching chamber. After each etching step, one of the twelve samples was removed and the thickness of the reference sample was measured. In this way, the etching rate was monitored during all the process, and the twelve samples were used afterwards for an AFM study of the modifications induced by the plasma on the material surface.

The following two experiments were performed on implanted samples. For the etching rate determination, unimplanted samples were also used, in order to establish whether the behaviour of the copolymer is changed by the ion implantation.

For the first plasma experiment with implanted sample, the first sample (S1) was used, because the total time spent at room temperature was already longer (four and a half hour implantation time compared to one and a half hour implantation time for the second sample). We decided that for the second experiment, the second sample would be removed from liquid nitrogen at a moment of time depending on the results of the first diffusion experiment.

For the second plasma etching experiment, sample S2 was removed from liquid nitrogen six days before and was kept at room temperature, in the dark. Thus, the total time during which the sample S2 was kept at room temperature was approximately 146 hours, compared to 4.5 hours for sample S1.

3.4. Radioactivity measurements

The activity of the implanted samples was measured before the plasma etching experiment and after each etching step using an NaI(Tl) detector (2 X 2 inches), model 51B51/2, from Scionix Holland. The samples were put directly on the detector, on the same place for all the measurements. Based on data from [34], the theoretical efficiency factor of the detector for the 478 keV energy γ radiation and

for the geometry used was determined to be 50. Thus, the activity of the samples (in Bq) was calculated by multiplying the integral under the peak by 50.

3.5. Thickness measurement by ellipsometry

The thickness of the samples was measured before the plasma etching experiment and after each etching step using a Sentech SE 850 spectroscopic ellipsometer with the wavelength ranging from 350 to 850 nm.

In order to determine with precision the refractive index of the copolymer, a scratch was made in the polymer film down to the silicon substrate. The thickness of the film near the scratch was measured using a Dektak 3030 profilometer. By means of spectroscopic ellipsometer measurements, the refractive index of the copolymer film with known thickness was determined to be 1.495. This value was used for the ellipsometry thickness measurements of all samples.

For each step, two thickness measurements were performed on the selected areas (see Section 3.1) and the average was considered for the etching rate calculation. The standard deviation in the thickness measurement $u(d_i)$ was considered to be the result of the ellipsometric measurement precision (~0.5 % of all measured values d_i) and the variations in the film thickness over the selected surface (~0.5 % of the initial film thickness d_0). As a result of the isotropic plasma etching method, this variation in the film thickness over the selected region was considered to remain constant during all the plasma etching experiment.

$$u(d_i) = 0.005 \cdot d_0 + 0.005 \cdot d_i = 0.005 \cdot (d_0 + d_i) \qquad (V.1$$

where i is the thickness measurement index.

3.6. AFM

The topography and structure of the twelve samples used in the first plasma etching experiment (see Section 3.3) was studied by Atomic Force Microscopy in tapping-mode (TM-AFM). The images were recorded in air with an Autoprobe CP from Park Scientific Instruments (Sunnyvale, CA) using a 5 µm scanner. Roughness measurements were performed on 5 µm x 5µm size images.

4. Results and discussion

4.1. Etching rates

The etching rates K_{Ei} were calculated as:

$$K_{E\,i} = \frac{\Delta d_i}{t_i} = \frac{d_i - d_{i+1}}{t_i} \quad [\text{Å /s}] \qquad (\text{V.2}$$

were Δd_i is the thickness variation of the film in the given etching step i and t_i is the corresponding plasma etching time.

The uncertainties in the etching rates $u(K_{Ei})$ were calculated taking into account the uncertainties in the film thickness determination (eq. V.1) [35]:

$$\begin{aligned} u\left(K_{E\,i}\right) &= \frac{1}{\sqrt{2}\cdot t_i}\cdot\sqrt{u^2\left(d_i\right)+u^2\left(d_{i+1}\right)} = \\ &= \frac{1}{\sqrt{2}\cdot t_i}\cdot\sqrt{\left(0.005\cdot d_i + 0.005\cdot d_0\right)^2 + \left(0.005\cdot d_{i+1} + 0.005\cdot d_0\right)^2} = \\ &= \frac{0.005}{\sqrt{2}\cdot t_i}\cdot\sqrt{\left(d_i + d_0\right)^2 + \left(d_{i+1} + d_0\right)^2} \end{aligned} \qquad (\text{V.3}$$

where d_0 is the initial thickness of the film (after annealing), d_i is the thickness of the film before the etching step i and d_{i+1} is the thickness of the film after the etching step i. The factor square root of two is introduced because for each step, two measurements were made and the average value was considered.

The corresponding depth in the sample was calculated using:

$$x_i = d_0 - d_i \qquad (\text{V.4}$$

where i is the number of the etching step, and the uncertainty given by:

$$\begin{aligned} u\left(x_i\right) &= \frac{1}{\sqrt{2}}\cdot\sqrt{u^2\left(d_0\right)+u^2\left(d_i\right)} = \\ &= \frac{1}{\sqrt{2}}\cdot\sqrt{\left(0.005\cdot d_0 + 0.005\cdot d_0\right)^2 + \left(0.005\cdot d_0 + 0.005\cdot d_i\right)^2} \\ &= \frac{0.005}{\sqrt{2}}\cdot\sqrt{\left(2d_0\right)^2 + \left(d_0 + d_i\right)^2} \end{aligned} \qquad (\text{V.5}$$

The results of the etching rate estimation are presented in Figure V-4 for the two experiments with implanted samples.

It can be observed that the etching rate decrease strongly when advancing in the sample. The evolution is linear, down to around 3000 nm in both cases, followed by an increase in the etching rate for the last 2000 nm. The same behaviour was

observed in all the plasma etching experiments performed on the copolymer samples.

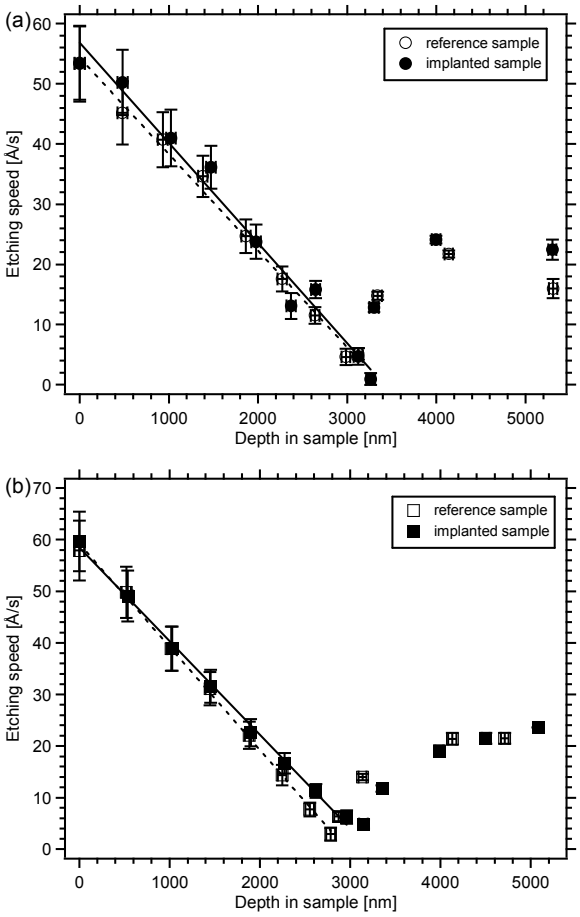

Figure V-4. Etching rate as a function of the depth in the sample. a)Implanted sample S1 with corresponding reference sample; b)Implanted sample S2 with corresponding reference sample.

It can be observed that the etching rate decrease strongly when advancing in the sample. The evolution is linear, down to around 3000 nm in both cases, followed by an increase in the etching rate for the last 2000 nm. The same behaviour was observed in all the plasma etching experiments performed on the copolymer samples.

The equations describing the linear evolution of the etching rate with the depth (in nm) in the sample are:

$$K_{E_{impl}} = 56.82 - 0.016 \cdot x \quad \text{(Å/sec)} \quad \text{(V.6}$$

$$K_{E_{ref}} = 54.36 - 0.016 \cdot x \quad \text{(Å/sec)} \quad \text{(V.7}$$

for implanted sample S1 and corresponding reference (Figure V-4a) and

$$K_{E_{impl}} = 59.24 - 0.02 \cdot x \quad \text{(Å/sec)} \quad \text{(V.8}$$

$$K_{E_{ref}} = 58.5 - 0.018 \cdot x \quad \text{(Å/sec)} \quad \text{(V.9}$$

for implanted sample S2 and corresponding reference (Figure V-4b).

The behaviour of implanted samples and of the reference one can be considered identical, in the limits of measurement uncertainties. This indicates that the plasma etching behaviour of the copolymer is not modified by the ion implantation and the processes accompanying it.

The variation of the etching speed with the etching time is presented in Figure V-5.

In the field of oxygen plasma etching of polymers, the decrease of the etching rate with etching time, when the plasma parameters are kept constant, was observed for poly(methyl methacrylate) PMMA films with initial thickness smaller than 500 nm [36]. The explanation found was that the etching rate variation is due to an increase in the glass transition temperature of the material with the decrease of the initial thickness of the film. However, as we mentioned before, this was observed only for polymer films thinner than 500 nm, value that is much lower than the sample thicknesses used in our experiments.

A possible explanation for the decrease of the etching rate of the SEPS copolymer is that the aromatic functional side groups of polystyrene have a protective role (see section 2.2.2 above); therefore, the etching speed of the polystyrene phase is much lower than the etching speed of the rubbery phase [37,38]. This may induce an accumulation of the polystyrene phase of the copolymer on the surface of the samples and, around 3000 nm, there is only polystyrene which is removed, with an etching speed of ~5 Å/s.

Due to this dissimilarity in the removal rates and the probable resulting polystyrene accumulation, the roughness of the sample increases, increasing thus the surface to be etched. This will further contribute to the decrease in the etching speed of the sample. In order to check this hypothesis, AFM examination was performed on twelve unimplanted samples and the evolution of the etching rate was compared with the results of the roughness measurements.

Another phenomenon that may influence the etching rate is the formation of a cross linked layer on the polymer surface exposed to the plasma treatment [33]. This layer would play a protective role for the underlying material.

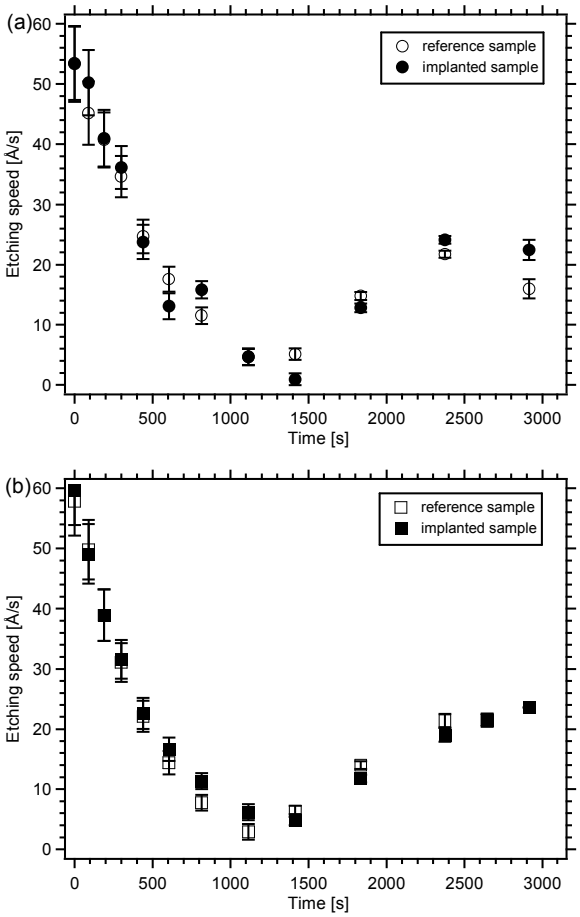

Figure V-5. Etching rate as a function of etching time: a)Implanted sample S1 with corresponding reference sample; b)Implanted sample S2 with corresponding reference sample

4.2. Roughness

As it was presented before (section 3.3 above), the modifications on the surface of twelve samples exposed to plasma etching were studied using AFM in tapping mode. The results of the roughness measurements are presented in Figure V-6a as a function of the depth in the thirteenth sample. In Figure V-6b the evolution of the etching rate for the thirteenth sample as a function of the depth in sample is presented, in order to facilitate the detection of similarities between the two curves.

In Figure V-6a it can be observed that the roughness of the samples increases with the depth in the sample, thus with the time of exposure to the plasma etching.

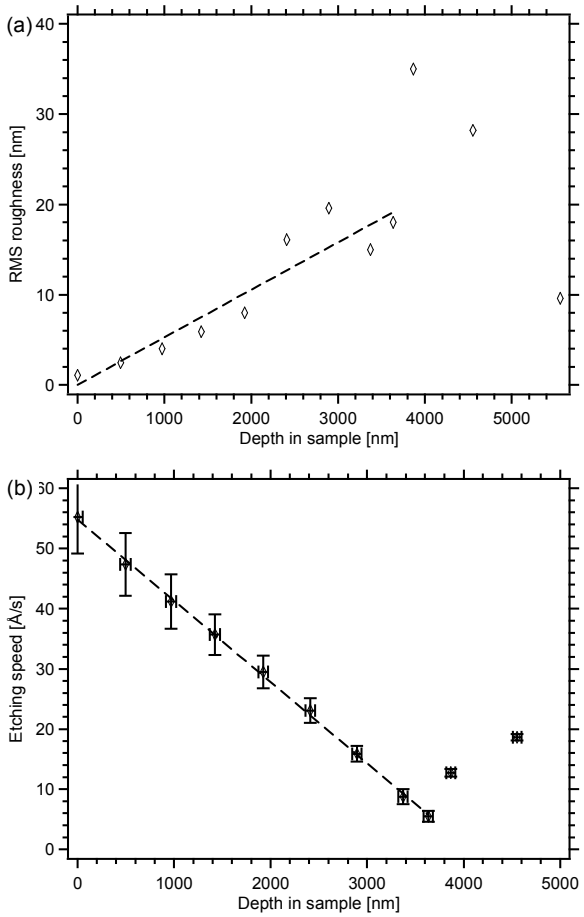

Figure V-6.a) RMS roughness measured on the etched surface (5µm x 5µm) of the sample as function of the depth; b) Etching rate as a function of the depth in the sample.

After the removal of approximately 4000 nm, the roughness suffers a strong increase, followed by a sharp decrease. A complementary behaviour can be observed in the etching speed evolution (Figure V-6b), where, after the linear decrease with the thickness of the removed material, at approximately 4000 nm, the etching speed starts to increase.

This is a clear indication that the behaviour of the etching rate is strongly related to the physico-chemical modifications occurring on the sample surface during the plasma etching process.

It has also to be noted that the roughness of the sample, even at its maximum value (35 nm) is not so large as to affect the ellipsometry thickness measurement at the corresponding sample thickness (~1700 nm).

The dramatic modifications induced by the plasma etching on the samples surfaces can also be followed in the topographic (left) and phase (right) AFM images presented in Figure V-7.

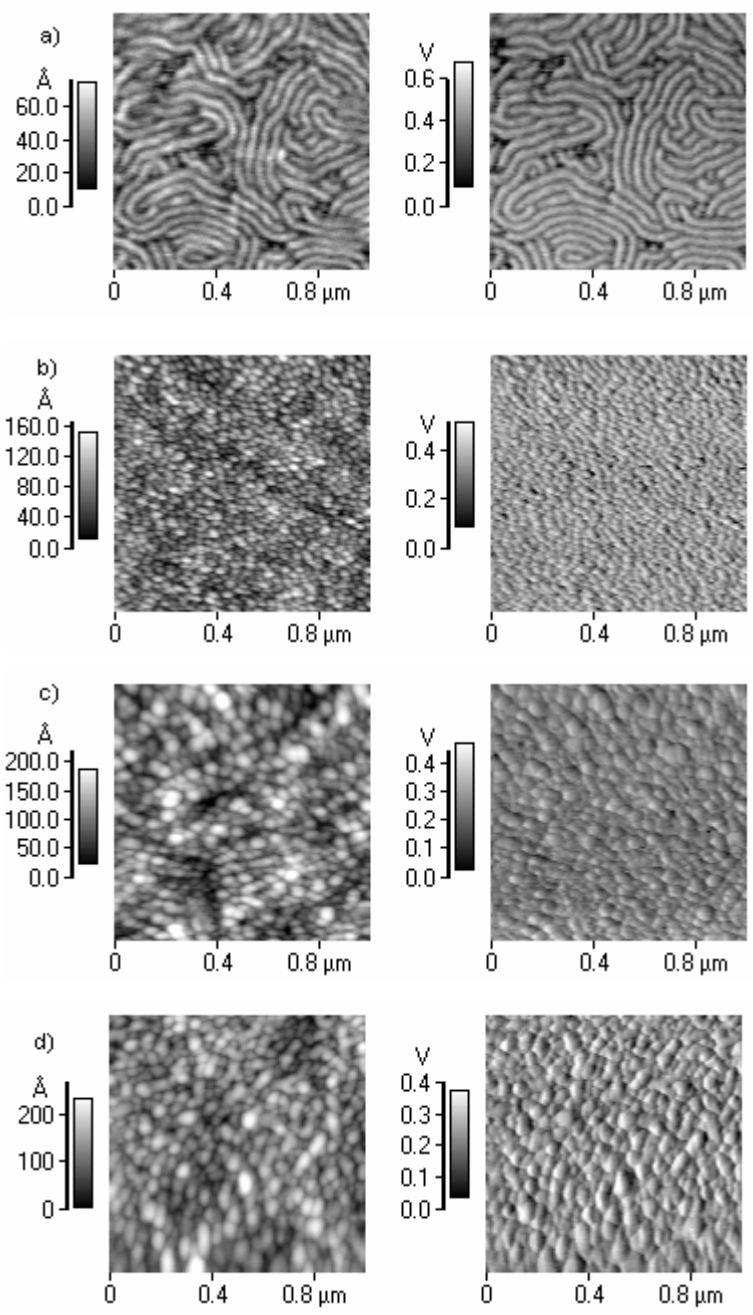

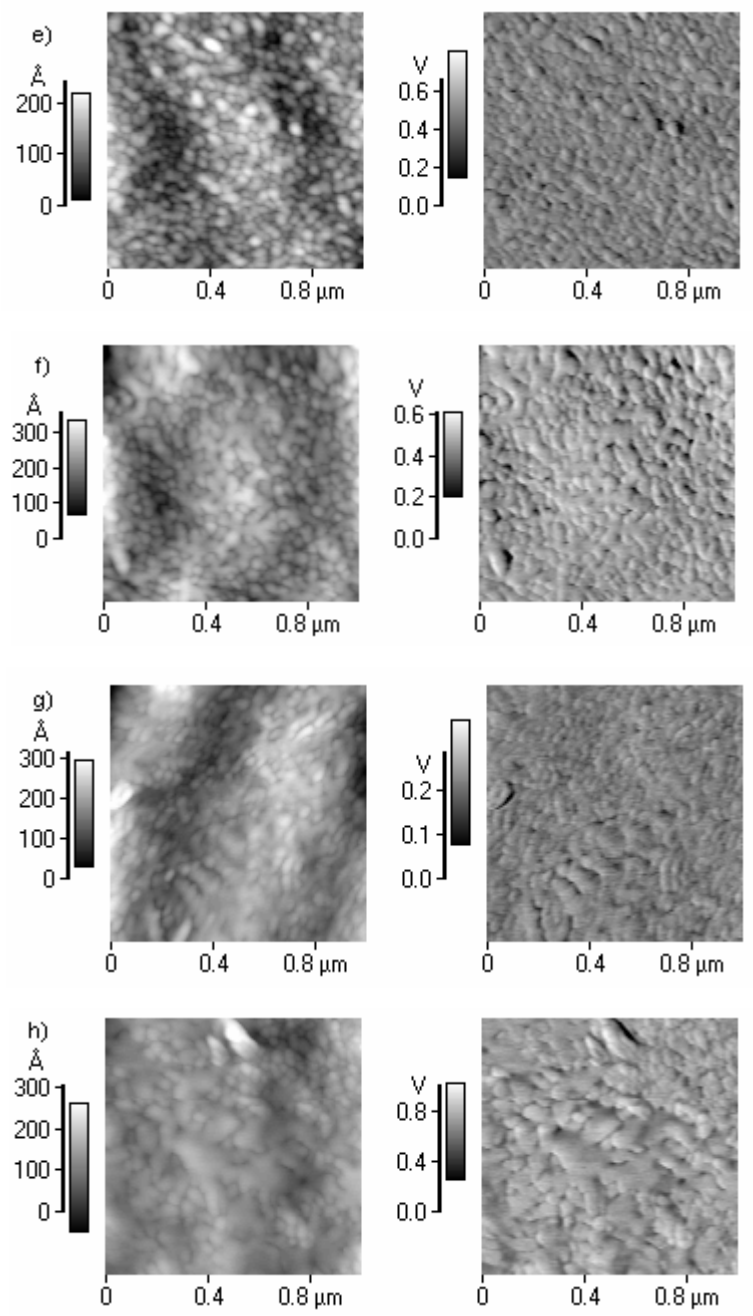
e)
Å
200
100
0
0
0.4
0.8 µm
V
0.6
0.4
0.2
0.0
0
0.4
0.8 µm
f)
Å
300
200
100
0
0
0.4
0.8 µm
V
0.6
0.4
0.2
0.0
0
0.4
0.8 µm
g)
Å
300
200
100
0
0
0.4
0.8 µm
V
0.2
0.1
0.0
0
0.4
0.8 µm
h)
Å
300
200
100
0
0
0.4
0.8 µm
V
0.8
0.4
0.0
0
0.4
0.8 µm

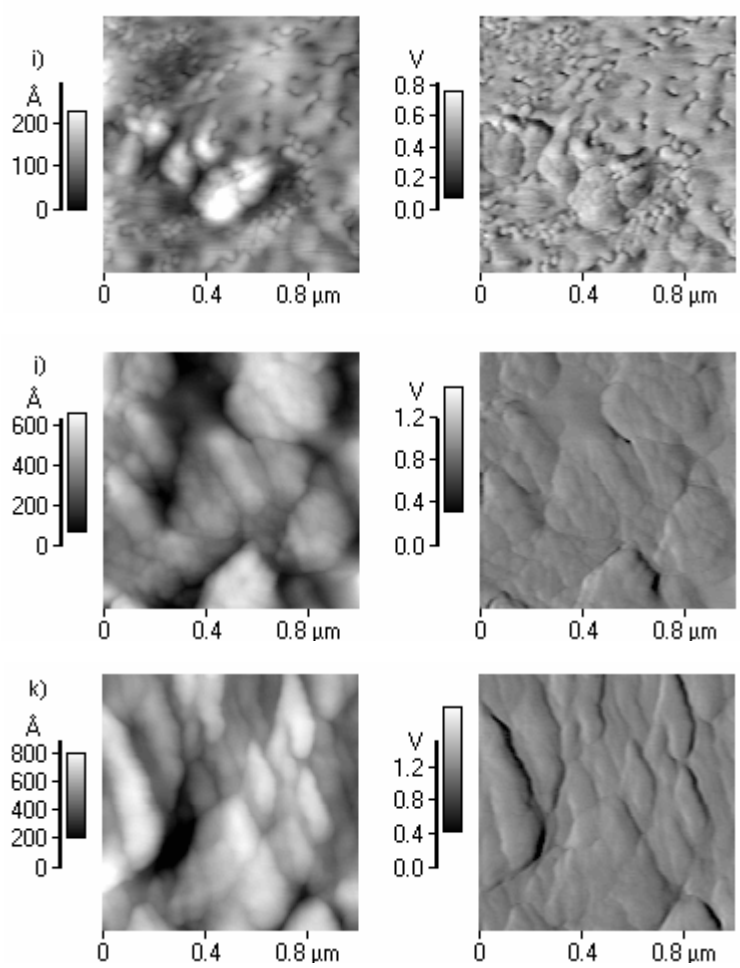

Figure V-7. AFM topographic and phase images (1 µm x 1µm) with the corresponding plasma treatment time: a) unmodified sample (0 s); b) 90 s; c) 190 s; d) 300 s; e) 440 s; f) 605 s; g) 815 s; h) 1115 s; i) 1415 s; j) 1835 s; k) 2375 s.

Even for the shortest time of plasma exposure (90 s), the morphology of the surface is changed, and the polystyrene cylinders in the rubbery matrix are no more visible (Figure V-7b). For intermediary etching times (Figure V-7c to Figure V-7e), in the topography images small spheres can be observed, but no phase separation can be detected in the phase images.

After a longer exposure time (starting with Figure V-7f), larger structures become visible in the topography images and their size continues to increase with increasing etching time. These structures could be the results of a cross linking process that is accentuated by the prolonged etching time.

Another phenomenon observed for the samples exposed to the oxygen plasma for more than 10 minutes was that the imaging with the AFM became difficult; the tip had the tendency to stick to the surface of the copolymer. In the last images (Figure V-7i and Figure V-7j), artefacts are visible, caused by the contamination of the tip by the substance on the surface. Even changing the tip after each complete scan did not improved the quality of the images; the new tip was contaminated after the first few scanning lines.

This indicates that besides etching and cross-linking, other processes occurred, and the generated degradation products (molecules of low molecular weight) accumulate on the sample surface. This phenomenon was also reported in AFM studies of oxygen plasma treated polypropylene surface [39] and polytetrafluoroethylene [40].

4.3. Diffusion of the implanted ions

The total number of implanted ions N_0 was calculated, for each sample, by taking into account the total activity A measured before the plasma treatment and the time after the implantation t:

$$N_0 = \frac{N}{\exp(-\lambda \cdot t)} = \frac{A}{\lambda \cdot \exp(-\lambda \cdot t)} \qquad (V.10$$

where N is the number of remaining ions after time t, and $\lambda = ln2/T_{1/2}$ is the decay constant (with $T_{1/2}=53.3$ *days*, the half-life of ^{7}Be). The results are presented in Table V-1.

Sample	n	±u(n)	A	±u(A)	t	N_0	±u(N_0)
	[cnts/s]	[cnts/s]	[Bq]	[Bq]	[h]		
S1	50.62	8.03	2531	401.68	54	$1.73 \cdot 10^{10}$	$2.7 \cdot 10^{9}$
S2	52.65	8.46	2632	423.149	556	$2.36 \cdot 10^{10}$	$3.8 \cdot 10^{9}$

Table V-1. Results of the total activity measurements and calculated total number of implanted ions for the two implanted samples

The corrected number of counts/s n was obtained by subtracting the background counting (without sample) n_{back} from the result measured on the sample, n_{sample}:

$$n = n_{sampl} - n_{back} \qquad (V.11$$

The uncertainties presented in Table V-1 were calculated using:

$$u(n) = \sqrt{u^2(n_{sampl}) + u^2(n_{back})} = \sqrt{\sqrt{n_{sampl}^2} + \sqrt{n_{back}^2}} = \\ = \sqrt{n_{sampl} + n_{back}} \qquad (V.12$$

$$u(A) = 50 \cdot u(n) \quad \text{(see paragraph 3.4 above)} \qquad \text{(V.13}$$

$$u(N_0) = \frac{u(N)}{\exp(-\lambda \cdot t)} = \frac{u(A)}{\lambda \cdot \exp(-\lambda \cdot t)} \qquad \text{(V.14}$$

The total numbers of implanted ions N_0, correspond to fluences of $(3.46\pm0.54)\cdot10^{10}$ ion/cm^2 for the first sample, respectively of $(4.72\pm0.76)\cdot10^{10}$ ion/cm^2 for the second one. These fluences are much lower than the lowest fluence $\sim10^{13}$ used in other studies concerning the redistribution of implanted ions in polymers.

The experimental calibration curves and theoretical one, calculated with SRIM [41], are presented in Figure V-8. Each point on the experimental curves was calculated by subtracting the background activity from the value measured on the sample. The error bars on the vertical axis were calculated using equation V.12 for each measured activity, and the ones on the horizontal axis were calculated using equation V.5.

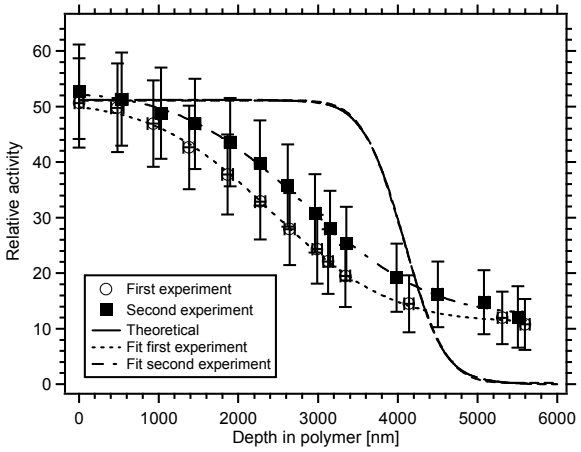

Figure V-8. Experimental and theoretic calibration curves (remaining activity after the removal of a given thickness)

Taking into consideration that the implantation profile is a Gaussian distribution, the calibration curves were fitted using the cumulative distribution function:

$$cdf(x) = a + \frac{1}{2} \cdot (b - a) \cdot \left[1 + erf\left(\frac{x - c}{\sqrt{2} \cdot d} \right) \right] \qquad \text{(V.15}$$

where the fitting parameters are: a, which is the total initial number of counts/s, b the remaining counts/s in the last layer, c indicate the implantation peak position [nm] and $2d$ is the peak width [nm] at half maximum. The error function (Gauss error function) *erf* is defined as [42]:

$$erf(x) = \frac{2}{\sqrt{\pi}} \int_0^x e^{-t^2} dt \qquad (V.16$$

The results of the fits are presented in Table V-2.

	a	b	c	d
	counts/s	counts/s	nm	nm
Theoretical (SRIM)	51.12	0.23	4079	415.6
First experiment	50.62	11.32	2424	1171.3
Second experiment	52.65	12.32	2825	1249.4

Table V-2. The results of the fitting of the two experimental and the theoretical calibration curves: a - the total initial number of counts/s, b - the remaining counts/s in the last layer, c - the implantation peak position, 2d - the peak width at half maximum.

To facilitate the illustration of these outcomes, the corresponding experimental and theoretical depth profiles are presented in Figure V-9. The experimental results were fitted using a Gaussian fitting function. The error bars were omitted in order to avoid the encumbering of the graphs.

The results presented in Table V-2 indicate that the distribution peak position shifts from a projected range of ~4000 nm to ~2400 nm for the first sample and to ~2800 nm for the second one. This phenomenon is accompanied by an important broadening of the depth profile; the peak width at half maximum is tripled. A discrepancy between theory and experiment cannot explain this large difference. With the occasion of the copolymer foils implantation experiment, it was confirmed that the simulations with SRIM could estimate with relatively high precision the position and shape of the implantation profile (see Chapter III).

Another surprising result is that the largest shift (~1600 nm) occurs for the first sample, though the time spent at room temperature was shorter (4.5 h) than for the second one (146 h). An explanation may be found in Figure V-8, where it can be observed that if the uncertainties in the results are taken into account, the differences between the two experimental curves may vanish.

However, the results indicate that the time spent at room temperature after implantation does not affect significantly the distribution profile of the ions in the copolymer. Therefore, it can be supposed that the redistribution of the implanted ions takes place during the implantation process and that an equilibrium state is reached in a short time.

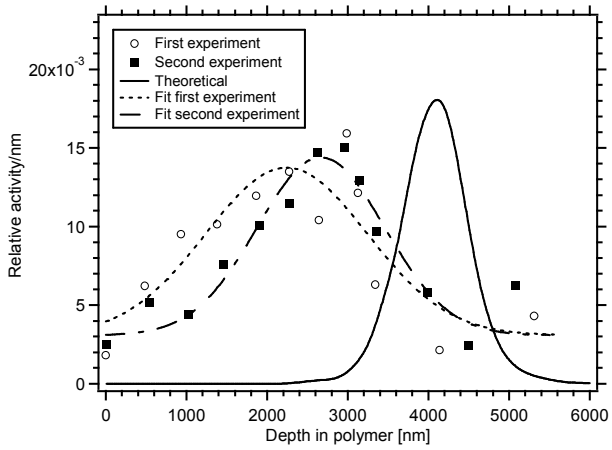

Figure V-9. Experimental and theoretical depth profiles

Heat generated at the surface due to the plasma treatment cannot be the explanation for the redistribution of the ions. The low thermal conductivity of polymers prevents the propagation of the heat in the bulk, therefore playing a protective role. It should be noted also, that already in the first removed layer of the copolymer, a small amount of radioactive ions was detected. This cannot be explained by a heat-enhanced redistribution of the ions, because this would mean that during the 90 s of the first plasma etching treatment, the ions would have to travel through a distance of approximately 3000 nm in the sample.

It has also to be taken into consideration that during the abrasive wear of materials, heat is generated at the contact surface due to the frictional forces. If the heat generated during the plasma treatment affects the comportment of the implanted ions, enhancing the redistribution, the same behaviour would be observed during an abrasive wear test.

A similar behaviour was observed for 100 keV energy boron ions implanted at high fluences ($5 \cdot 10^{16}$ ion/cm^2) in polyethylene, polyamide and cellulose by means of neutron depth profiling techniques [43]. The depth profiles presented a maximum, shifted from ~500 nm (theoretical prediction with SRIM) to ~300 nm for all materials.

In another study, the redistribution of ^{6}Li ions with 100 keV energy, implanted in polystyrene films at fluences between 10^{13} and 10^{14} ion/cm^2, was investigated by means of neutron depth profiling technique [44]. The implantation profiles resulted as a superposition of two components, a peaked one around 120 nm (corresponding to the theoretical prediction), and a flat one that extended deep into the bulk polymer. For the low-fluence implanted sample, the peaked component vanished completely.

For 150 keV ^{6}Li implanted in polypropylene foil at $5 \cdot 10^{13}$ and 10^{14} ion/cm^2, studied by neutron depth profiling the same behaviour was observed [45]. The distribution

peak shifted from approximately 1.2 μm (mean projected range) to approximately 0.6 μm, accompanied by an important broadening, but for the lowest fluence implanted (10^{13} ion/cm^2), the redistribution peak position remained almost unchanged compared to projections, with only a minor broadening. The implanted ^{6}Li was able of diffusing through both the pristine and irradiated polymer, though the diffusional speed in the radiation-damaged material exceeds the one in the pristine material by at least an order of magnitude.

These studies indicated as explanation for the seemingly contradictory results that the irradiation with light ions promotes two counteracting effects, radiation enhanced diffusion (due to excess free volume) and radiation retarded diffusion (due to trapping, detrapping processes at the defects), and it is the sum of both that determines the experimentally observed effect (see also Chapter II, Section 3.2). The dominant effect seems to be dependent on the ion energy, fluence and implanted material properties. As we concluded in Chapter II, there is so far no universal theory able to explain all the experimental results. This implies that the redistribution of the ions should be carefully evaluated for each implantation circumstances.

With only two measurements performed, it is difficult to formulate justifications for the results obtained. From the point of view of our project, the main objective was to check if the radioactive ions redistribute or not during or after the implantation, and the conclusion is that, unfortunately, they do so extremely rapidly.

5. Conclusion

As we mentioned in the introduction of this chapter, the main aspect of the radioactive ion implantation wear measuring method was examined, namely, whether if the implantation profile remains unchanged or the ions redistribute during or after the implantation.

In order to achieve this goal, a new method was used, that implied the use of plasma etching technique in order to remove layers of polymer and measuring the remaining activity after each step. This was necessary because no existing method is able to detect light ions as ^{7}Be, at low fluences (10^{10} ion/cm^2 order of magnitude) and large implantation depths (~4000 nm), conditions that were selected for the experiments.

The same material was used as in all previous experiments, a SEPS poly(styrene-*block*-(ethylene-*co*-propylene)-*block*-styrene) tri-block copolymer. The copolymer nature of the material determined some complications during the plasma etching; more specifically, the etching rate of the material decreased with the increase of the etching time. The large difference in the etching speed of the two components, polystyrene and ethylene-propylene rubber induced also an increase in the roughness of the sample surface, studied by AFM.

The plasma etching of the two implanted samples allowed us to obtain the calibration curves, thus, the remaining activity after each step. These calibration

curves revealed that a redistribution of the implanted ions took place during the implantation process.

However, the redistribution takes place in a very short time, therefore, a steady state is reached quickly. After this short redistribution stage, the depth profile and the corresponding calibration curve remain unchanged even for longer time (a week in the conditions of our experiments).

This indicates that polymer wear measurements performed by means of radioactive ions implantation are still possible, if a special methodology is employed. Namely, together with the implantation of the actual sample (the sample to be exposed to the wear test), a reference sample has to be implanted with ^{7}Be ions. Of course, the reference sample has to be carefully prepared; if possible, a duplicate of the actual sample can be used. Prior to the wear measuring experiments on the actual sample, this reference sample can be used to establish the calibration curve, using the plasma etching method.

By the experiments presented in this chapter we also proved that diffusion studies in polymers implanted with radioactive ions at very low fluences (~10^{10} ion/cm^2) and large implantation ranges (up to 4000 nm or more) can be performed using plasma etching techniques. By using adequate background shielding and high performance detectors during the activity measurements, the precision of the results could be improved and lower fluences (<10^{10} ion/cm^2) could also be used.

It remains however difficult to determine the mechanisms responsible for the fast redistribution of the ions. Complementary experiments are clearly required here. They could not be performed within the frame of this thesis due to the high cost and limited availability of the ^{7}Be beam. Given the limited practical interest of performing such a costly study with respect to the development of the radioactive wear measurement technique, investment into further study is not practically relevant. Nevertheless, basic studies on different polymers and different implantation/storage conditions of the samples could be certainly be performed by the method we have developed, which could contribute to a better understanding of the motions of light ions in polymers of varying structure. Furthermore, by choosing different plasma parameters (different gas, for example) it may be possible to further reduce the selectivity of the plasma etching process, therefore, copolymer materials could also be studied with less uncertainty.

6. References

1. J.G.A. Terlingen, Introduction of functional groups at polymer surfaces by glow discharge techniques; University of Twente: Enschede, The Netherlands, 1993.

2. H.V. Jansen, Plasma Etching in Microtechnology; University of Twente: Enschede, The Netherlands, 1996.

3. M.J. Madou, M. Madou, Fundamentals of microfabrication: The science of miniaturization, CRC Press, 1997, p.77.

4. F.D. Egitto, L.J. Matienzo, Plasma modification of polymer surfaces for adhesion improvement, IBM J. Res. Develop. 38 (1994) 423.

5. B.R. Rogers, T.S. Cale, Plasma processes in microelectronic device manufacturing, Vacuum 65 (2002) 267.

6. A.C. Forza, M. Moisan, M.R. Wertheimer, Vacuum ultraviolet to visible emission from hydrogen plasma: Effect of excitation frequency, J. Appl. Phys. 88 (2000) 20.

7. R.M. France, R.D. Short, Plasma treatment of polymers : effects of energy transfer from an argon plasma on the surface chemistry of poly(styrene), low density poly(ethylene), poly(propylene) and poly(ethylene terephthalate), J. Chem. Soc., Faraday Trans., 93 (1997) 3173.

8. N. Morosoff, B. Crist, M. Bumgarner, T. Hsu, H. Yasuda, Free radicals resulting from plasma polymerization and plasma treatment, J. Macromol. Sci.- Chem, A10 (1976) 451.

9. J. Behnisch, J. Friedrich, H. Zimmermann, Topokinetics of the polyene formation in pvc films during treatment with non-oxidative plasma, Acta Polymerica, 42 (1991) 51.

10. B. Ranby, J.F. Rabek, Photodegradation, Photooxidation and Photostabilization of Polymers, Principles and Application, John Wiley, New York, 1975.

11. M. Hudis, L.E. Prescott, Surface crosslinking of polyethylene produced by the ultraviolet radiation from a hydrogen glow discharge, Polym. Lett. 10 (1972) 179.

12. J.C. Ashley, Interaction of Low-Energy Electrons With Condensed Matter: Stopping Powers and Inelastic Mean Free Paths From Optical Data, J. Electron Spectrosc. Relat. Phenom.,46 (1988) 199.

13. A. M. Wrobel , B. Lamontagne, M. R. Wertheimer, Large-area microwave and Radiofrequency plasma etching of polymers, plasma chemistry and plasma processing, 8 (1988) 315.

14. F.D. Egitto, Plasma etching and modification of organic polymers, Pure & Appl. Chem., 62 (1990) 1699.

15. S.J. Moss, A.M. Jolly, B.J. Tighe, Plasma oxidation of polymers, J. Plasma Chem. Plasma Process., 6 (1986) 401.

16. V.V. Rybkin, A.B. Bessarab, E.V. Kuvaldina, A.I. Maximov, V.A. Titov, Self-consistent analysis of low temperature oxygen plasma and processes of its interaction with some polymer materials, Pure & Appl. Chem., 68 (1996) 1041.

17. I.C. Plumb, K.R. Ryan, A model of the chemical processes occurring in CH_4/O_2 discharges used in plasma etching, J. Plasma Chem. Plasma Process., 6 (1986) 205.

18. M.J. Kushner, A kinetic study of the plasma etching process. II. Probe measurements of electron properties in an rf plasma-etching reactor, J. Appl. Phys. 53 (1982) 2939.

19. J.M. Cook, J.J. Hannon, B.W. Benson, EPR studies of the effects of impurity gases on the oxidation of organics, Proc. 6th Internat. Symp. on Plasma Chem., M.I. Boulos, R.J. Munz, Eds., IUPAC, Montreal, 1983, p. 616.

20. M.C. Coen, R. Lehmann, P. Groening, L. Schlapbach, Modification of the micro-and nanotopography of several polymers by plasma treatments, J. Appl. Surf. Sci., 207 (2003) 276.

21. E. Bonaccurso, K. Graf, Nanostructuring effect of plasma and solvent treatment on polystyrene, Langmuir, 20 (2004) 11183.

22. N. Sprang, D. Theirich, J. Engemann, Plasma and ion beam surface treatment of polyethylene, Surf. and Coat. Technol., 74-75 (1995) 689.

23. A. Durandet, O. Joubert, J. Pelletier, M.J. Pichot, Effects of ion bombardment and chemical reaction on wafer temperature during plasma etching, J. Appl. Phys., 67 (1990) 3862.

24. K. Richter, M. Orfert, K. Drescher, Anisotropic patterning of copper-laminated polyimide foils by plasma etching, Surf. Coat. Technol. 97 (1997) 481.

25. S.J. Moss, Polymer degradation ion reactive-gas plasmas, J. Polym. Degrad. Stab., 17 (1987) 205.

26. S.R. Cain, F.D. Egitto, F. Emmi, Relation of polymer structure to plasma etching behaviour: Role of atomic fluorine, J. Vac. Sci. Technol. A, 5 (1987) 1578.

27. G.N. Taylor, T.M. Wolf, Oxygen plasma removal of thin polymer films, Polym. Eng. Sci., 20 (1980) 1087.

28. O. Joubert, P. Paniez, M. Pons, J. Pelletier, Polymer behaviour under plasma etching : Influence of physical properties on kinetics and durability, J. Appl. Phys., 70 (1991) 977.

29. S. Herbert, D.M. Shinozaki, R.J. Collacott, Fine-scale morphology of ultraviolet-ozone etched polyethylene, J. Mater. Sci., 31 (1996) 4655.

30. B.D. Beake, J.S.G. Ling, G.J. Leggett, Scanning force microscopy investigation of poly(ethylene terephtalate) modified by argon plasma treatment, J. Mater. Chem., 8 (1998) 1735.

31. Ch.C. Dupont-Gillain, Y. Adriaensen, S. Derclaye, P.G. Rouxhet, Plasma-oxidizied polystyrene: wetting properties and surface reconstruction, Langmuir, 16 (2000) 8194.

32. M.C. Coen, G. Dietler, S. Kasas, P. Groning, AFM measurements of the topography and the roughness of ECR plasma treated polypropylene, J. Appl. Surf. Sci., 103 (1996) 27.

33. R. Mahlberg, H.E.M. Niemi, F.S. Denes, R.M. Rowell, Application of AFM on the adhesion studies of oxygen-plasma-treated polypropylene and lignocellulosics, Langmuir, 15 (1999) 2985.

34. G.F. Knoll, Radiation detection and measurement, J. Wiley and Sons, New York, 2002.

35. Multi-agency radiological laboratory analytical protocols manual, Vol. III, National Technical Information Service (NTIS), www.ntis.gov.

36. N. Voudras, A.G. Boudouvis, E. Gogolides, Plasma etch rate measurements of thin PMMA films and correlation with the glass transition temperature, J. of Phys.: Conf. Series, 10 (2005) 405.

37. F.S. Denes, S. Manolache, Macromolecular plasma-chemistry: an emerging field of polymer science, Prog. Polym. Sci., 29 (2004) 815.

38. M. Park, C. Harrison, P.M. Chaikin, R.A. Register, D.H. Adamson, Block copolymer lithography: periodic arrays of ~10^{11} moles in 1 square centimetre, Science, 276 (1997) 1401.

39. R. Mahlberg, H.E.M. Niemi, F. Denes, R.M. Rowell, Effect of oxygen and hexamethyldisiloxane plasma on morphology, wettability and adhesion properties of polypropylene and lignocellulosics, Int. J. Adhes. 62 Adhes. 18 (1998) 283.

40. M.E. Ryan, J.P.S. Badyal, Surface structuring of PTFE film using nonequilibrum plasmas, Macromolecules, 28 (1995) 1377.

41. www.srim.org

42. M. Abramowitz, I. A. Stegun, eds. Handbook of Mathematical Functions with Formulas, Graphs, and Mathematical Tables, New York: Dover, 1972.

43. V.N. Popok, V.B. Odzhaev, I.P. Kozlov, I.I. Azarko, I.A. Karpovich, D.V. Sviridov, Ion beam effects in polymer films: structure evolution of the implanted layer, Nucl. Instr. and Meth. in Phys. Res. B 129 (1997) 60.

44. M.R.F. Soares, P. Alegaonkar, M. Behar, D. Fink, M. Muller, $^{6}Li^{+}$ ion implantation into polystyrene, Nucl. Instr. and Meth. in Phys. Res. B 218 (2004) 300.

45. D. Fink, M. Behar, J. Kaschny, R. Klett, L.T. Chadderton, V. Hnatowicz, J. Vacik, L. Wang, On the redistribution of $^{6}Li^{+}$ ions implanted into polypropylene foils, Appl. Phys. A, 62 (1996) 359.

Conclusions and perspectives

The thesis has focused on main aspects of the radioactive ion implantation (RII) wear measuring technique, as the only wear measuring method based on radionuclide techniques that is suitable for polymeric materials, as suggested by a review of the literature presented in section 3 of the Chapter 1. This bibliographic research indicated also that the use of direct implantation of radioactive ^{7}Be ions would reduce the risks of inducing unwanted material modification in sensitive materials, as polymers.

One main objective of our research was to confirm experimentally these theoretical expectations; therefore, samples of a SEPS poly(styrene-*block*-(ethylene-*co*-propylene)-*block*-styrene) tri-block copolymer, presented in Chapter 1, section 4.3, and a copolymer containing unsaturated bonds SIS poly(styrene-*block*-isoprene-*block*-styrene), a tri-block copolymer, were implanted with ^{7}Be, ^{7}Li and Kr ions. Thereafter, the samples were characterised by means of optical microscopy, Atomic Force Microscopy (AFM), Fourier Transform Infrared Spectroscopy (FT-IR) and X-ray Photoelectron Spectroscopy (XPS).

As it was expected, the results of the characterisation techniques, presented in Chapter 4, indicate that the ^{7}Li and ^{7}Be ion implantation, in the selected conditions, does not induce significant modifications in the materials, even in the more sensitive SIS copolymer.

Another important conclusion of the physico-chemical characterisation presented in Chapter 4 is that the modifications observed in the ^{7}Be implanted copolymer samples are induced by the combined effect of the ion implantation and the γ and X-rays emitted by the radioactive ions, this part of the degradation being relatively important.

On the contrary, in the case of Kr ions implantation, the samples were strongly modified, up to the level that new material layer (or layers) was formed. Complex patterns with microscopic features (waves) are formed spontaneously on the samples surface due to the heterogeneities induced by the irradiation. In our experiments, no preferential direction of the wrinkles was observed, apart from the transition region between the implanted and unimplanted areas of the samples. We consider that by carefully selecting the implantation conditions (ion fluence and energy, shape of implantation mask opening) a better control of the surface structure (wavelength, amplitude and pattern of the waves) could be obtained [1-5]. This could offer the opportunity to obtain in a simple and rapid way wavy structures that can function also as diffraction gratings, pressure sensors, or in areas as biology, nano- and microfabrication [6]. This wrinkling of polymer surfaces under ion bombardment

has recently been proposed for the formation of a “stiff skin”, with protecting role on polymeric substrates [7].

Another objective of the thesis was to verify whether it is possible to predict the experimental implantation profile by means of simulations, which would simplify considerably the wear measurement experiments. Therefore, Chapter III presented the implantation of ^{7}Be ions with a particular energy distribution in a stack of ten copolymer foils.

The evaluation of the calculated implantation profile and calibration curve, obtained with the SRIM software and the experimental ones, determined by means of activity measurements indicated the possibility to predict the results of the implantation.

Experimental values for the stopping power of ^{7}Be ions in aluminium were also determined, by means of transmission techniques, in the 500-1500 keV energy interval, and the results are presented in Chapter III. The results are comparable to other experimental determinations performed before.

Our third objective was to check whether if the implantation profile remains unchanged or the ions redistribute during or after the implantation, because, in order to have the same calibration curve during the wear measurement, the implanted radioactive ions have to remain at their implantation place during the whole test.

No existing method is able to detect light elements (Li, Be, B) implanted in polymer targets at low fluences ($\leq 10^{12}$ ion/cm^2 order of magnitude) with implantation depths of a few μm. From the point-of-view of radioactive ions implantation for wear measurement, where the fluences are kept as low as possible (10^{10}-10^{11} cm^{-1}) in order to avoid material degradation and for radioprotection reasons, this value is much too high. Therefore, a new method was developed, which implied the use of plasma etching technique in order to remove layers of polymer and measuring the remaining activity after each step.

The experimental calibration curves obtained with this occasion revealed that a redistribution of the implanted ions took place during the implantation process.

Therefore, it could be concluded that polymer material wear measurements performed by means of radioactive ions implantation are not reliable; the distribution of light ions in the material changes during the implantation; as for heavy ions, the material is strongly modified by the implantation.

However, an important observation made during the experiments with light ions presented in Chapter V is that the time spent at room temperature after implantation does not affect significantly the distribution profile of the ions in the copolymer. Therefore, it was concluded that after the short redistribution stage, the distribution profile and the corresponding calibration curve remain unchanged even for a long time (a week in the conditions of our experiments). This characteristic feature could be used to develop the radioactive ion implantation wear measuring method for polymers, by using a special methodology. Namely, together with the implantation of the actual sample (the sample used for the wear measurement test), in identical

conditions, a reference sample should be also implanted with the radioactive ions. An important aspect of the methodology should be the preparation of the reference sample; for example, a duplicate of the actual sample could be used. This reference sample could be used to establish the calibration curve, by using the plasma etching method developed by us. With a known calibration curve, the wear test can then be performed and a precise measurement can be performed.

Moreover, in time, a database of calibration curves could be built-up, for different materials, with different implantation conditions, depending on the wear test requirements. This would reduce the time and the budget spent with each individual experiment. Even more, a large database of calibration curves could be used to perform statistical calculations, allowing to compute theoretically other calibration curves, without the need of performing all the experiments.

Hence, the possibility to perform reliable wear measurements on polymers is still open, even in the more complex cases, where more than one type of wear are acting simultaneously, as the one discussed in the introduction of the present thesis, weathering of organic coating or the contact motion of two solids.

However, the price of an implantation is still high, due to the complex preparations required to obtain a stable ^{7}Be beam, and this should also be considered when planning a project. Meanwhile, if the developments in the research related to the production and acceleration of ^{7}Be beams continue, lower implantation costs could be obtained and the method could become more accessible.

Nevertheless, the experiments presented in Chapter V proved that diffusion studies in polymers implanted with radioactive ions in conditions that were beyond the detection limits of the existing experimental techniques (very low fluencies and large implantation ranges) become possible using plasma etching techniques.

Therefore, basic studies on different polymers and different implantation/storage conditions of the samples could be certainly be performed by the method we have developed, which could contribute to a better understanding of the motions of light ions in polymers of varying structure.

---

1. J. Groenewold, Wrinkling of plates coupled with soft elastic media, Physica A 298 (2001) 32-45

2. N. Bowden, W. T. S. Huck, K. E. Paul, G. M. Whitesides, The controlled formation of ordered, sinusoidal structures by plasma oxidation of an elastomeric polymer, Appl. Phys. Let. 75 (1999) 2557.

3. K. M. Crosby, R. M. Bradley, Pattern formation during delamination and buckling of thin films, Phys. Rev. E, Rapid Com. 59 (1999) 2542.

4. K. Y. Suh, H. H. Lee, Dynamic instability of strongly confined thin polymer films in spinodal dewetting, Phys. Rev. Let. 87 (2001) 135502.

5. P. J. Yoo, H. H. Lee, Evolution of a stress-driven pattern in thin bilayer films: spinodal wrinkling, Phys. Rev. Let. 91 (2003) 154502.

6. W.T.S. Huck, N. Bowden, P. Onck, T. Pardoen, J. W. Hutchinson, G. M. Whitesides, Ordering of spontaneously formed buckles on planar surfaces, Langmuir 16 (2000) 3497.

7. M-W. Moon, S. H. Lee, J-Y. Sun, K. H. Oh, A. Vaziri, J. W. Hutchinson, Wrinkled hard skins on polymers created by focused ion beam, Proc. Nat. Acad. Sc. of U.S.A, 104 (2007) 1130.

Annexe A
Ion implantation experiments

The implantation of the samples was the result of a successful collaboration with the Centre de Recherches du Cyclotron (CRC), Université catholique de Louvain (UCL).

At the Louvain-la-Neuve radioactive beam facility most beams are produced using the Isotope Separation OnLine (ISOL) technique [1]. However, this on-line method is less suitable for metallic or very reactive elements because these elements do not diffuse out of the target or they immediately condense in the transfer tube from target to ion source [2].

There are two different techniques to avoid these problems: by manipulating the chemistry in the target or by using semi-online or even off-line methods. Because of the long half-life (53 days) of the ^{7}Be, this isotope is an ideal candidate for off-line production.

The ^{7}Be is produced by bombarding a metallic Li target with 27.5 MeV protons using the ^{7}Li(p,n)^{7}Be reaction. The target consists of a water-cooled molybdenum crucible, filled with about 2 g of lithium.

The ^{7}Be is extracted from the target, purified chemically, and then deposited on an aluminum sputtering electrode, which is placed in the Electron Cyclotron Resonance (ECR) ion source.[3].

The electrode is polarised negatively with several hundred volts so the ions of the source plasma are attracted to the electrode and sputter the activity in the source chamber [4,5]. The sputtering rate is determined by the sputtering voltage and by the proximity of the plasma to the electrode, which can be changed by moving the electrode in the source and/or by changing the magnetic field in the injection solenoid.

Because of the small quantities of ^{7}Be available (<100 ng), a heated plasma chamber is used, which allows the use of “on-line chemistry in the source” to effectively recycle the material deposited on the plasma chamber wall [6].

The ^{7}Be extracted from the ECR source is post-accelerated using the CYCLONE110 cyclotron. The stable contaminant beams produced in the ion source (14N2+, 7Li1+, with the same m/q) are successively used as pilot beams to tune the machine and beam transport line for $^{7}Be^{1+}$.

The beam purification is achieved by tuning the cyclotron as a radiofrequency mass separator. Because the m/q difference between $^{14}N^{2+}$ and $^{7}Be^{1+}$ is $2 \cdot 10^{-3}$, these beams are completely separated at the exit of the accelerator. However, In the case of 7Li1+ and $^{7}Be^{1+}$, the difference is only $1.4 \cdot 10^{-4}$ and the lithium contamination is not completely suppressed. To remove this residual beam, an additional stripper foil located at the accelerator is used to strip the ^{7}Be to the 4+ charge state. Because the ^{7}Li can only be stripped to the 3+ charge state, an analysing magnet can separate the two beams [2].

In this way, high purity post-accelerated ^{7}Be beams with intensities of up to 30 pA or approximately $5 \cdot 10^{7}$ particles per second (4+ charge state) at the implantation target position were obtained .

---

1. F. Vanderbist, P. Leleux, C. Angulp, E. Casarejos, M. Couder, M. Loiselet, G. Ryckewaert, P. Descouvemont, M. Aliotta, T. davinson, Z. Liu, P.J. Woods, A first experimental approach to the $^{15}O + \alpha$ elastic scattering, Eur. Phys. J. A 27, (2006) 183

2. M. Gaelens, M. Cogneau, M. Loiselet, G. Ryckewaert, Post acceleration of ^{7}Be at the Louvain-la-Neuve radioactive ion beam facility, Nucl. Instr. and Meth. in Phys. Res. B 204 (2003) 48.

3. M. Gaelens, M. Loiselet, G. Ryckewaert, development of a Be-7 beam : Techniques for the ionization of the radioactive metallic elements, Rev. Sci. Instr. V 75 (2004) 1630.

4. C. Barue, S. Biri, S. Cherkani-Hassani, M. Gaelens, M. Loiselet, G. Ryckewaert, Electron cyclotron resonance ion source developments at Louvain-la Neuve, Rev. Sci. Instr. V 69 (1998) 764.

5. G. Ryckewaert, J.M. Colson, M. Gaelens, M. Loiselet, N. Postiau, Recent results from the Louvain-la-Neuve RIB-facility, Nuclear Physics A 701 (2002) 323c.

6. M. Gaelens, M. Loiselet, G. Ryckewaert, ECR ion sources and rare isotope beams at Louvain-la-Neuve, Rev. Sc. Instrum. 73 (2002) 714.

Annexe B
Correcting Fourier Transform Infrared Spectroscopy (FT-IR) spectra

Polymer film on silicon substrate - Fourier Transform Infrared Spectroscopy in Reflection mode

Our polymer film on silicon substrate represents a two-layer system in air, with three interfaces. Figure B-1 presents the reflection and transmission suffered by the infrared light beam at the air-polymer and polymer-substrate interfaces.

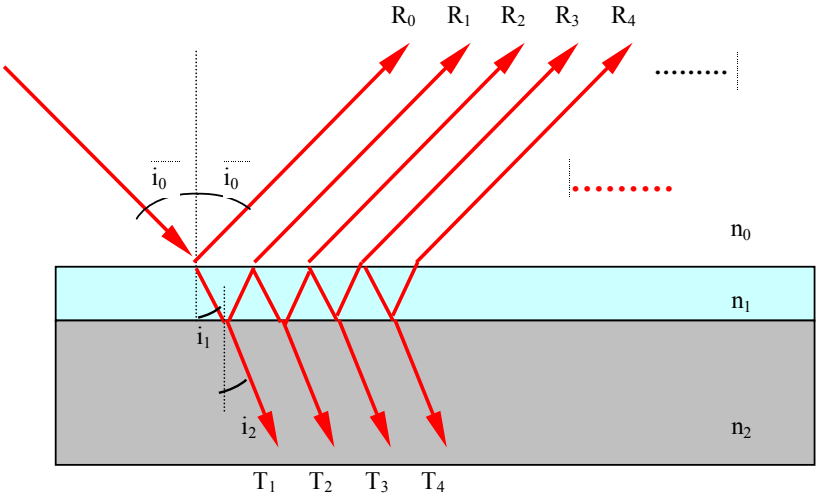

Figure B-1. Reflection and transmission of light in the case of two-layer system

The silicon-air interface is not taken into account. There are two reasons for this. Firstly, the silicon substrate has a thickness of approximately 500 µm, so the intensity of infrared light reflected at this interface, which has to traverse two times this layer, is strongly reduced. The second reason is that the unpolished surface diffuses the light in all direction, therefore the intensity of the beam reflected in the same direction as R_0, R_1, R_2… will be very low [1].

Therefore, the resultant reflected light returning in the first medium, air, is considered to be made up of the light reflected directly from the first interface plus all of the transmissions from the light approaching the first interface from the second

medium. The addition by interference of this infinite series of partial waves leads to the resultant wave. In this case, the plane parallel plate act as a Fabry-Perot interferometer and multiple-beam interference fringes are produced [2,3].

The presence of the interference fringes obstructs the interpretation of the infrared spectra. We had to find a solution to remove the fringes. A procedure was written in order to simulate the interference phenomena, without the absorption peaks. The procedure was based on the theory of reflection and transmission for a thin film on top of a thick substrate system [4]. At the end, the simulated spectrum was subtracted from the experimental one and a relatively "good" spectrum was obtained.

In the following, theoretical aspects that served as basis for the procedure are presented.

The fraction of the intensity of incident light that is reflected from the air, polymer film, silicon substrate system is given by the reflectance R_{012}, the fraction refracted by the transmittance T_{012} and the fraction absorbed in the polymer film is given by the absorbance A_{012}.

Energy conservation requires:

$$R_{012} + T_{012} + A_{012} = 1 \qquad (B.1$$

In our case, we are interested in the simulated baseline of the infrared spectrum, therefore, the absorption can be neglected and the relation become:

$$R_{012} + T_{012} = 1 \qquad (B.2$$

where:

$$R_{012} = R_0 + R_1 + R_2 + R_3 + ... \qquad (B.3$$

$$T_{012} = T_1 + T_2 + T_3 + ... \qquad (B.4$$

The parameter that characterises the interaction of light with a material is the complex index of refraction:

$$N = n - ik \qquad (B.5$$

where n stands for the real and k for the imaginary part of the refractive index.

In Figure B-1 n_0, n_1 and n_2 represent the real part of the refractive indexes of air, polymer film and substrate, respectively. i_0, i_1 and i_2 are the angles between the surface normal and the incident and the transmitted beams.

When a light beam meets the interface between two mediums, the plane of incidence can be defined as the plan that contains both the incoming beam and the outgoing beam as well as the normal to the surface. The field vector of the light beam, E can

be split into 2 components E_p and E_s which are polarised parallel (p) and perpendicular (s) to the plane of incidence [5].

The Fresnel coefficients are defined as the ratios of the amplitudes of the reflected and transmitted beams to the corresponding amplitude of the incident beam:

$$r_p = \frac{E_{p,r}}{E_{p,0}} \quad \text{(B.6}$$

$$r_s = \frac{E_{s,r}}{E_{s,0}} \quad \text{(B.7}$$

$$t_p = \frac{E_{p,t}}{E_{p,0}} \quad \text{(B.8}$$

$$t_s = \frac{E_{s,t}}{E_{s,0}} \quad \text{(B.9}$$

where the subscripts *p* and *s* denote the parallel and perpendicular components.

At the first, air-polymer interface, the Fresnel coefficients are given by [6]:

$$r_{01p} = \frac{N_1 \cos i_0 - N_0 \cos i_1}{N_1 \cos i_0 + N_0 \cos i_1} \quad \text{(B.10}$$

$$r_{01s} = \frac{N_0 \cos i_0 - N_1 \cos i_1}{N_0 \cos i_0 + N_1 \cos i_1} \quad \text{(B.11}$$

$$t_{01p} = \frac{2N_0 \cos i_0}{N_1 \cos i_0 + N_0 \cos i_1} \quad \text{(B.12}$$

$$t_{01s} = \frac{2N_0 \cos i_0}{N_0 \cos i_0 + N_1 \cos i_1} \quad \text{(B.13}$$

where the subscript *0* refers to air and subscript *1* refers to polymer.

At the first interface, the relation between i_0 and i_1 is given by Snell's law:

$$N_0 \sin i_0 = N_1 \sin i_1 \quad \text{(B.14}$$

At the second, polymer-silicon substrate interface, the corresponding Fresnel coefficients are:

$$r_{12p} = \frac{N_2 \cos i_1 - N_1 \cos i_2}{N_2 \cos i_1 + N_1 \cos i_2} \quad \text{(B.15}$$

$$r_{12s} = \frac{N_1 \cos i_1 - N_2 \cos i_2}{N_1 \cos i_1 + N_2 \cos i_2} \quad (B.16$$

$$t_{12p} = \frac{2N_1 \cos i_1}{N_2 \cos i_1 + N_1 \cos i_2} \quad (B.17$$

$$t_{12s} = \frac{2N_1 \cos i_1}{N_1 \cos i_1 + N_2 \cos i_2} \quad (B.18$$

and Snell's law can be written as:

$$N_1 \sin i_1 = N_2 \sin i_2 \quad (B.19$$

where the subscript *2* refers to silicon substrate.

The ratio of the amplitude of the resultant reflected wave to the amplitude of the incident wave is given by the total reflection coefficients [7,8]:

$$r_{012p} = \frac{r_{01p} + r_{12p} e^{-2j\beta}}{1 + r_{01p} r_{12p} e^{-2j\beta}} \quad (B.20$$

$$r_{012s} = \frac{r_{01s} + r_{12s} e^{-2j\beta}}{1 + r_{01s} r_{12s} e^{-2j\beta}} \quad (B.21$$

and similarly, the ratio of the amplitude of the resultant transmitted wave to the amplitude of the incident wave is given by the total transmission coefficients

$$t_{012p} = \frac{t_{01p} t_{12p} e^{-j\beta}}{1 + r_{01p} r_{12p} e^{-2j\beta}} \quad (B.22$$

$$t_{012s} = \frac{t_{01s} t_{12s} e^{-j\beta}}{1 + r_{01s} r_{12s} e^{-2j\beta}} \quad (B.23$$

The phase β follows from a geometrical consideration of the phase difference, which is given by the path difference of two neighbouring interfering beams:

$$\beta = \frac{2\pi}{\lambda} d \sqrt{N_1^2 - N_0^2 \sin^2 i_0} \quad (B.24$$

where d is the film thickness.

In the general case, these coefficients are complex numbers. As intensities are proportional to the square of the complex field amplitudes, the corresponding

intensity reflection coefficients, namely, the reflectance and the transmittance of the system are given by:

$$R_{012p} = r_{012p} \cdot r^{*}_{012p} \qquad \text{(B.25}$$

$$R_{012s} = r_{012s} \cdot r^{*}_{012s} \qquad \text{(B.26}$$

$$T_{012p} = \frac{N_2 \cos i_2}{N_0 \cos i_0} t_{012p} \cdot t^{*}_{012p} \qquad \text{(B.27}$$

$$T_{012s} = \frac{N_2 \cos i_2}{N_0 \cos i_0} t_{012s} \cdot t^{*}_{012s} \qquad \text{(B.28}$$

Because the incident infrared light is unpolarised (containing an equal mix of *s*- and *p*-polarisations), the reflectance of the system is g:iven by:

$$R_{012} = \frac{R_{012s} + R_{012p}}{2} \qquad \text{(B.29}$$

and the transmittance of the system by:

$$T_{012} = \frac{T_{012s} + T_{012p}}{2} \qquad \text{(B.30}$$

An example of simulation results is presented in Figure B-2, for a copolymer film thickness of 1.6 µm.

To correct the Fourier Transform Infrared Spectra obtained in reflection mode, the simulated reflectance R_{012} was subtracted from the experimentally obtained reflectance.

Polymer film on aluminium frame - Fourier Transform Infrared Spectroscopy in Transmission mode

This case can be derived from the previous one, by considering that the medium after the polymer film is not silicon wafer anymore, but air. Thus, all the equations presented above can be used, by replacing N_2 with the refractive index of air, N_0.

At the end, the expression of the simulated transmittance, T_{012}, was used instead of R_{012} in order to correct the spectra.

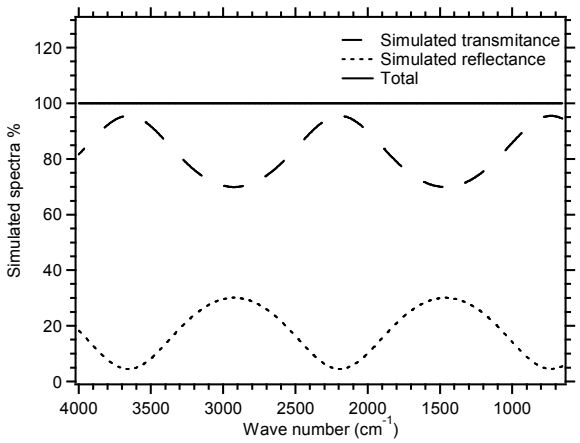

Figure B-2. Results of the spectra simulation, for the case where the polymer film thickness is 1.6 μm

---

1. W. Jacob, A. Keudell, T. Schwartz-Selinger, Infrared analysis of thin films: amorphous, hydrogenated carbon on silicon, Brazilian Journal of Physics 30 (2000) 508.

2. C.Z. Tan, Determination of refractive index of silica glass for infrared wavelengths by IR spectroscopy, Journal of Non-Crystalline Solids 223 (1998) 158.

3. A.M.A. Pistorius, W.J. DeGrip, Deconvolution as a tool to remove fringes from an FT-IR spectrum, Vib. Spect. 36 (2004) 89.

4. T. Yuan, Y. Huang, S. Dong, T. Wang, M. Xie, Infrared reflection of conducting polyaniline polymer coating, Polymer testing 21 (2002) 641.

5. H.G. Tompkins, A user's guide to ellipsometry, Acad. Press, London, 1993.

6. J.H.W.G. den Boer, G.M.W. Kroesen, F.J. de Hoog, Measurement of the complex refractive index of liquids in the infrared using spectroscopic attenuated total reflection ellipsometry: correction for depolarisation by scattering, Appl. Optics, 34 (1995) 5708.

7. J.J. Monzon, L.L. Sanchez-Soto, Fresnel coefficients as hyperbolic rotations, Eur. J. Phys. 23 (2002) 1.

8. K. Yamamoto, H. Ishida, Complex refractive index determination for uniaxial anisotropy with the use of Kramers-Kronig analysis, Appl. Spect. 51 (1997) 1287.